Active Materials in Photonic Crystals

by

Peter Bermel

B.S., University of North Carolina (2000)
M.Phil., University of Cambridge, United Kingdom (2002)

Submitted to the Department of Physics
in partial fulfillment of the requirements for the degree of

Doctor of Philosophy in Physics

at the

MASSACHUSETTS INSTITUTE OF TECHNOLOGY

June 2007

Author ....
Department of Physics
May 24, 2007

Certified by..
John D. Joannopoulos
Francis Wright Davis Professor of Physics
Thesis Supervisor

Accepted by..
Thomas J. Greytak
Associate Department Head for Education

Active Materials in Photonic Crystals

by

Peter Bermel

Submitted to the Department of Physics
on May 30, 2007, in partial fulfillment of the
requirements for the degree of
Doctor of Philosophy in Physics

Abstract

I analyze new phenomena arising from embedding active materials inside of photonic crystal structures. These structures strongly modify the photonic local density of states (LDOS), leading to quantitative and qualitative changes in the behavior of active materials. First, I show that the emission spectrum of pointlike sources inside an "omniguide" is strongly modified by features resembling one-dimensional van Hove singularities in the LDOS. The resulting overall enhancement of the LDOS causes radiating dipoles to emit more rapidly than in vacuum (known as the Purcell effect). Second, I study optically pumped lasing in three model systems: a Fabry-Perot cavity, a line of defects in a two-dimensional square lattice of rods, and a cylindrical photonic crystal. It is shown that high conversion efficiency can be achieved for large regions of active material in the cavity, as well as for a single fluorescent atom in a hollow-core cylindrical photonic crystal, suggesting designs for ultra-low-threshold lasers and ultra-sensitive biological sensors. Third, I consider a photonic crystal-based light-trapping scheme, capable of compensating for weak optical absorption of crystalline silicon solar cells in the near infrared. For a 2 μm-thick cell, relative efficiency enhancements as high as 35% are expected. Fourth, I explore a way to achieve full ±90° electronically-controlled beam steering using a linear array of one-dimensionally periodic elements containing electro-optic materials. Fifth, I consider switching of a single signal photon by a single gating photon of a different frequency, via a cross-phase modulation generated by electromagnetically-induced transparency atoms embedded in photonic crystals. The exact solution shows that the strong coupling regime is required for lossless two-photon quantum entanglement. Finally, I demonstrate that the Purcell effect can be used to tailor the effective Kerr nonlinear optical susceptibility. Using this effect for frequencies close to an atomic resonance can substantially influence the resultant Kerr nonlinearity for light of all (even highly detuned) frequencies. For example, in realistic physical systems, enhancement of the Kerr coefficient by one to two orders of magnitude could be achieved.

Thesis Supervisor: John D. Joannopoulos
Title: Francis Wright Davis Professor of Physics

Acknowledgments

I'd like to acknowledge my supervisor, John D. Joannopoulos. He inspired me to work on research in the field of photonics, and more generally, to focus on that which excites me. He also taught me to strive for excellence in all my professional endeavors, which has already served me well in dealing with the world beyond MIT.

Thanks to Marin Soljacic and Steven G. Johnson for all the time and effort you put into helping me to go from exciting but vague ideas into concrete results and papers. I couldn't have done it without you guys.

It was a pleasure working with all the past and current members of the *ab initio* physics group. I'd especially like to thank Mihai Ibanescu and David Roundy for the time they put into tutoring me in the ways of photonic crystals in the beginning of my grad school career. Thanks to Matt Evans for being a good officemate. Also, it was great having Lefteris Lidorikis, both for our photonics discussions and for his help writing code. I appreciated the help from Michelle Povinelli on several topics such as transfer matrices. Casey (K.C.) Huang was a great friend and contributor, particularly with computer-related issues. Also, thanks to Chiyan Luo for answering my questions and starting work on a number of topics, such as solar cells, that came into play in my thesis. Having David Chan as an officemate was a singular delight, and he did sometimes provide useful code, such as smooth.cpp. I'd also like to thank Alejandro Rodriguez for inspiring me with his dedication to research (not to mention the great work he did to help me). I appreciated Ardavan Farjadpour's help with Meep and in managing the computer issues of our research group.

Thanks to all of my friends and colleagues from outside my research group, for providing me with an opportunity to expand my horizons.

Finally, I want to thank my family: my mother Christine, my father Frank, and my sisters Laura and Chelsea. They always put my education first, and supported me in all my endeavors. I'd like to especially thank my mom for taking personal responsibility for my education, particularly in elementary school, but also at times in middle school and high school. I would be nowhere without her.

Biographical Note

Education and Experience

MASSACHUSETTS INSTITUTE OF TECHNOLOGY, Cambridge, MA, 2001-2007

Ph.D., Dept. of Physics (advisor: John D. Joannopoulos), GPA 5.0/5.0.

- Applied numerical and theoretical techniques to study diverse phenomena in photonic crystals.
- Wrote custom code to calculate properties of low threshold lasers and solar cells.
- Consultant for British Aerospace Engineering AIT: DARPA Visibuilding Project.
- Winner, New England Energy Innovation Collaborative contest for “StarSolar”.
- NSF Graduate Research Fellow (all expenses paid for three years).
- Tutored undergraduate and graduate students in classes and research; graded statistical mechanics.

CAMBRIDGE UNIVERSITY, Cambridge, England, 2000-2001

Masters of Philosophy, Dept. of Physics (advisor: Mark Warner).

- Thesis title: "Photonic bandstructure of cholesteric elastomers”.
- Analyzed photonic bandstructure for a novel material; wrote a program to calculate it numerically.
- Winston Churchill Foundation Scholarship (all expenses paid for one year).

UNIVERSITY OF NORTH CAROLINA, Chapel Hill, NC, 1996-2000

Bachelor of Science with Highest Honors, Physics and Biology (advisor: Michael Rubinstein), GPA: 3.97 / 4.00. Senior Thesis: “Monte-Carlo simulation of adsorption of a polyampholyte chain on a charged surface”. Graduated summa cum laude.

Publications and Invited Talks

- Y. Yi, S. Akiyama, P. Bermel, X. Duan, and L. C. Kimerling, "Sharp bending of on-chip silicon bragg cladding waveguide with light guiding in low-index core materials", IEEE Journal of Selected Topics in Quantum Electronics **12** (6), 1345 (2006).
- L. Zeng, P. Bermel, Y. Yi, N.-N. Feng, B. A. Alamariu, C.-Y. Hong, X. Duan, J.D. Joannopoulos, and L. C. Kimerling, "Optimization of Textured Photonic Crystal Backside Reflector for Si Thin Film Solar Cells", Materials Research Society Symposium Proceedings, vol. **974E**, CC2.6 (2006).
- P. Bermel, A. Rodriguez, S. G. Johnson, J. D. Joannopoulos and M. Soljacic "Single-photon all-optical switching using waveguide-cavity quantum electrodynamics", Physical Review A **74**, 043818 (2006).
- A. Farjadpour, D. Roundy, A. Rodriguez, M. Ibanescu, P. Bermel, J. D. Joannopoulos, S. G. Johnson, and G. W. Burr, "Improving accuracy by subpixel smoothing in the finite-difference time domain", Opt. Lett. **31** (20), 2972 (2006).
- P. Bermel, "Improving Solar Cell Efficiencies through Periodicity", MIT CIPS 3rd Annual Conference (Invited Speaker), May 5, 2006.
- P. Bermel, E. Lidorikis, Y. Fink, and J. D. Joannopoulos, "Simulations of active materials in an electromagnetic field", Phys. Rev. B **73**, 165125 (2006).
- Y. Yi, S. Akiyama, P. Bermel, X. Duan, and L. C. Kimerling, "On-chip Si-based waveguide with 1D photonic crystal cladding", Opt. Express **12**, 4775 (2004).
- P. Bermel, J. D. Joannopoulos, Y. Fink, P. A. Lane, C. Tapalian, "Properties of radiating pointlike sources in cylindrical omnidirectionally reflecting waveguides", Phys. Rev. B **69**, 035316 (2004).
- Y. Yi, P. Bermel, K. Wada, X. Duan, J. D. Joannopoulos, and L. C. Kimerling, "Tunable multichannel optical filter based on silicon photonic band gap materials actuation", Appl. Phys. Lett. **81**, 4112 (2002).

- P. Bermel and M. Warner. "Photonic band structure of cholesteric elastomers", Phys. Rev. E **65**, 056614 (2002).
- Y. Yi, P. Bermel, K. Wada, X. Duan, J. D. Joannopoulos, and L. C. Kimerling, "Low Voltage Tunable One Dimensional Photonic Crystal With Large Air Defects", Proceedings of the Materials Research Society, vol. **722**, L3.3 (2002).
- P. Bermel and M. Warner. "Photonic band structure of highly deformable self-assembling systems", Phys. Rev. E **65**, 010702 (2002).

Patents

- P. Bermel, J. D. Joannopoulos, and C. Luo, "Improving Solar Cell Efficiencies Through Periodicity", filed with USPTO on April 10, 2006.
- P. Bermel and J. D. Joannopoulos, "Pi-Phase Shift Device for Light", filed with USPTO on November 15, 2006.

Computer Skills

- Programming Languages: C/C++, FORTRAN, Perl, MATLAB, MPI, bash/csh, LaTeX, Scheme, BASIC.
- Operating Systems: Linux (Debian, Redhat), AIX, HP-UX, Catamount, Windows XP/Vista, Mac OS X.
- Numerical Techniques: finite-difference time-domain, frequency-domain, eigenmode decomposition, matrix diagonalization, transfer matrix method.

Contents

List of Figures

List of Tables

Chapter 1

Introduction

1.1 Background and motivation

One of the primary drivers of solid state physics in the twentieth century was understanding the unique properties of semiconductors. It is now well-known that the combination of an electronic bandgap, which causes a pure semiconductor to behave as an insulator at room temperature, and doping, which allows one to add a controlled amount of conductivity to a pure sample, leads to a great deal of freedom in materials design, and enables many novel physical devices. The most important one is, of course, the transistor, which led to the modern computer industry.

The physics of semiconductors, or any crystalline material, begins with Schrödinger's equation, which controls the quantum-mechanical behavior of each individual electron, combined with Bloch's theorem, which dictates the form of the electronic wavefunction in the crystal. It can be shown that electrons in these materials will form a Blöch wave, which is a product of two terms, one being a function with the same periodicity as the crystal lattice, and the other being a plane wave. The periodicity of the potential means that these plane waves are only defined up to a so-called "reciprocal lattice vector". One can then construct a region enclosing all the unique wavevectors for a given lattice, which is referred to as a Brillouin zone. Generally, at the Brillouin zone boundaries, two or more bands will intersect (due to symmetry), which can give rise to an avoided crossing in the presence of a potential. In semiconductors, this potential is strong enough to give rise to a complete bandgap, i.e., a range of electron energies that are forbidden to exist within the infinite crystal.

The field of photonics was initiated by researchers who noticed a formal similarity between the Schrödinger equation:

$$-\nabla^2\psi = \frac{2m}{\hbar^2}(E - V)\psi, \tag{1.1}$$

and Maxwell's equations, in a region with no free charges or currents (with a dielectric function $\epsilon(\vec{x}) = \bar{\epsilon} + \delta\epsilon(\vec{x})$):

$$-\nabla^2\vec{E} \approx \left[\bar{\epsilon}(\omega/c)^2 - \left(-\delta\epsilon(\vec{x})(\omega/c)^2\right)\right]\vec{E}, \tag{1.2}$$

provided that $\delta\epsilon(\vec{x})$ is small [6, 7]. This demonstrates that one can view the propagation of an electric field through space in much the same way as a quantum-mechanical wavefunction. Here, $-\delta\epsilon(\vec{x})(\omega/c)^2$ serves as an effective potential for the photons. This result implies that one can transfer much of the existing understanding of electronic bandstructures over to photonic bandstructures. And furthermore, one can imagine making photonic structures in analogy with various existing materials. In particular, by analogy with semiconductors, one might imagine that a periodic structure (as in Fig. 1-1) with sufficient index contrast and the correct lattice structure (e.g., face-centered cubic, or fcc), would give rise to a *photonic* bandgap (PBG) [1].

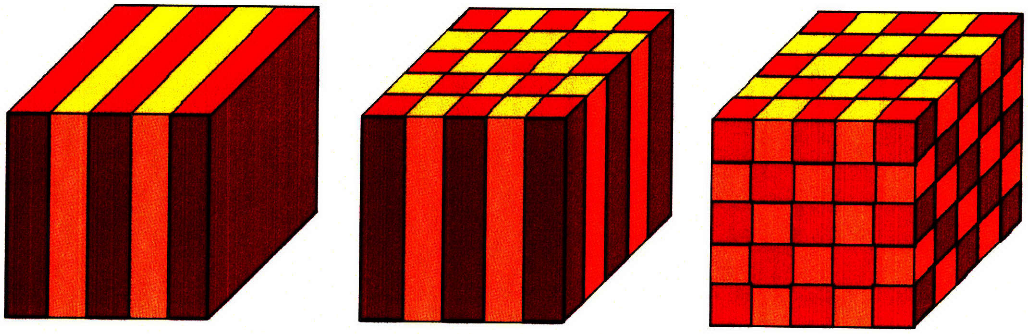

Figure 1-1: Illustration of periodicity in a photonic crystal in one, two, and three dimensions (adapted from Ref. [1]).

However, it turns out that calculating photonic bandstructures creates unique challenges not present in the calculation of electronic bandstructures. One initial proposal for a 3D photonic bandgap structure [8], based on an fcc lattice with high dielectric contrast, turns out *not* to have a true 3D PBG, but instead a pseudogap [9]. The simplest structure displaying a full PBG is instead a diamond structure [9]. The procedure used for calculating the previous result, however, is relatively inefficient for large systems. In 1993, a high performance $\mathcal{O}(N)$ method for calculating photonic bandstructures was introduced in order to reduce memory and calculation time requirement by a factor of 10^4 [10].

In subsequent years, the advent of an efficient method for simulating photonic crystals gave rise to many new results and applications, including: confinement of light with low losses and small modal volume [11]; wavelength-scale bends that transmit light without losses [12]; 2D periodic slabs capable of extracting light from LEDs [13] as well as confining light in all directions [14]; suppression or enhancement of spontaneous emission [15]; channel-drop filters [16]; and omnidirectional reflectors [17].

In particular, omnidirectional reflectors are simply stacks of alternating high and low dielectric materials (cf. the left-hand side of Fig. 1-1), with the property that they reflect incoming light of all angles and polarizations [17]. In the past, that was thought to be impossible because of the Brewster angle: a special angle, predicted by Fresnel's equations, at which all TM-polarized radiation passes from one dielectric medium to another. However, if both the high and low dielectric constants are sufficiently well above the index of the material from which light is incident, then the Brewster angle can be pushed outside of the light cone. This allows omnidirectional reflectivity, as illustrated in Fig. 1-2.

Furthermore, these omnidirectional reflectors can be rolled into cylinders with a hollow core, which are referred to as omniguides. As illustrated in Fig. 1-3, this gives rise to modes that can be guided through air (for omnidirectionally reflected frequencies) in a fashion very similar to a hollow metal waveguide [18, 19, 3]. However, the advantage of the omniguide is that it can offer much lower losses than a metallic waveguide could ever achieve in the visible spectrum, due to Ohmic losses from the finite conductivity of the metal.

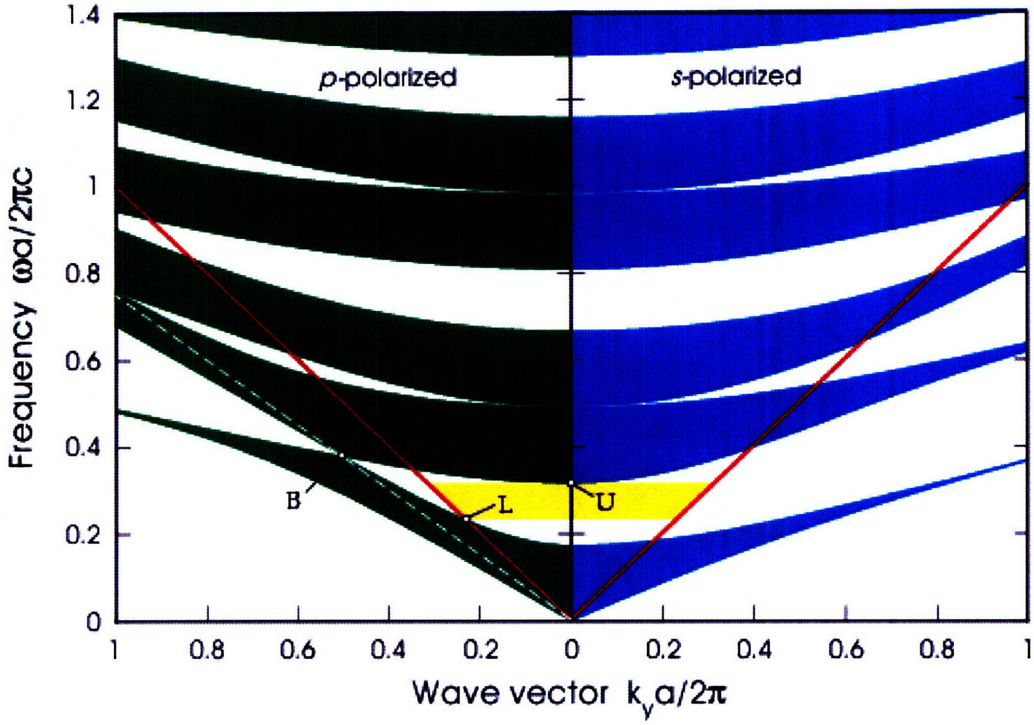

Figure 1-2: Projected bandstructure (frequency vs. transverse wavevector k_y) for an omnidirectional reflector with $\epsilon_{\text{high}} = 13$, and $\epsilon_{\text{low}} = 2$ – omnidirectional reflection is denoted by the yellow region; the Brewster angle B lies outside the light cone (adapted from Ref. [2]).

Today, an open problem is characterizing the phenomena that can emerge when "active materials" are placed in photonic crystals. In this thesis, active materials are taken to be materials that actively emit or absorb light, materials with nonlinear susceptibilities, and materials displaying electromagnetically induced transparency. Since it has already been shown that photonic crystals are capable of strongly modifying the electromagnetic environment, one would expect many new physical phenomena to occur. The degree to which the electromagnetic environment changes in the presence of photonic crystals is quantified by the local density of states (LDOS), which is defined by:

$$g(\omega, \vec{r}) = \sum_{n,\vec{k}} \epsilon(\vec{r}) \left| \vec{E}_{n\vec{k}}(\vec{r}) \right|^2 \delta(\omega - \omega_{n\vec{k}}), \tag{1.3}$$

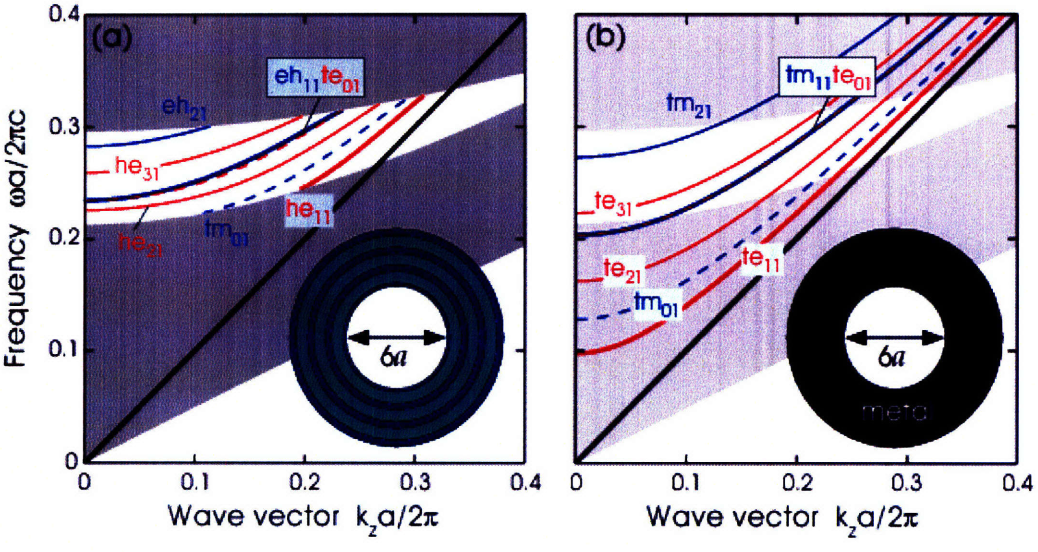

Figure 1-3: Projected bandstructure for (a) an omniguide with a diameter of 6 periods of the omnidirectional reflector, and (b) for a metallic waveguide with the same diameter. Just like in the metallic waveguide, modes in the omniguide observe a quadratic dispersion, for omnidirectionally reflected frequencies (adapted from Ref. [3]).

where $\int dV\, \epsilon(\vec{r}) \left|\vec{E}_{n\vec{k}}(\vec{r})\right|^2 = 1$ for each wavevector $\vec{k}$ and band n, whose dispersion relation is given by $\omega_{n\vec{k}}$. As is evident from its definition, the LDOS is influenced by both the photonic bandstructure, given by $\omega_{n\vec{k}}$, as well as the field profiles $\vec{E}_{n\vec{k}}(\vec{r})$ of each of those bands. In the presence of defect structures, the field profiles for modes with frequencies inside the photonic bandgap are strongly localized inside the defect region, leading to huge increases in the local density of states. This is a powerful effect that has the potential to cause not just a quantitative change in the strength of existing material properties, but also qualitative changes, i.e., fundamentally new phenomena. One example of the latter is the Purcell effect; other examples are explored later in this thesis. Some of these phenomena can only be properly understood through the lens of quantum mechanics. Below, I present a brief summary of the cavity quantum electrodynamics formalism that will be used in subsequent chapters, along with a discussion of some of the intriguing phenomena already known in the literature, such as the Purcell effect and electromagnetically-induced transparency.

1.2 Cavity quantum electrodynamics

1.2.1 Purcell effect

Cavity quantum electrodynamics (CQED) is quantum electrodynamics (QED) in cavities with discrete electromagnetic modes. One example in which this formalism applies is a two-level atom with a transition at the same frequency as the fundamental electromagnetic mode of a cavity. The CQED Hamiltonian for this system can be derived from the expression:

$$H = -\sum_i q_i \vec{x}_i \cdot \vec{E} = -\vec{d} \cdot \vec{E}, \tag{1.4}$$

where $\vec{d}$ is its dipole moment, and $\vec{E}$ is the applied electromagnetic field. The latter equality holds true insofar as the atom behaves like a dipole. This is a very good approximation as long as the wavelength of the light is much longer than the size of the atom, which is true for all wavelengths studied in this thesis, ranging from ultraviolet through microwave wavelengths.

In the next step of the derivation, the electric field can be quantized according to [20]:

$$\vec{E}(\vec{r}) = i \sum_\mu \sqrt{\frac{\hbar\omega_\mu}{\epsilon}} \left[\vec{\alpha}_\mu(\vec{r}) a_\mu - \vec{\alpha}^*_\mu(\vec{r}) a^\dagger_\mu\right], \tag{1.5}$$

where a is the photon annihilation operator, ϵ is the dielectric constant of the medium filling the cavity (the refractive index $n = \sqrt{\epsilon}$), ω_μ is the frequency of mode μ, and $\vec{\alpha}_\mu$ is the mode function, normalized such that $V_{\text{mode}} = 1/|\vec{\alpha}_\mu|^2_{\text{max}}$. One can then apply time-dependent perturbation theory (Fermi's golden rule) to obtain the spontaneous emission decay rate [20]:

$$\gamma_{\text{SE}} = \frac{8\pi Q_\mu}{\hbar} \frac{|\vec{d} \cdot \vec{\alpha}_\mu(\vec{r})|^2}{\epsilon} \frac{(\gamma_\mu/2)^2}{(\omega - \omega_\mu)^2 + (\gamma_\mu/2)^2}, \tag{1.6}$$

where Q_μ is the quality factor of mode μ of the cavity, while γ_μ is its radiative width. If one then divides by the decay rate in free space at the central frequency, given by

$\gamma_o = 4nd^2\omega_\mu^3/(3\hbar c^3)$, one can obtain a spontaneous emission enhancement factor F_P given by [20, 21]:

$$F_P = \frac{3Q_\mu}{4\pi^2 V_{\text{mode},\mu}}\left(\frac{\lambda}{n}\right)^3, \tag{1.7}$$

where $V_{\text{mode},\mu}$ is the effective modal volume of mode μ. This is also known as the Purcell enhancement factor – named after the Purcell effect [22]. It predicts that high quality factor cavities and small modal volumes can strongly enhance spontaneous emission. Physically, high quality factor cavities contribute to spontaneous emission because they cause the cavity to resonate more strongly at the resonant frequency than it would in free space. Small modal volumes also enhance spontaneous emission because the field is strongly localized on top of the dipole moment of the atom.

1.2.2 Jaynes-Cummings Hamiltonian

The dipole operator can also be quantized according to:

$$\vec{d} \rightarrow i\vec{d}(\sigma^+ + \sigma^-), \tag{1.8}$$

where $\sigma^\pm$ are the creation and annihilation operators for the excitation. One can then rewrite equation (1.4) with the help of equations (1.5) and (1.8) to obtain the expression:

$$H = \sum_\mu d\sqrt{\frac{\hbar\omega_\mu}{\epsilon}}\left[\vec{\alpha}_\mu(\vec{r})a_\mu(\sigma^+ + \sigma^-) - \vec{\alpha}^*_\mu(\vec{r})a^\dagger_\mu(\sigma^+ + \sigma^-)\right] \tag{1.9}$$

Applying the rotating-wave approximation, in which terms that oscillate rapidly and have a vanishing average value are neglected, this expression can be simplified to:

$$H = \sum_\mu \hbar g_\mu(a^\dagger_\mu\sigma^- + a_\mu\sigma^+), \tag{1.10}$$

known as the Jaynes-Cummings Hamiltonian, where $a^\dagger$ (a) is the raising (lowering) operator for the cavity photon mode, σ^+ (σ^-) is the raising (lowering) operator for the electronic excitation, and g_μ is the coupling strength for mode μ, given by:

$$g_\mu = d\sqrt{\frac{\omega_\mu}{\hbar\epsilon V_{\text{mode},\mu}}}. \tag{1.11}$$

If one introduces loss into this system via the Hamiltonian $H_{\text{loss}} = i\hbar\Gamma a^\dagger a + i\hbar\kappa\sigma_z$, one obtains two physical regimes: weak coupling and strong coupling. Physically, weak coupling just means that the eigenmodes of the system are similar to the normal atomic and photonic states, with a coupling that can be treated as a perturbation. This is the regime in which the Purcell effect is significant, since spontaneous emission can be thought of as a time-dependent perturbation of the excited atom eigenstate. Strong coupling, on the other hand, corresponds to eigenmodes which consist of superpositions of atomic and photonic modes. Mathematically, it occurs when $g > |\Gamma - \kappa|/2$. In this case, Rabi splitting will occur, in which one mode is split from the other by a finite energy gap, given by twice the coupling strength. This effect is analogous to band anti-crossing in the physics of bandstructures, and just as in that case, can be derived from degenerate perturbation theory.

1.2.3 Electromagnetically-induced transparency

Electromagnetically-induced transparency (EIT) is a phenomenon whereby the optical properties of a medium experienced by a probe beam can be dramatically modified by the introduction of a so-called "coupling" beam [4, 23]. EIT occurs in three-level atomic systems, such as the one illustrated in Fig. 1-4. Here, there are two metastable internal states, labeled $|1\rangle$ and $|2\rangle$, coupled to a common upper state $|3\rangle$, which has a radiative decay rate Γ. In the absence of the coupling beam, the probe beam observes an absorption peak when tuned to the transition frequency ω_{13}. On the other hand, the presence of a coupling beam with frequency ω_{12} can actually reduce the on-resonance cross-section for the absorbing beam by many orders of magnitude [24]. The way in which this occurs is coherent population trapping into the so-called "dark state", a superposition of $|1\rangle$ and $|2\rangle$ that are decoupled from the upper level [25]. This can be seen mathematically as follows [4]: if one then writes the EIT interaction

Hamiltonian as:

$$H_I = (\Delta_p + i\Gamma)\sigma_{33} + (\Delta_p - \Delta_c)\sigma_{22} + g_p a_p^\dagger \sigma_{13} + g_c a_c^\dagger \sigma_{23} + \text{c.c.} \tag{1.12}$$

then this Hamiltonian can be written in the one-excitation manifold as:

$$H_I = c^\dagger \begin{pmatrix} 0 & 0 & g_p \\ 0 & \Delta_p - \Delta_c & g_c \\ g_p & g_c & \Delta_p + i\Gamma \end{pmatrix} c \tag{1.13}$$

where $c^\dagger = \begin{pmatrix} a_p^\dagger & a_c^\dagger \sigma_{21} & \sigma_{31} \end{pmatrix}$. Now consider the case where a two-photon resonance exists, i.e., $\Delta_c = \Delta_p$. This gives rise to an eigenstate $d^\dagger = \begin{pmatrix} g_c & -g_p & 0 \end{pmatrix}$. Remarkably, this so-called "dark state" has zero amplitude in the highest atomic excitation, which leads to the observed dramatic decrease in absorption of the probe beam in a steady state. Nonetheless, this state has extremely high dispersion, which leads to the unique combination of ultra-slow light propagation and low losses. This also gives rise to remarkably high Kerr nonlinear coefficients, which are many orders of magnitude larger than in ordinary materials. One of the many applications enabled by this remarkable confluence of properties is presented in chapter 6.

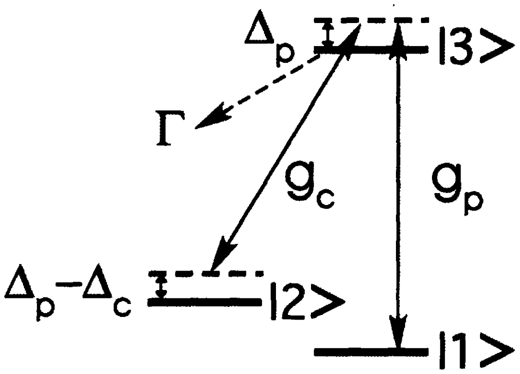

Figure 1-4: Level diagram for a 3-level EIT atom, with an upper level $|3\rangle$ which has a spontaneous decay rate Γ and detuning Δ_p, and two lower levels $|1\rangle$ and $|2\rangle$ with coupling strengths g_p and g_c to the upper level. Level $|2\rangle$ also has a detuning $\Delta_p - \Delta_c$ that vanishes upon two-photon resonance (adapted from Ref. [4]).

1.3 Overview of this work

Active materials can display a rich variety of physical phenomena, including spontaneous emission, stimulated emission, and the photovoltaic effect. These phenomena are the basis of a wide variety of technologically important devices, e.g., optical sensors, lasers, and photovoltaic cells. Over the next several chapters, the effects of placing these active materials in photonic crystals are explored for a variety of applications.

Consider the problem of guiding light from a source to a receiver. Typically this is solved using a waveguide. Specific devices of this type include optical amplifiers, which utilize index-guiding, and hollow waveguide optical sensors, which confine light with a metal or high-index material. However, both of these waveguiding approaches exhibit low output efficiency, and additionally, may be limited by the core material properties. With the index-guiding mechanism, isotropic emission from a randomly oriented collection of dipoles leads to high radiation losses. In the case of metal, high ohmic losses occur at IR and visible wavelengths. Alternatively, one could envision trapping light using an omnidirectionally reflective mirror wrapped into a cylindrical waveguide, which would combine low losses with collection at all angles. In chapter 2, the behavior of pointlike electric dipole sources enclosed by such a waveguide is analyzed. It is found that the emission spectrum of a source inside the waveguide is strongly modified by features resembling 1D van Hove singularities in the local density of states. The resulting overall enhancement of the LDOS at certain frequencies causes radiating dipoles to emit more rapidly than seen in vacuum (known as the Purcell effect). The effect of varying the positions and orientations of electric dipole sources is also studied.

Another open area of investigation lies in optimizing the design of optically-pumped lasing systems. While analytical solutions can be found for very simple designs, such solutions do not necessarily apply to photonic-crystal based lasers. Obtaining precise values for lasing thresholds and conversion efficiencies requires a numerical approach. In chapter 3, a detailed numerical scheme is presented in order to model the interaction of light with active dielectric media embedded in photonic crystals. Optically pumped lasing is studied in three model systems: a Fabry-Perot cavity, a line of defects in a 2D square lattice of rods, and a cylindrical photonic crystal. Field profiles and conversion efficiencies are calculated for these systems. It is shown that high conversion efficiency can be achieved for large regions of active material in the cavity, as well as for a single fluorescent atom in a hollow-core cylindrical photonic crystal, suggesting designs for ultra-low-threshold lasers and ultra-sensitive fluorescent sensors.

A different, but important, problem is how one can maximize the performance of crystalline silicon (c-Si) based solar cells, which often suffer from imperfect light trapping and low efficiencies. Most photovoltaic cells available today are made from either c-Si or related materials, such as nanocrystalline silicon (nc-Si). However, these crystals have an indirect bandgap, which gives rise to weak absorption of light in the near infrared, a range of wavelengths which contains over a third of usable solar photons. Thus, a c-Si solar cell with a plain wafer geometry substantially less than 1 mm thick (e.g., 100 μm) will fail to absorb a significant number of photons that could otherwise be used to generate power in the cell, giving rise to low efficiencies. At the same time, the expense of c-Si for a 300 μm-thick wafer with a correspondingly long diffusion length drives up costs significantly. As a result, efficient light trapping schemes that can achieve high levels of absorption for thin films of silicon are needed. In chapter 4, a photonic crystal-based light-trapping scheme capable of compensating for this problem is proposed and analyzed. The simulations predict that for a 2 μm-thick slab of c-Si or nc-Si, overall power generation can be enhanced by 24.3% for a distributed Bragg reflector with a 1D grating, and 25.3% for a 2D triangular photonic crystal, made of air holes in silicon.

Another important class of active materials are nonlinear materials, such as Pockels or Kerr media. Optical nonlinearities have fascinated physicists for many decades because of the variety of intriguing phenomena that they display, such as frequency mixing, supercontinuum generation, and optical solitons. Moreover, they enable numerous important applications such as higher-harmonic generation, electro-optic phased arrays, integrated all-optical signal processing, and all-optical quantum information processing. Designing such devices to operate effectively with low powers is a fundamental challenge, because a unique combination of large nonlinearities and low losses is required. In the next three chapters, several different approaches to enhancing nonlinearities are discussed, along with some resulting applications.

Many common electro-optic nonlinear materials can be used for high speed signal modulation. However, the strength of nonlinearity exhibited is too low for many applications. One example is an optical phased array, in which the phase and amplitude of light across a wavefront must be dynamically controlled over a large range. In chapter 5, 1D photonic crystal devices are developed to enhance the small index shift associated with the electro-optic effect. It is shown that if one surrounds the electro-optic material with a cavity of quality factor Q, the maximum phase sensitivity is increased by Q compared to a bare slab of material. Such devices can be placed into linear arrays in order to enable applications such as anamorphic lensing, array generation, aberration correction, and beam steering. In particular, the presence of photonic crystals enable high-speed full $\pm 90^\circ$ beam steering with a single stage (rather than multiple stages which gradually increase the angle of the light at each step).

One special class of materials discussed earlier, known as EIT materials, exhibit nonlinear coefficients up to 12 orders of magnitude larger than those observed in common materials. As a result, one can envision inducing strong interactions between two very weak signals of different frequencies by placing a 4-level EIT atom in a high-Q cavity, so that a very small signal at a specific atomic transition frequency could shift another resonant frequency of the system by a measurable amount. This effect has already been demonstrated to work semi-classically for fields with magnitudes as small as those expected for a single photon. In chapter 6, this approach is studied for a design consisting of a PhC waveguide and a PhC microcavity containing a four-level EIT atom using an analytical model based on waveguide-cavity QED. It is solved exactly and analyzed using experimentally accessible parameters. It is demonstrated to be capable of switching of a single signal photon by a single gating photon of a different frequency, via a cross-phase modulation. It is found that the strong coupling regime is required for lossless two photon quantum entanglement.

Finally, in chapter 7, I demonstrate that the effective nonlinear optical susceptibility can be tailored in a novel way: through the Purcell effect. While this is a general physical principle that applies to a wide variety of nonlinearities, I specifically investigate the Kerr nonlinearity, since it is present in most materials. For definiteness, I use a generic two-level model for Kerr nonlinearities. I show theoretically that using the Purcell effect for frequencies close to an atomic resonance can substantially influence the resultant Kerr nonlinearity for light of all (even highly detuned) frequencies. For example, in realistic physical systems, enhancement of the Kerr coefficient by one to two orders of magnitude could be achieved.

Chapter 2

Properties of radiating pointlike sources in cylindrical omnidirectionally-reflecting waveguides

2.1 Introduction

A variety of technologically significant devices rely on guiding light from a source placed inside a waveguide. These include optical amplifiers, which utilize index-guiding, and hollow waveguide optical sensors, which confine light with metal or high-index material. While the guiding mechanisms in these two devices are different, both exhibit low output efficiency and may be limited by the core material properties. With the index-guiding mechanism, isotropic emission from a randomly oriented collection of dipoles leads to high radiation losses. In the case of metal, high ohmic losses occur at IR and visible wavelengths [26, 27, 28].

Rather than using lossy metallic structures, one could also envision using a highly reflective dielectric mirror to confine light. In this paper I study the performance of a structure consisting of a uniform index core, possibly air, surrounded by a dielectric mirror cladding, known as an omniguide. I find that this structure not only minimizes the losses due to radiation and absorption, but due to the Purcell effect, also achieves an output power that exceeds that of the source in vacuum at some frequencies.

It has been known for some time that a finite slab of stratified dielectric media will reflect certain frequencies of light better than others. One could easily predict multiple slabs of dielectric could enhance this effect for a target frequency. However, solving any but the simplest of cases is a formidable problem using the method of multiple reflections [29]. Nonetheless, the development of the transfer matrix method by multiple authors in the 1940's and 1950's led to the theoretical prediction of highly efficient dielectric mirrors [30, 31, 32]. This approach was then extended to the cylindrical case by Yeh and Yariv in 1978 [33]. Although the theory developed by Yeh and Yariv is of general applicability, emphasis was placed on obtaining Bragg reflections for a specific frequency and conserved wavevector, which could be obtained using a relatively small dielectric contrast. In early papers, for example, Cho, Yariv, and Yeh conducted experiments on Bragg waveguides with a reflecting layer of indices $n_1 = 3.43$ and $n_2 = 3.35$ [34]; Yeh considered a slightly higher contrast of $n_1 = 2.89$ and $n_2 = 3.38$ in a theoretical paper [35]. However, other studies indicated that 10 layers of a low dielectric-contrast cladding (with $n_1 = 1.485$ and $n_2 = 1.45$) for a hollow-core structure, even with a radius of tens of wavelengths, can result in losses in excess of 1 dB per mm [36]. The benefits of using a high-contrast periodic dielectric fiber ($n_1 = 4.0$ and $n_2 = 2.4$) with metal on the outside was also studied theoretically [37], but to the best of my knowledge, not implemented experimentally. As a result, most studies of these Bragg fibers continued to focus on low-contrast dielectric claddings through the mid-90s, despite their limitations [38]. Interest in these structures was renewed, however, upon the theoretical discovery and experimental fabrication of omnidirectional mirrors – one-dimensionally periodic dielectric structures that reflect light from all incident angles and polarizations [17]. The concept of omnidirectional reflectivity can readily be extended to a system with cylindrical symmetry [18, 19, 39]. Recently, these structures have been fabricated in fiber form and used to demonstrate low-loss transmission of high-intensity IR light [40, 41].

The behavior of pointlike light sources in an omniguide is an interesting problem for two reasons: spontaneous emission may be modified, and coupling to index-guided modes may occur. Spontaneous emission will take place in the photon modes available to the emitter. All the electromagnetic modes of free space are not necessarily available in the presence of materials. For example, it has been shown theoretically and experimentally that a pointlike light source between two conducting plates will experience strongly suppressed emission below the cutoff frequency [42, 43]. Also, it has been shown experimentally [44] that a metallodielectric photonic crystal suppresses spontaneous emission at frequencies within the bandgap, giving rise to emission concentrated within a relatively narrow frequency range. In this work, the hollow cylindrical core mimics a line defect in a 3D photonic crystal structure. I operate at frequencies within the gap, where most photon modes are suppressed except for those associated with the hollow-core defect. Spontaneous emission into these hollow-core modes would be predicted to be strongly enhanced. The second issue regards coupling to index-guided modes. A monochromatic pointlike light source in a hollow waveguide can couple to modes at a given frequency with any axial wavevector, i.e., values both above and below the light line. The modes below the light line are evanescent and would not cause losses in equilibrium if the waveguide were made of a perfect conductor; however, in a hollow waveguide with dielectric cladding, fields that are evanescent inside the hollow core can couple to propagating modes in the dielectric cladding. These index guided modes can be lossy if the high-index material is absorptive, if the material outside the dielectric cladding has an index higher than the hollow core, or if there are any bends or kinks in the dielectric cladding.

The behaviors of pointlike light sources in artificial opals and 2D triangular lattices of rods have been predicted through the calculation of the local density of states at several points within the systems [45]. Also, the Green's function of a point source in an optical waveguide has been calculated in two dimensions [46]. However, the behavior of light sources in 1D periodic hollow omniguide structures has yet to be explored in great detail.

Some recent experimental work on a ring of pointlike sources inside an omniguide

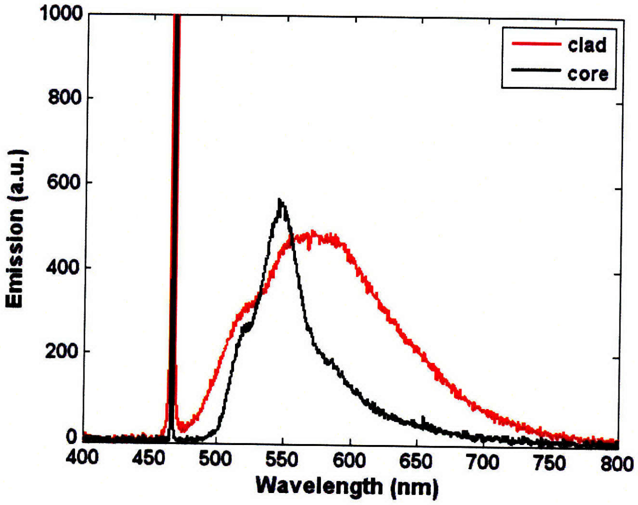

Figure 2-1: Experimental measurement of the flux spectrum for spontaneously emitted light collected in the core and cladding regions of an omniguide fiber (adapted from Ref. [5]).

has shown that hollow omniguides can guide spontaneously emitted light [5]. Fig. 2-1 shows the flux spectrum observed for spontaneously emitted light collected in the core and cladding regions of the end of the waveguide. The core and cladding transmissions are of similar magnitude. However, note that the transmission is more sharply peaked, most likely corresponding to a particular set of guided modes within the omnidirectional bandgap region. The cladding guides light based on index-guiding, and thus is less sensitive to wavelength. This data confirms the importance of cladding modes, and raises the possibility that emission is modified in the presence of omniguide fiber.

This chapter predicts the behavior of light sources in hollow omniguide structures through the following approach. First, a realistic model of an omniguide fiber, suitable for simulation, is developed. Initial results for a single dipole at the center of the omniguide, which indicate a substantial modification of the rate of spontaneous emission in vacuum, are then presented. They are explained in terms of the local density of states of the 1D omniguide system. Additional results for dipoles with different radial positions and orientations are then given. Finally, the problem of a dipole at the inner surface coupling to index-guided modes in the cladding is discussed.

2.2 Simulation

The computational set-up is illustrated to scale in Fig. 2-3. Following Ref. [18], the high-index tellurium (Te) layers ($n = 4.6$) have a thickness one-half that of the low-index polystyrene (PS) layers ($n = 1.6$); the thickness of one Te/PS bilayer is defined as a. The inner radius of the hollow core, r_i, defined as the distance from the center of the cylinder to the first layer of dielectric material, is chosen to be $2.144a$. For a realistic set of materials such as titania and silica, one might require 20 bilayers; for computational ease, three layers of tellurium and polystyrene, materials used for experiments in infrared in Ref. [17], are substituted. Therefore, the outer radius, r_o, defined as the distance from the center of the cylinder to the outer air region, is $5.144a$.

A single dipole source is placed at one end of the waveguide within the hollow core region. In the limit of an infinite number of layers of an omnidirectionally reflecting mirror, all of the emitted light should presumably couple into lossless propagating modes. The actual number of layers required for relatively high reflection is illustrated in Fig. 2-2.

For this system, Maxwell's equations are solved in a finite difference time-domain simulation, based on the work of Yee [47], using perfectly-matched layer absorbing boundary conditions [48]. A constant-frequency AC current modulated by a Gaussian envelope serves as the electric dipole source. The key quantity of interest is the total flux emerging from the far end of the waveguide, which is measured in the simulation as the integrated Poynting flux through a square plane covering the hollow core region.

2.3 Results and discussion

While there are many possibilities for the placement and orientation of even a simple dipole current source, I start off with it placed at one end of the waveguide in the center of the hollow region. There are still many choices for the orientation of the dipole; I choose a dipole pointing along the axial direction, z, since in vacuum, it

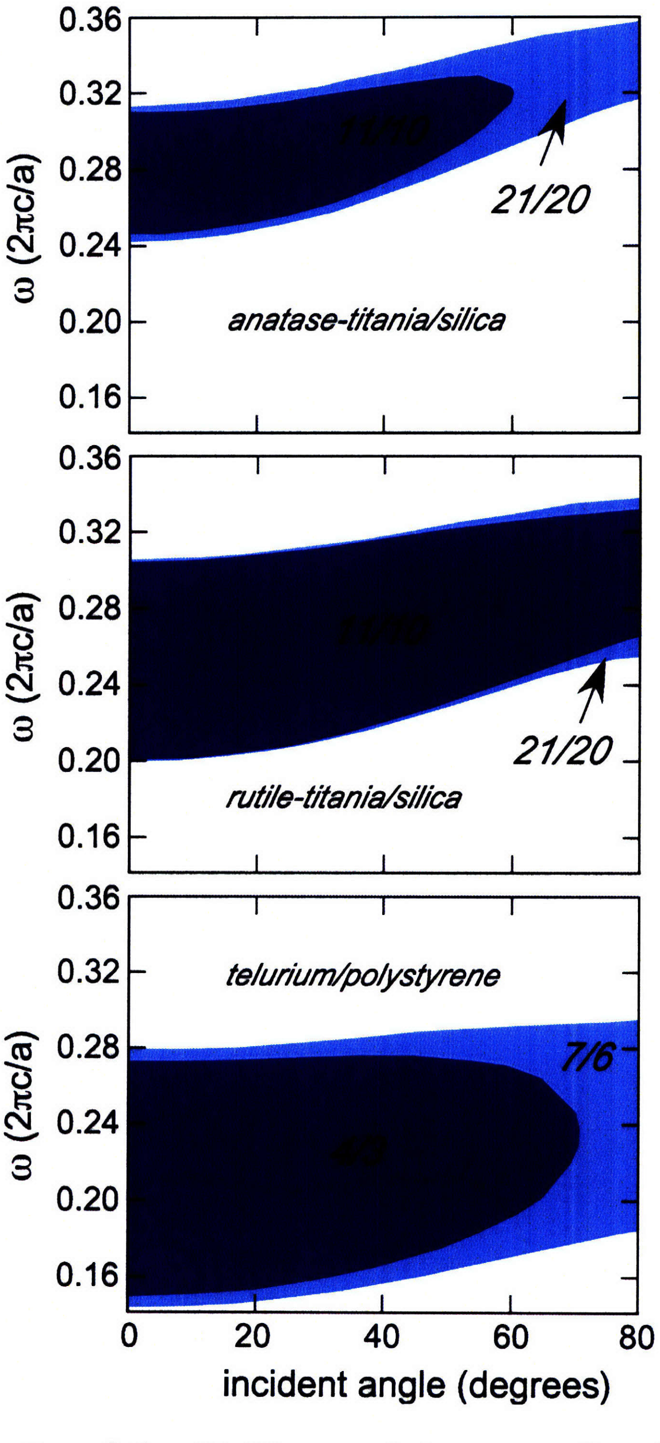

Figure 2-2: Illustration of the -20 dB transmission ranges (i.e., for which at least 99% of light is reflected) for three different material pairs at two different numbers of layers (listed as the number of high-index and low-index layers, respectively).

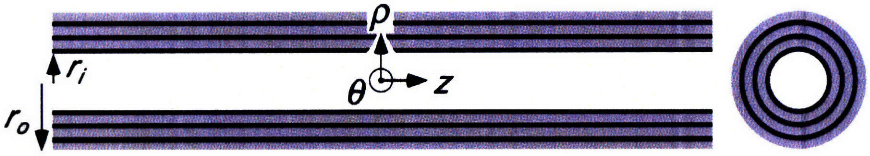

Figure 2-3: Waveguide used in simulations, consisting of 3 bilayers of tellurium ($n = 4.6$) and polystyrene ($n = 1.6$). The core is hollow and made of air (the inner radius – the distance from the center to the innermost cladding layer – is given by $r_i = 2.144a$; the outer radius – the distance from the center to the outermost cladding layer – is given by $r_o = 5.144a$).

would lose most of its power in the transverse directions, leaving very little at a small flux plane far away in the z direction. The introduction of a cylindrical dielectric mirror changes this result dramatically, however. In Fig. 2-4, the initial dipole pulse encounters the reflective wall and couples into the TM_{01} mode, which propagates down the hollow part of the waveguide and leaves the far end. Figure 2-5 quantifies the effect of the presence of the waveguide, by measuring the frequency spectrum of the flux in arbitrary units (defined as $F(\omega) = \int_{\text{surface}} \mathbf{S}(\omega) \cdot \hat{\mathbf{n}}\, \mathrm{d}A$, where $\mathbf{S}(\omega) = \frac{1}{2}\mathrm{Re}\{\mathbf{E}(\omega) \times \mathbf{H}(\omega)^*\}$, and $\mathbf{E}(\omega) = \int_0^T e^{i\omega t}\mathbf{E}(t)\, \mathrm{d}t$, etc.) and comparing it to the flux observed for a hollow glass waveguide and the total flux emitted by a dipole in vacuum.

Clearly, the performance of a hollow glass tube ($n = 2.6$), which relies upon index guiding, is several orders of magnitude below the ideal of 50% transmission of the total flux emitted in vacuum. The hollow cylindrical waveguide, on the other hand, has enhanced performance vis-à-vis the vacuum case within a narrow range of frequencies above cutoff. This behavior is a result of the *Purcell effect.* Purcell found that boundary conditions on the electromagnetic field around a dipole emitter can substantially alter the emission rate [22]. In the case of a resonant cavity with a single resonant mode of quality factor Q, it has been shown [42] that the spontaneous rate of emission at the resonant frequency will be enhanced by a factor of Q. One can also make the more detailed calculation by first noting that the frequency near cutoff is given by $\omega^2 = \omega_c^2 + c^2k_z^2/n^2$, where ω_c is the cutoff frequency, and k_z is the component of the wavevector pointing along the long axis, which yields the following expression for the density of states within the cavity [42]: $g_C(\omega) = \frac{2}{V}\frac{dn}{d\omega} = \frac{4}{cA_g}\frac{\omega}{\sqrt{\omega^2-\omega_c^2}}$.

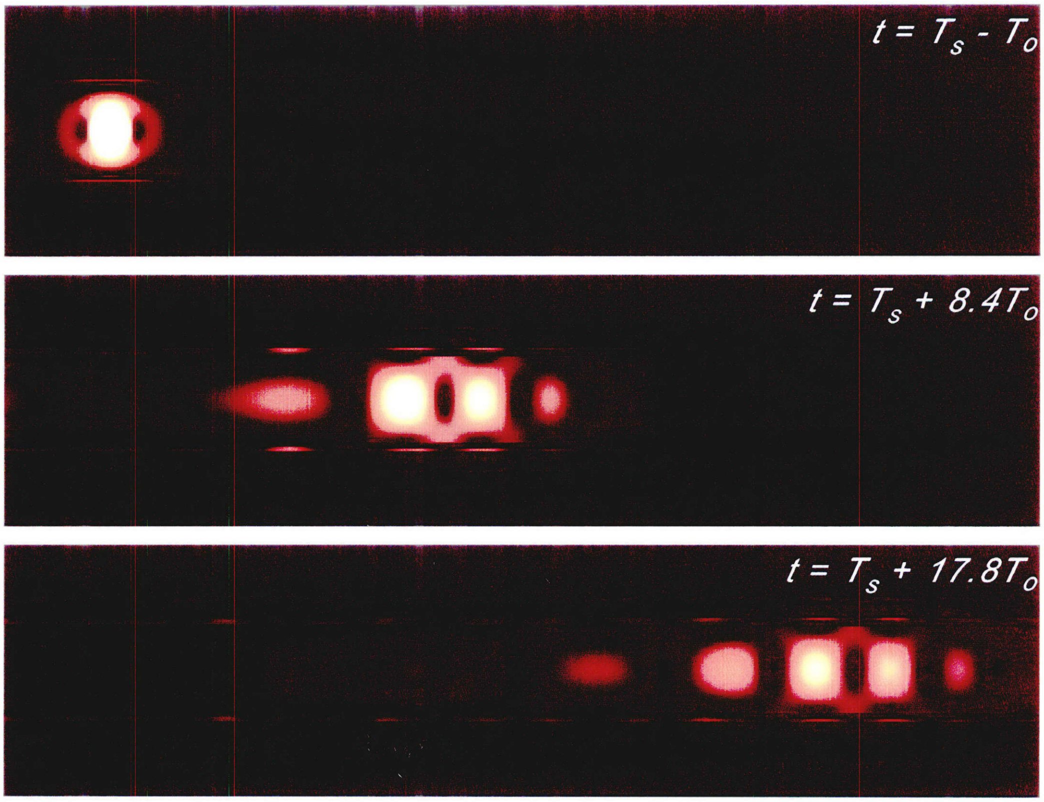

Figure 2-4: Snapshots of the distribution of electrical power in the waveguide for a single dipole at the center of the hollow core. Times are given here and in other figures relative to the time of peak emission, T_s, in units of the period of the central frequency, T_o.

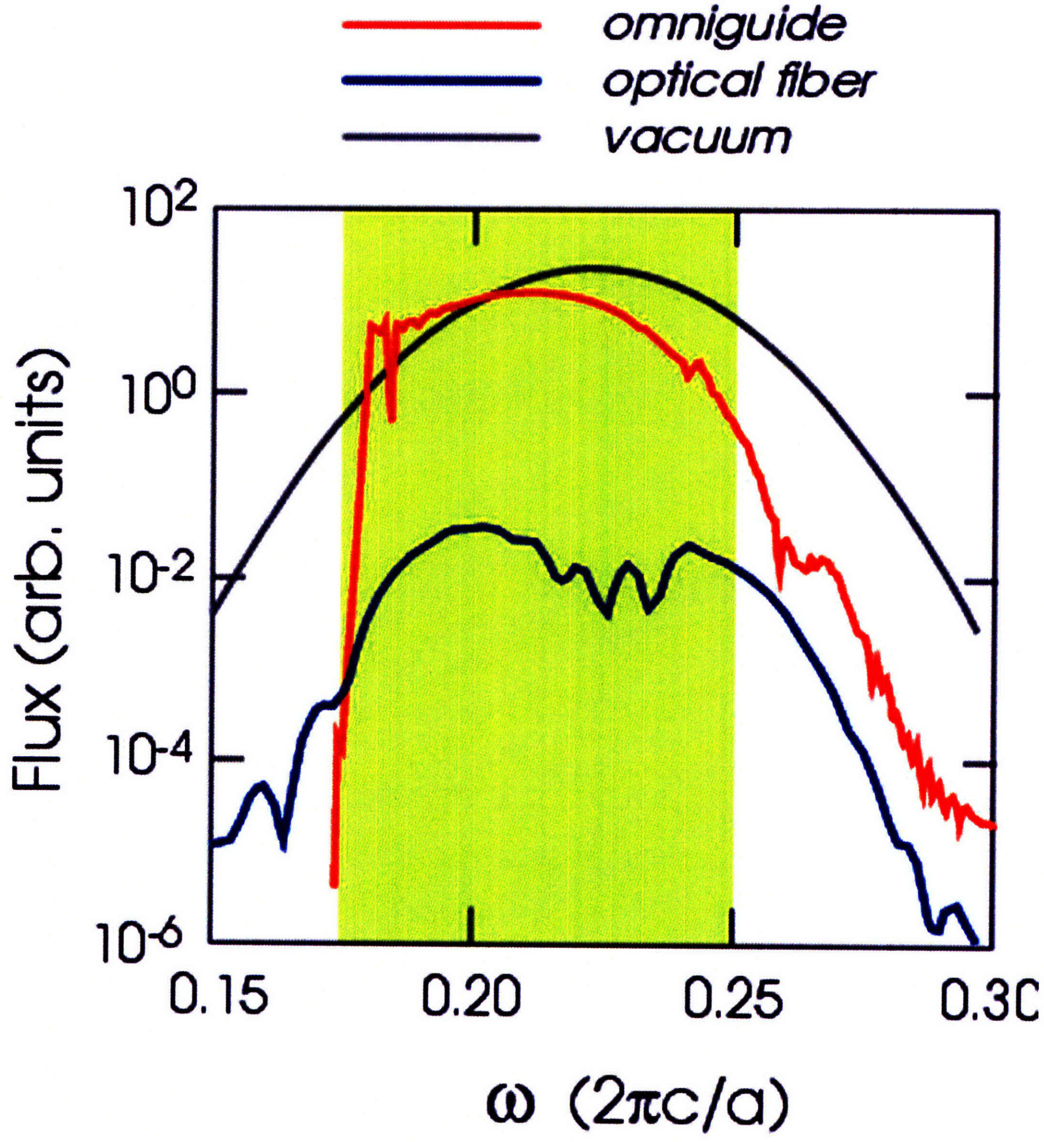

Figure 2-5: Flux spectrum for a dipole at the center of the hollow core, plus data for a hollow glass fiber ($n = 2.6$), and the total flux of the dipole in vacuum.

Clearly this formula can be generalized to accommodate multiple modes with these types of singularities characteristic of one-dimensional periodicity (van Hove-type singularities). To obtain a detailed comparison with time-domain simulations, however, the density of states, given formally by $g(\omega) = \sum_{n,k} \delta(\omega - \omega_{nk})$, was calculated numerically. The technique used involved a linear extrapolation of the eigenfrequencies calculated at a mesh of k-points, as described by Gilat and Raubenheimer [49]. The global density of states calculation is difficult to interpret, since in addition to several peaks from the resonant modes, there are many others from nearly degenerate index-guided modes. In order to isolate the important features of this density of states calculation, I look at the photonic local density of states, which is defined here as $g_L(\omega, \mathbf{r}) = \sum_{n,k} \epsilon(\mathbf{r}) \left|\mathbf{E}_{nk}(\mathbf{r})\right|^2 \delta(\omega - \omega_{nk})$, where the fields are normalized such that $\int \mathrm{d}\mathbf{r}\, \epsilon(\mathbf{r}) \left|\mathbf{E}_{nk}(\mathbf{r})\right|^2 = 1$, for all n and k, which implies that the global density of states can be recovered by integrating over all space, i.e., $g(\omega) = \int \mathrm{d}\mathbf{r}\, g_L(\omega, \mathbf{r})$.

The results obtained both at the center of the hollow cavity, and at a distance 1.2 times the lattice spacing away from the center, are shown in Fig. 2-6. In this case, the greatly decreased density of states within the bandgap below cutoff, and the enhanced density of states associated with the hollow core resonant modes, leads to enhanced emission just above cutoff for modes to which the dipole can couple.

This behavior shows that a cylindrically symmetric, omnidirectionally reflective coating can create an environment in which dipole emitters can efficiently couple into low-loss resonant modes in the hollow core. In Fig. 2-7, a different pulse is used to show the behavior near cutoff in more detail. While the total integrated power $\int F(\omega)\, \mathrm{d}\omega$ is greater for the dipole in the waveguide than in vacuum, that is not physically unreasonable since the conserved quantity in my simulations is simply the current, while power is given by the current acting against the local field, which may be selectively enhanced at certain frequencies and positions in the presence of a dielectric.

Next, I consider the behavior of a dipole close to the inner surface of the hollow tube (at $\rho = 2a$, with $r_i = 2.144a$). The flux spectrum for dipoles oriented in the ρ, θ and z directions (see Fig. 2-3) are shown in Fig. 2-8. In Figs. 2-9 through 2-11, the

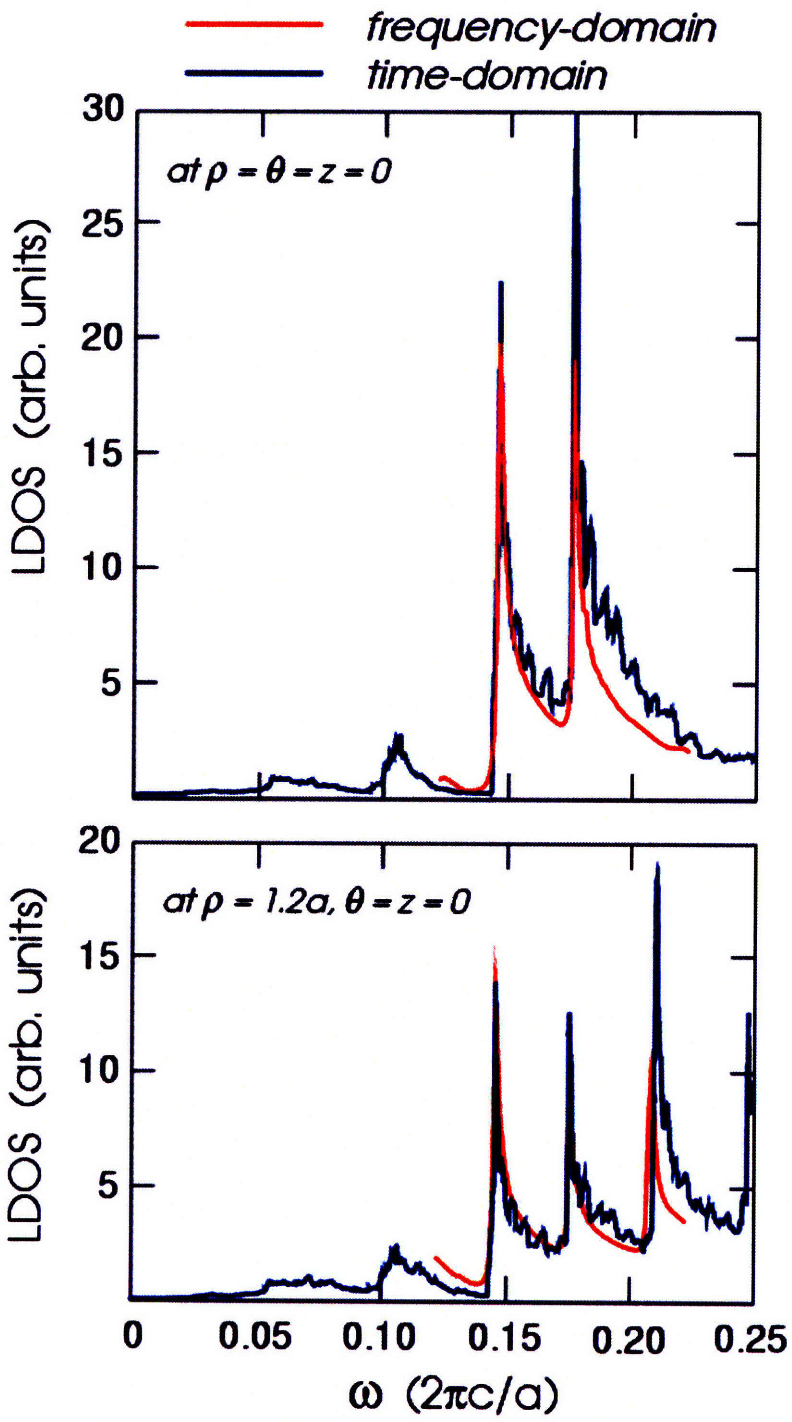

Figure 2-6: Local density of states for the hollow cylindrical waveguide. Note the presence of sharp $1/\sqrt{\omega - \omega_c}$-type singularities, as predicted.

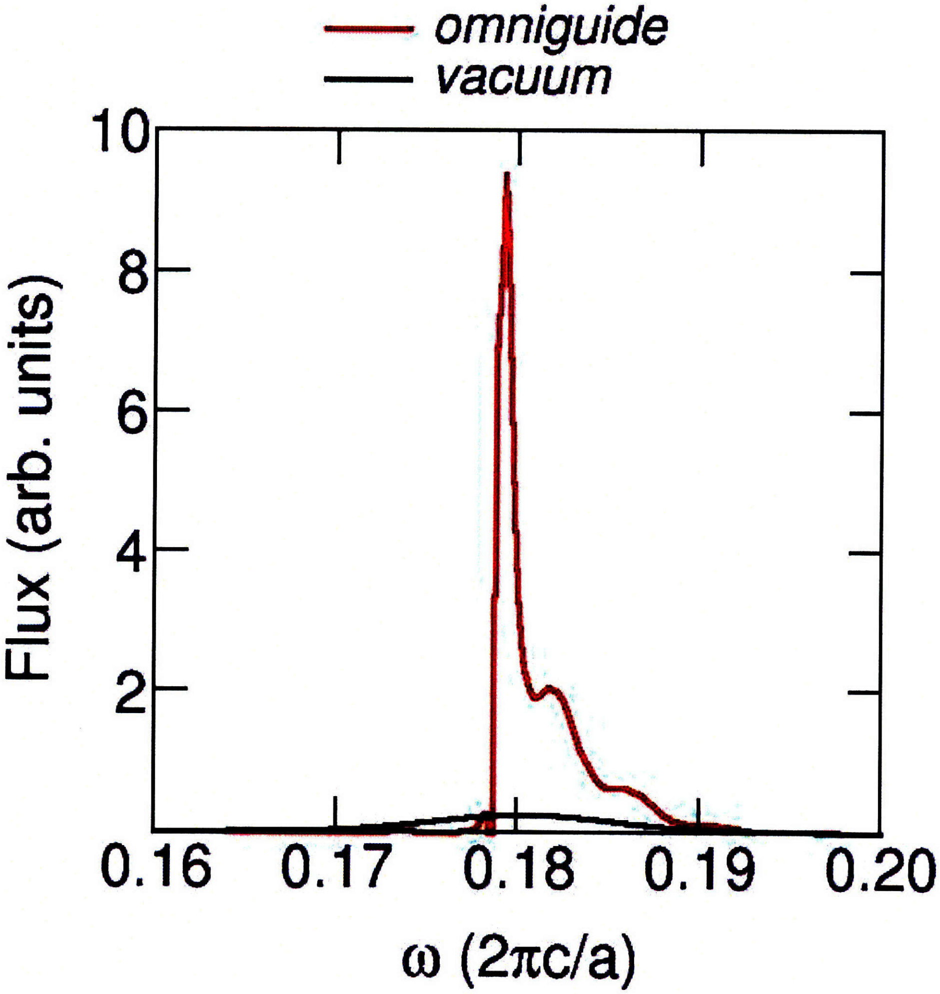

Figure 2-7: Flux spectrum for a dipole at the center of the hollow core, as in figure 2-5, but zoomed in on the region near cutoff.

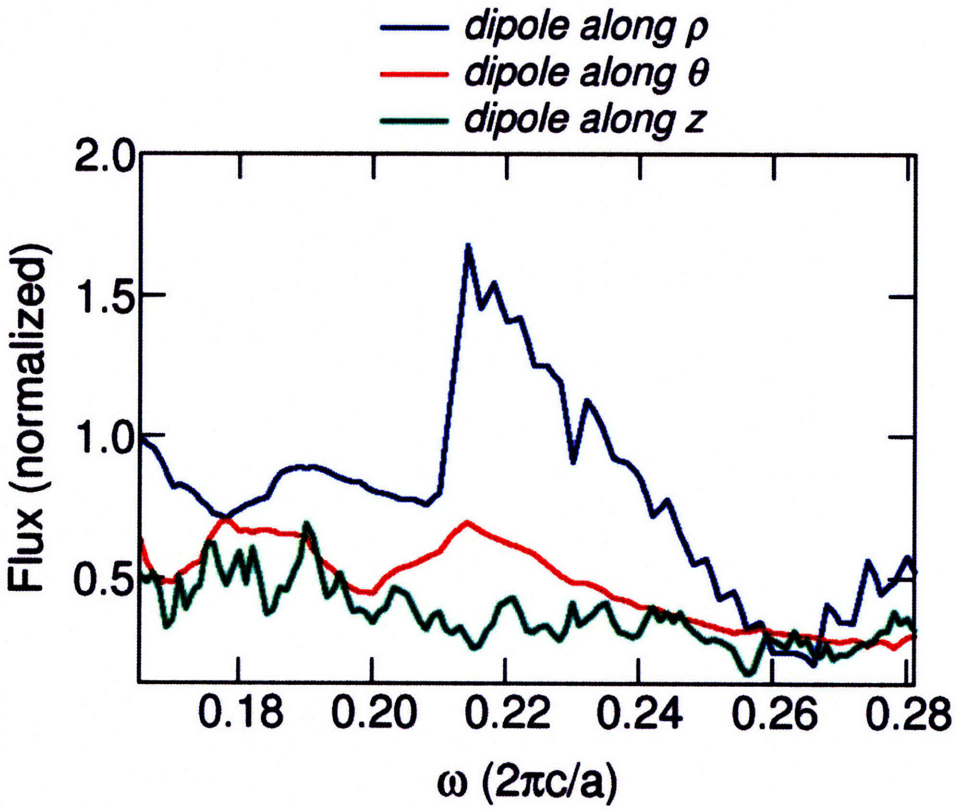

Figure 2-8: Flux spectrum for dipoles on the inner surface of the hollow core, oriented in the ρ, θ, and z directions, normalized by the flux of a dipole in vacuum.

redistribution of electric power as a function of time is shown for these same three orientations. Performance varies dramatically with the orientation of the dipole. The presence of a sharp rise in the transmission at a certain frequency can be interpreted as a cutoff corresponding to a hollow core guided mode. The lack of such a cutoff can generally be interpreted as a sign that any transmission would come through an index guiding mechanism. Thus, I surmise that a dipole oriented along ρ will couple much more efficiently to the hollow core guided modes than the dipoles pointing along θ or z. This interpretation is supported by the snapshots of the power distribution in Figs. 2-9 -2-11. Furthermore, a circular flow of energy is observed for the dipole oriented along z, as illustrated in Fig. 2-12.

Also, the behavior of a dipole intermediate between the inner surface and center of the hollow tube in the transverse direction (at $\rho = 1.2a$, with $r_i = 2.144a$) is considered. In contrast with the previous results for a dipole situated adjacent to the

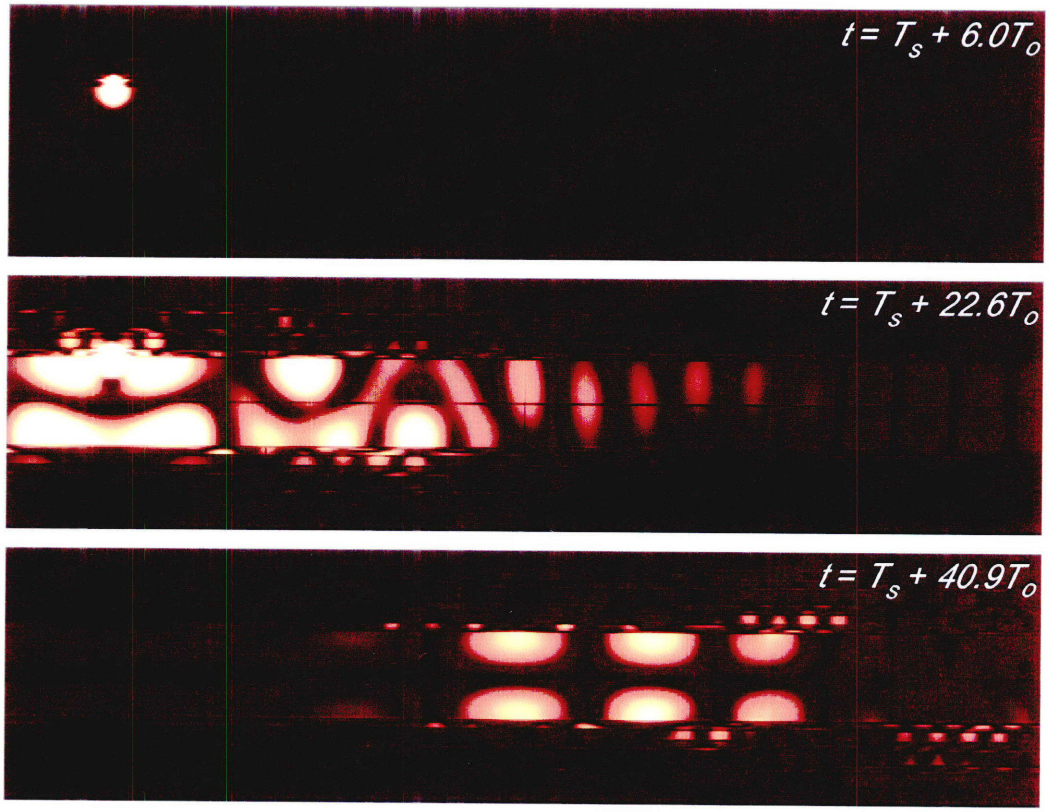

Figure 2-9: Snapshots of the distribution of electrical power in the waveguide for a single dipole source on the inner surface pointing in the ρ direction.

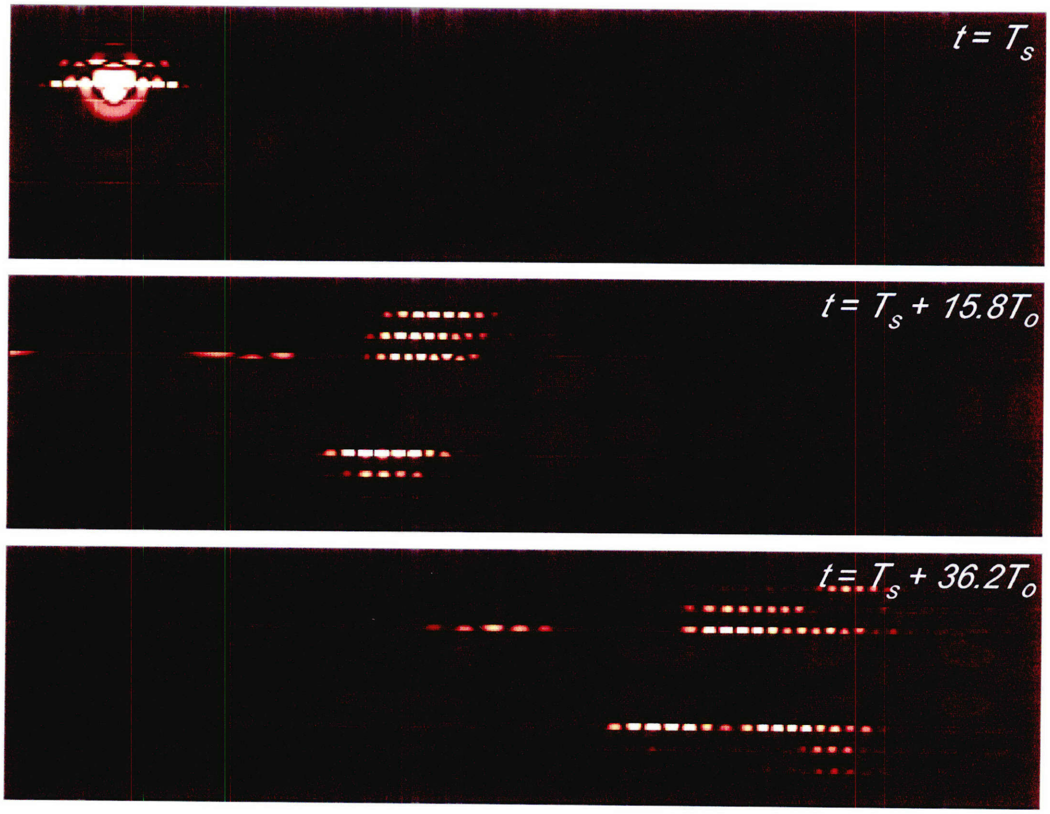

Figure 2-10: Snapshots of the distribution of electrical power in the waveguide for a single dipole source on the inner surface pointing in the θ direction.

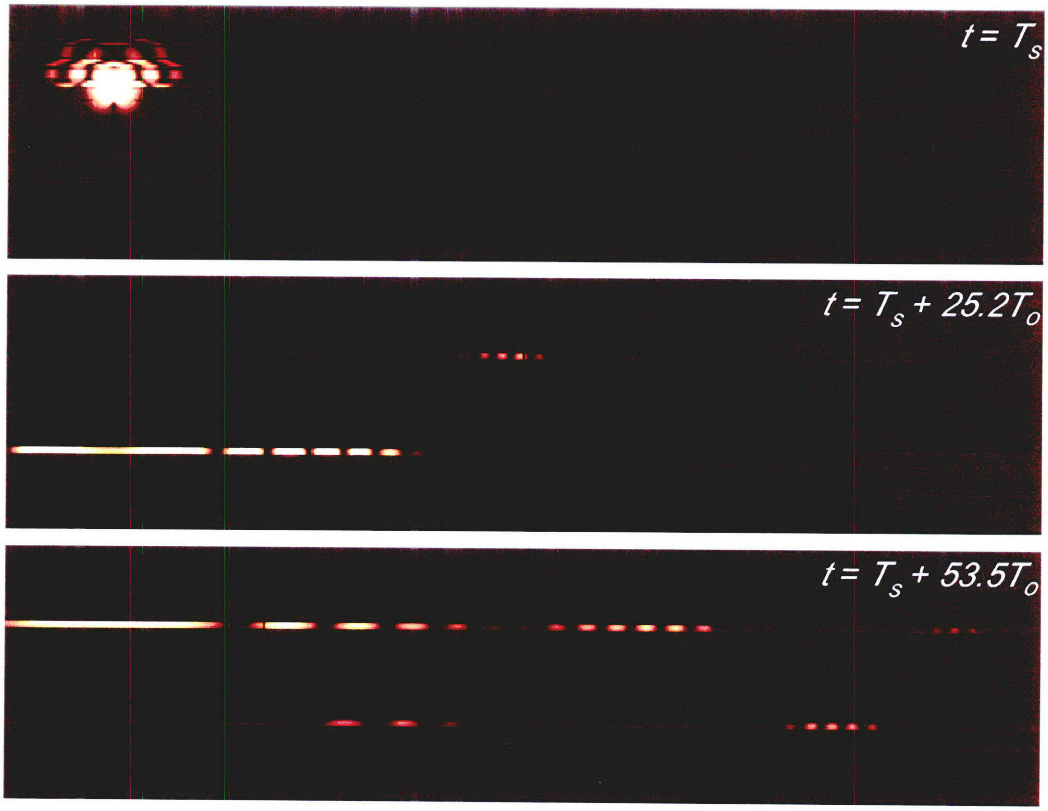

Figure 2-11: Snapshots of the distribution of electrical power in the waveguide for a single dipole source on the inner surface pointing in the z direction.

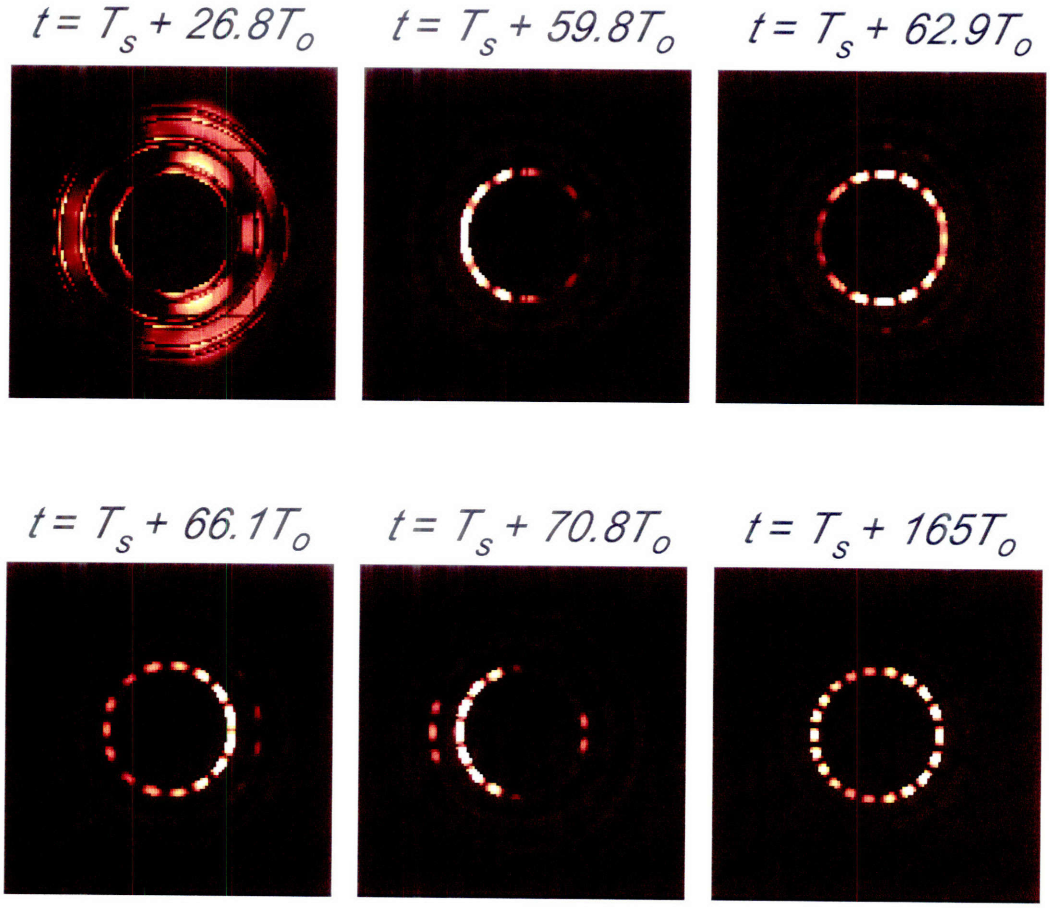

$t = T_s + 26.8T_o$

$t = T_s + 59.8T_o$

$t = T_s + 62.9T_o$

$t = T_s + 66.1T_o$

$t = T_s + 70.8T_o$

$t = T_s + 165T_o$

Figure 2-12: Snapshots of the distribution of electrical power in a cross section of the waveguide away from the source which is located near the wall ($\rho = 2a$, $r_i = 2.144a$), and pointing along z.

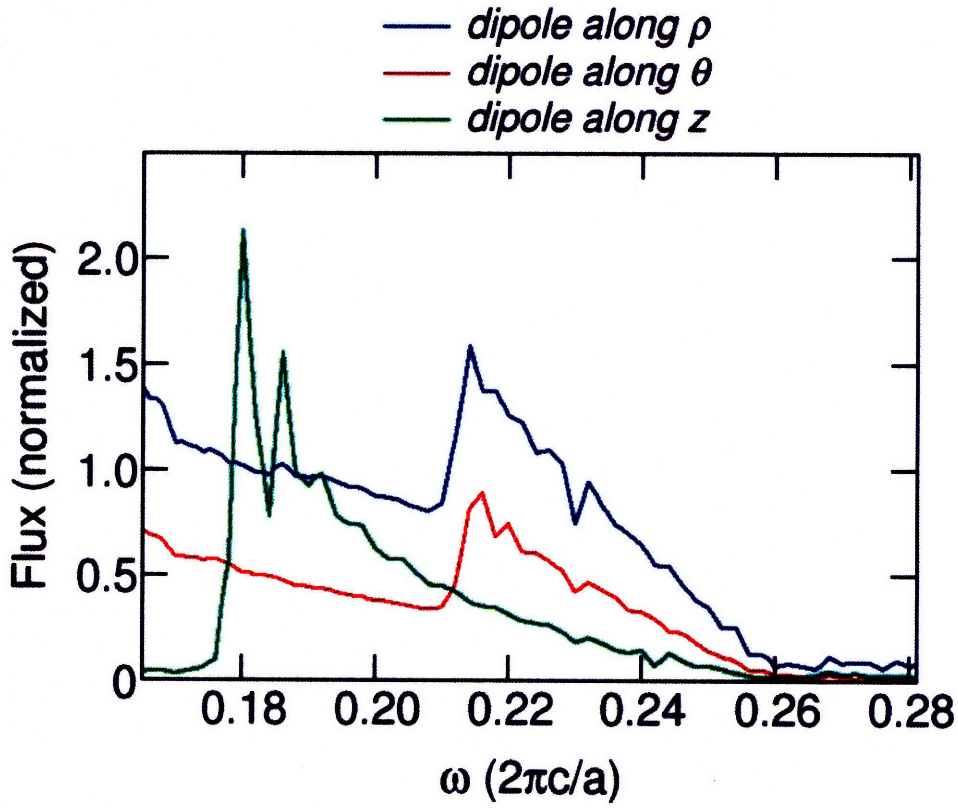

Figure 2-13: Flux spectrum for a dipole roughly halfway between the center and inner wall of the hollow core, i.e., at $\rho = 1.2a$ ($r_i = 2.144a$), normalized by the flux of a dipole in vacuum.

inner surface (see Fig. 2-8), the dipoles oriented along θ and z in this middle position are able to couple to the hollow core guided modes, as suggested by the presence of cutoffs in the flux spectra shown in Fig. 2-13. This is also illustrated more explicitly in Figs. 2-14 through 2-16, where all three orientations are shown coupling into these modes, in contrast with Figs. 2-9 through 2-11.

Evidently dipole sources near the inner core radius can have strong coupling to modes which exist in the dielectric cladding. This is consistent with the finding that the local density of states of an omnidirectional reflector is not zero, or even small, but instead characteristic of a waveguide [50]. In other words, they are index-guided modes. However, empirically, it is observed that the coupling of dipoles to these modes is decreased if they are at a distance of order $\lambda/4$ away from the inner surface. This analysis suggests that a low-index coating may prevent coupling to the problematic

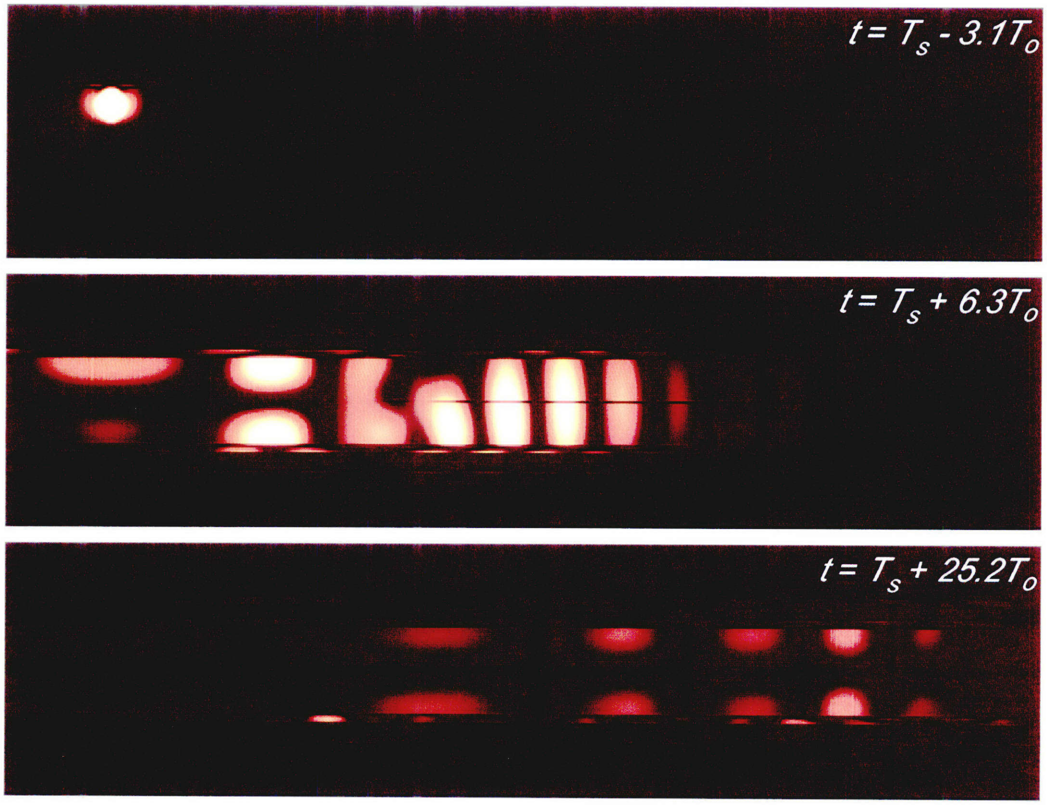

Figure 2-14: Snapshots of the distribution of electrical power in the waveguide for a single dipole source near the inner surface ($\rho = 1.2a$, $r_i = 2.144a$) pointing in the ρ direction.

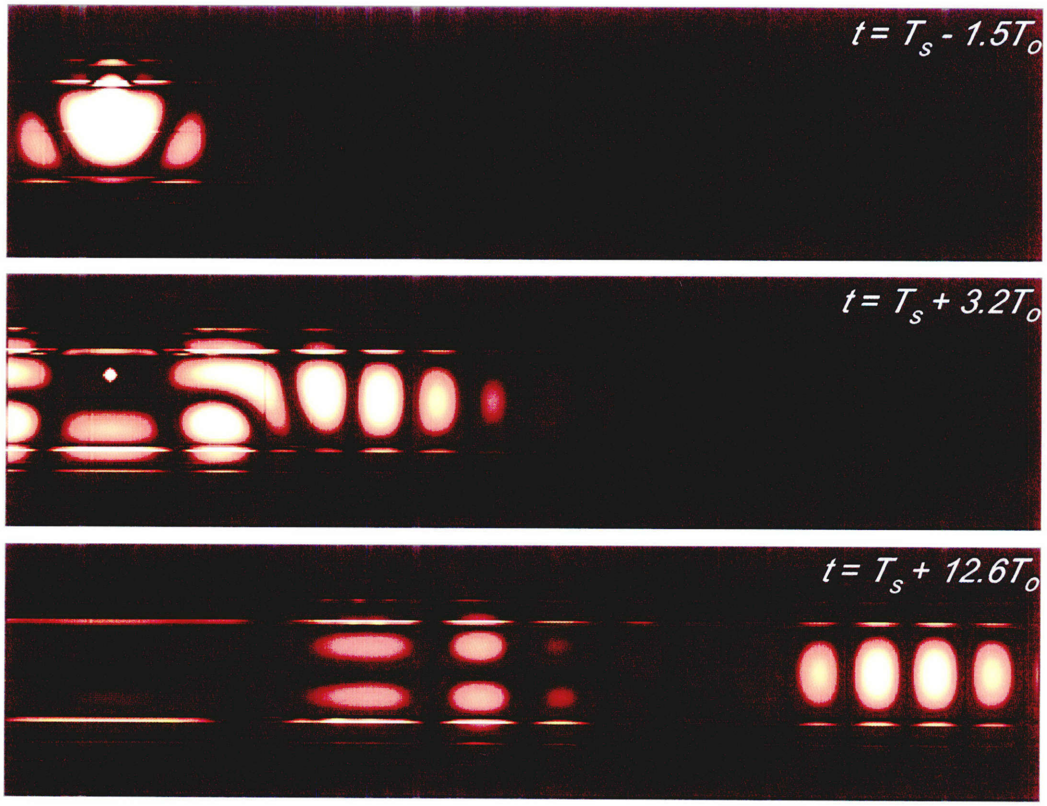

Figure 2-15: Snapshots of the distribution of electrical power in the waveguide for a single dipole source near the inner surface ($\rho = 1.2a$, $r_i = 2.144a$) pointing in the θ direction.

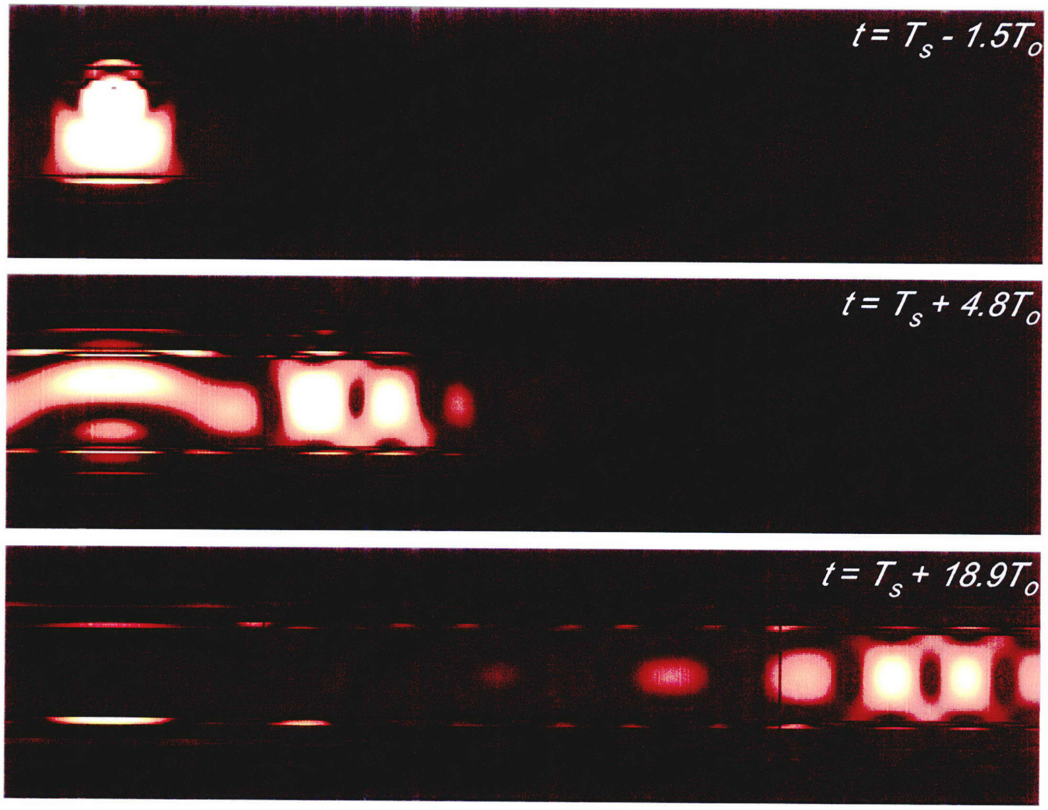

Figure 2-16: Snapshots of the distribution of electrical power in the waveguide for a single dipole source near the inner surface ($\rho = 1.2a$, $r_i = 2.144a$) pointing in the z direction.

index-guided modes. It may immediately be noted that as the index of the inner coating approaches unity, the performance should be the same as the case illustrated in Figs. 2-13 and 2-14 through 2-16, since the inner coating would just act like an extension of the hollow core. However, the yield of a hollow tube with a "low-index" ($n = 1.3$) coating which extends from $\rho = 1.2a$ to $\rho = 2.144a$ was also tested, and the result, as well as a comparison to the $n = 1$ case, is given in Fig. 2-17. It is found that if one couples to the appropriate modes which have frequencies within the range of omnidirectional reflection, efficiencies comparable to the previous case of a dipole away from the surface, essentially suspended in air, can be achieved. The propagation of this mode is illustrated in figure 2-18.

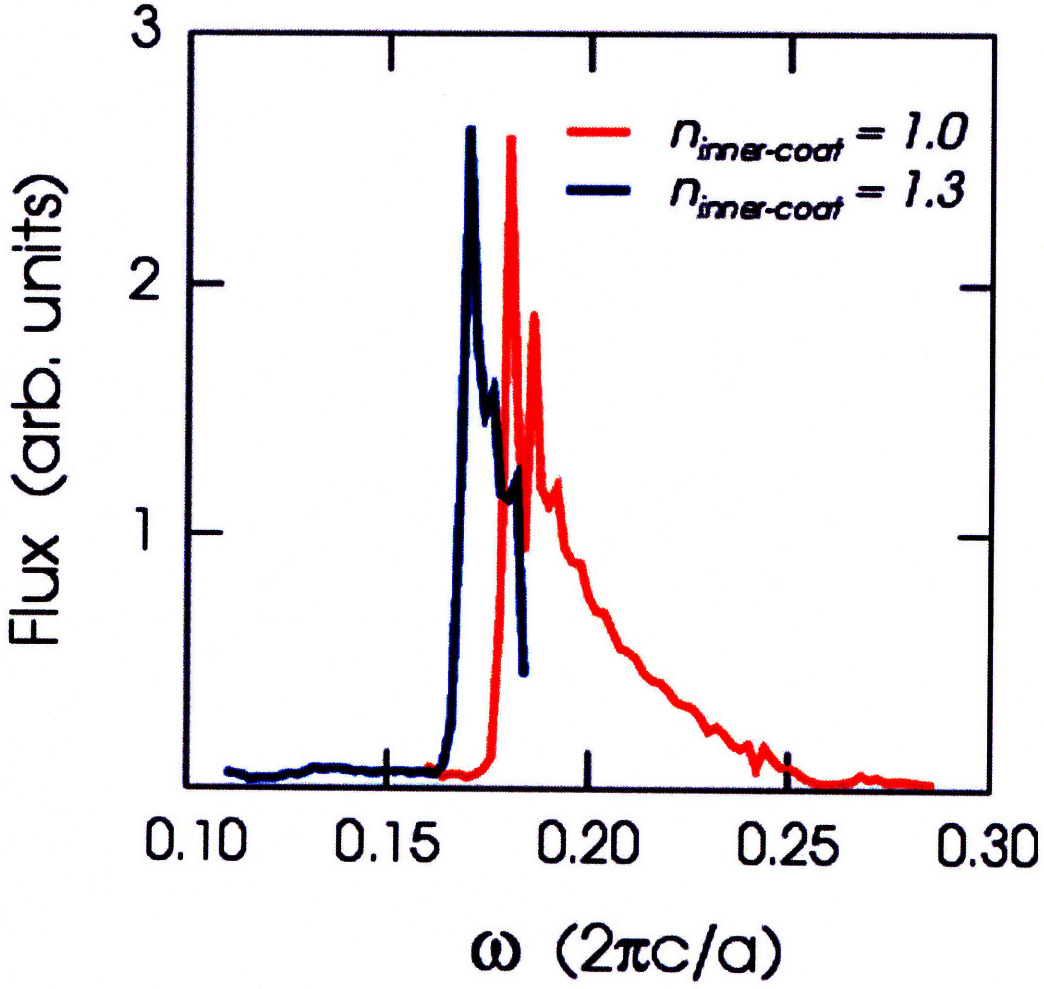

Figure 2-17: Flux spectrum for dipoles oriented along z situated on the inner wall of a medium-sized cell with an inner coating of low-index material ($n = 1.3$) extending from $\rho = 1.2a$ to $\rho = 2.144a$.

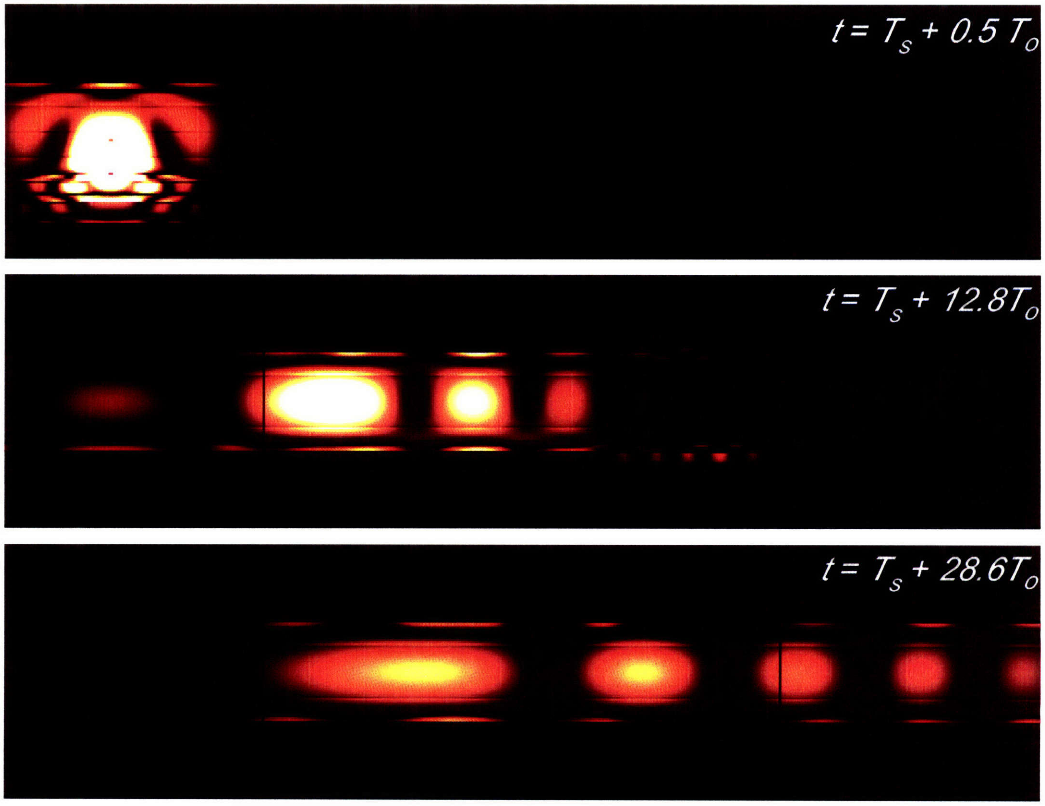

Figure 2-18: Snapshots of the distribution of electrical power in the waveguide for a single dipole source, oriented along z, on the inner surface of a cell with a coating of low-index material ($n = 1.3$) extending from $\rho = 1.2a$ to $\rho = 2.144a$.

Next, I calculate the dispersion of modes localized to the core. The dispersion of a wave packet with a relatively narrow range of frequencies is proportional to $d^2k_z/d\omega^2$ evaluated at the central frequency [51]. In terms of units useful for interpreting numerical calculations, the spatial separation accrued per unit frequency difference between waves per unit distance travelled along the waveguide, the dispersion is given by $D = (d\omega/dk_z)(d^2k_z/d\omega^2)$. It can be shown that for small k_z, which dominates the spontaneous emission spectrum, the dispersion is approximately proportional to the core index. This comes about from two competing effects. First, a lower group velocity decreases the spatial separation between nearby modes. However, a flatter band means there will be a greater spread of axial wavevectors. Since distance along the waveguide and frequency spread are held constant in the two simulations, the overall effect is an increase in the separation between modes in a system with a low-index coating, as can be observed by comparing figures 2-4 and 2-18.

Finally, I discuss one potential application: a detector for fluorescent molecules. One could design the omniguide to be transparent at excitation frequencies, and reflective at emission frequencies. Then, ideally, the spontaneously emitted radiation could only couple to hollow-core guided modes, which would propagate to the end of the waveguide with low losses. The important design considerations are as follows: making sure the fluorescent molecules do not couple to index-guided modes, choosing the core radius to control the available guided core modes, and choosing the number of layers to keep losses over the length of the omniguide acceptably low. The fluorescent molecules can be kept from coupling to index-guided modes by introducing a low-index coating, as discussed above. For an index-guided cladding mode near the light line, the damping factor over a distance x is given by $\exp\left[-2\pi\sqrt{n_h^2 - n_c^2}(x/\lambda)\right]$, where n_h is the refractive index of the high-index cladding layer and n_c is the refractive index of the low-index coating. For $n_h = 4.6$, $n_c = 1.2$, $x = \lambda/4$, this factor is 0.1%, which shows that a thin coating is more than sufficient for high-contrast materials.

The considerations involved in choosing the appropriate hollow omniguide geometry are covered in some detail in Ref. [19]. Applications of these principles to the detector application are briefly covered here. First, I consider the problem of choosing the appropriate mode. There are primarily TE and TM-like modes, which have an angular momentum m and index n. All properties of the TE modes can be calculated from $H_z = J_m(\omega\rho/c)e^{im\phi}$ subject to the boundary condition $\left.\frac{\partial H_z}{\partial \rho}\right|_{\rho=R} = 0$ (where R is the core radius). Similarly, TM modes have a scalar E_z which vanishes at $\rho = R$. It has been shown that TE_{0n} mode losses scale as $1/R^3$, and all other mode losses scale as $1/R$. However, there are 5 modes with equal or lower cutoff frequencies as the TE_{01} mode, including several doubly-degenerate modes. For simplicity, one may wish to restrict the fluorescent molecule to only couple to one mode. In this case, I choose the TM_{01} mode, which has a cutoff frequency of $\omega = 0.383/(r_i/a)$, where r_i is the inner core radius. Only the TE_{11} mode has a lower cutoff frequency ($\omega = 0.293/(r_i/a)$), though an emitter placed at the center can only couple to $m = 0$ modes (such as TM_{01}) due to the physical requirement that the fields be single-valued. Alternatively, one could choose the r_i to be small, for instance, $r_i = 2a$, so that the TE_{11} mode cutoff would be below the range of omnidirectional reflection, which would leave only the TM_{01} mode at the end of the omniguide. The last issue concerns choosing the appropriate number of cladding layers. The loss of a given mode for a given core radius and given number of layers can easily be calculated. For instance, a TM_{01} mode has a loss of 26 dB / cm for a radius of $6a$ and 4 bilayers of tellurium / polystyrene. If the target loss is 1 dB or less with a length of 1 cm of omniguide, the fact that TM losses decrease by a factor of 5 with each bilayer means that 6 cladding bilayers are needed.

2.4 Conclusion

In conclusion, I have shown that the radiation of electric dipole sources couples strongly to low-loss hollow-core guided modes of 1D periodic hollow omniguide structures. Furthermore, the rate of emission of these sources is controlled by the local density of states at its location and orientation. For states away from the inner surface, there are 1D van Hove singularities at the guided mode cutoff frequencies, just as in a metallic waveguide. This gives rise to spontaneous emission concentrated at frequencies just above cutoff, a substantial departure from the vacuum case. Strong modification of spontaneous emission has been already observed experimentally [44] for a metallodielectric photonic crystal. There is a potential problem for detection applications that sources near the inner surface can couple into guided modes in the dielectric cladding layers. Fortunately, this undesirable behavior can be reduced substantially through the introduction of a low-index coating on the inner surface of the hollow core.

Chapter 3

Active materials embedded in photonic crystals and coupled to electromagnetic radiation

3.1 Introduction

The interaction of light with active materials can give rise to a rich variety of physical phenomena, such as material dispersion [52], plasmons [53], polaritons [54], and spontaneous and stimulated emission [55]. These phenomena are the basis of a wide variety of technologically important devices, such as fiber optics [52], lasers [52], and photovoltaic cells [56]. They can all be understood with the semi-classical physical model of harmonic oscillators coupled to electromagnetic fields. However, while simple analytical expressions can be written down, precise solutions for realistic systems require a numerical solution. The most detailed model of four-level atomic systems tracks fields and occupation numbers at each point of the computational cell, taking into account energy exchange between atoms and fields, electronic pumping, and non-radiative decays [55].

This chapter aims to apply a detailed computational model to the problem of lasing. The basics of optical lasing have been understood theoretically since 1958: an atomic system is put in a resonant cavity and excited to a population inverted state, which then leads to stimulated emission of coherent photons [57]. Quantities such as lasing threshold and efficiency can be calculated approximately using simple analytical expressions. However, exact calculations of efficiency or non-equilibrium dynamics are still considered to be challenging. Many groups in the past have employed approximations to simplify their calculations, e.g., using a current source [58], a fixed conductivity [59], or randomly distributed dipole sources [60, 61]. In an attempt to achieve more realistic simulations, it has been shown that 2-level Maxwell-Bloch equations can be solved using iterative predictor-corrector FDTD methods to demonstrate saturation and self-induced transparency [62, 63]. This approach has also been applied to objects with 1D periodicity which may act as couplers, modulators, and switches [64], and has been extended to 3-level atoms using pseudospin equations [65]. In another line of research, researchers have now begun to study random laser systems by directly simulating semiclassical atoms interacting with electromagnetic fields. This work began with simulations of 4-level atoms in 1D that demonstrated lasing is indeed possible in random systems [66, 67, 68]. More recent work demonstrates that random arrangements of 2D rods can also give rise to random lasing [69, 70]. A much more thorough review of recent work in random lasing, both theory and experiment, can be found in Ref. [71]. Along slightly different lines, using 2-level Maxwell-Bloch equations, it has been shown that electrically-pumped atoms inside a 2D high-index cavity can give rise to lasing [72]. On a related note, Ref. [73] has developed a simulation scheme for 4-level 2-electron atomic systems which demonstrate a different lasing threshold than observed for the semiclassical lasing equations in Ref. [55].

Nonetheless, all of these calculations have been done in 1D or 2D systems. And to the best of my knowledge, have not been applied to photonic crystals with periodicity in more than one direction. In this chapter, this type of approach is extended to 3D systems, and results are obtained for photonic crystal systems of each dimensionality. This chapter begins with a discussion of the computational approach and verification of the code with an analytically soluble problem. This code is then applied to a Fabry-Perot cavity with atomic material in the defect region. Next, a 2D problem is considered, a photonic crystal consisting of a square lattice of rods with a line of defects. Finally, a 3D problem is considered, a cylindrical photonic crystal with a region of atomic material.

3.2 Theory

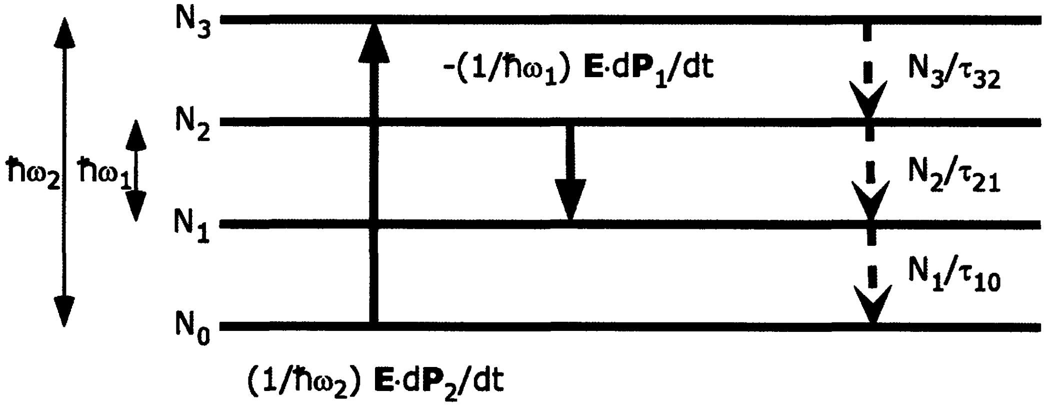

Figure 3-1: Relationships between energy levels in the four-level atomic system used in this chapter. Straight lines correspond to radiative transitions; dashed lines correspond to non-radiative transitions.

The theoretical approach is as follows. The electric fields and occupation numbers N_j for a four-level atomic system ($j = 0, 1, 2, 3$) are modeled semi-classically, with all quantities being tracked at every point in the computational cell (following Ref. [55]). Maxwell's equations are given by $\nabla \times \mathbf{E} = -(1/c)\partial\mathbf{H}/\partial t$ and $\nabla \times \mathbf{H} = 4\pi\mathbf{j}/c + (1/c)\partial\mathbf{D}/\partial t$ with the constitutive relation $\mathbf{D} = \epsilon_p\mathbf{E} + 4\pi\sum_{i=1,2}\mathbf{P}_i$, where ϵ_p is the dielectric function of the passive medium (i.e., in the absence of active materials), and where $\mathbf{P}_i$ is the ith electronic polarization density of the active material. This polarization density behaves as a harmonic oscillator driven by the product of the external field and the population inversion, and is given by:

$$\frac{d^2\mathbf{P}_i}{dt^2} + \Gamma_i\frac{d\mathbf{P}_i}{dt} + \omega_i^2\mathbf{P}_i = \sigma_i\Delta N_i\,\mathbf{E}, \tag{3.1}$$

where Γ_i is the nonradiative decay width for $\mathbf{P}_i$, σ_i is the coupling strength of $\mathbf{P}_i$ to the external electric field, and $\Delta N_1 = N_1 - N_2$ and $\Delta N_2 = N_0 - N_3$ are the population inversions that drive the polarizations. The occupation numbers vary according to the following equations:

$$\frac{dN_3}{dt} = \frac{1}{\hbar\omega_2}\mathbf{E}\cdot\frac{d\mathbf{P}_2}{dt} - \frac{N_3}{\tau_{32}} \tag{3.2}$$

$$\frac{dN_2}{dt} = \frac{1}{\hbar\omega_1}\mathbf{E}\cdot\frac{d\mathbf{P}_1}{dt} + \frac{N_3}{\tau_{32}} - \frac{N_2}{\tau_{21}} \tag{3.3}$$

$$\frac{dN_1}{dt} = -\frac{1}{\hbar\omega_1}\mathbf{E}\cdot\frac{d\mathbf{P}_1}{dt} + \frac{N_2}{\tau_{21}} - \frac{N_1}{\tau_{10}} \tag{3.4}$$

$$\frac{dN_0}{dt} = -\frac{1}{\hbar\omega_2}\mathbf{E}\cdot\frac{d\mathbf{P}_2}{dt} + \frac{N_1}{\tau_{10}} \tag{3.5}$$

Terms such as $(\mathbf{E}\cdot d\mathbf{P}_1/dt)/\hbar\omega_1$ represent the conversion between atomic potential energy and field energy at a certain rate. A population inversion will drive the polarization field $\pi/2$ radians out of phase with the external electric field, which converts atomic potential energy into field energy – the semiclassical version of stimulated emission. Other terms such as N_2/τ_{21} are non-radiative decays between adjacent levels; this energy is considered to be lost. The interactions between the energy levels are illustrated in Fig. 3-1. Decay rates play an important role in determining the efficiency of any optical pumping process. In this chapter, efficiency is defined as the ratio of the number of optical transitions at the emitting frequency to the number of optical transitions at the absorbing frequency, i.e.,

$$\eta = \frac{\hbar\omega_2 \int_0^\infty dt \left[\mathbf{E}\cdot\frac{\partial\mathbf{P}_1}{\partial t}\right]}{\hbar\omega_1 \int_0^\infty dt \left[\mathbf{E}\cdot\frac{\partial\mathbf{P}_2}{\partial t}\right]}. \tag{3.6}$$

This quantity effectively measures the competition between radiative and non-radiative decay processes, and approaches one in the limit where the stimulated emission rate is much greater than the non-radiative decay rate. As a result, η will generally go up with incoming beam power, as well as with an increase in the lifetime of the metastable state τ_{21}. This relationship, which includes lasing threshold-type behavior, is quantified later in this chapter.

In order to solve the behavior of active materials in electromagnetic fields numerically, the finite-difference time domain (FDTD) technique [47] is utilized, using an approach similar to the one outlined in Ref. [67]. Both time and space are discretized into steps small compared to the characteristic periods and wavelengths of the problem, and at each point the electric, magnetic, and polarization fields are initialized to zero, while the atomic fields are initialized to their ground states. The following steps are taken to evolve the fields in time. First, the polarizations are integrated through one time step using equation (3.1) (tracking the two values at each point needed for any second order ODE). Next, the electric fields are integrated according to the Maxwell-Ampère law (which includes subtracting the polarizations from the electric field). Finally, the atomic occupations N_j are integrated according to equations (3.2-3.5), and the magnetic fields are integrated according to Faraday's law (these last two steps can be done in either order). The cycle repeats for each time step until all the electric, magnetic, and polarization fields have decayed to negligible magnitudes.

In this work, stimulated emission at frequency ω_1 is desired, which requires a population inversion between the two intermediate levels separated by energy $\hbar\omega_1$. Photonic crystals can enhance such stimulated emission when the absorption and emission frequencies and widths are chosen so that an excitation frequency above the photonic bandgap drives atomic material present in a defect region to emit into a resonant mode inside the bandgap. For generality, I choose to model the active material as an adjustable four-level atomic system. The field amplitudes, coupling strengths and decay rates are chosen to ensure that a substantial fraction of atoms absorb fields of frequency ω_2, and then produce a population inversion, thereby amplifying fields of frequency ω_1. The decay times τ_{32} and τ_{10} are chosen to be quite small, e.g., 200 time steps, just large enough to achieve a smooth decay curve for the upper level. The decay time τ_{21} is chosen to be several orders of magnitude larger than the other decay times, τ_{32} and τ_{10}, to simulate a metastable state. Clearly, the conversion between the excitation and emission frequencies will be most efficient for the largest values of τ_{21}. Furthermore, the decay widths should be chosen so that the width associated with the higher frequency absorbing transition, Γ_2, is relatively large to maximize absorption, and so that the width associated with the lower frequency emission transition, Γ_1, is relatively small, in order to match the quality factor of the resonant mode in the photonic crystal. The choice of coupling strengths σ_i and field amplitudes are closely related. The appropriate values can be calculated through the following approach. First, note that in a steady state, $\mathbf{P}_i(\omega) = \frac{\sigma_i \Delta N_i}{\omega_i^2 - \omega^2 - i\omega\Gamma_i}\mathbf{E}(\omega)$. As a result, the on-resonance response to a continuous wave (cw) source in the time-domain will be $\mathbf{P}_i(t) = \frac{\sigma_i \Delta N_i}{-i\omega_i \Gamma_i}\mathbf{E}(t)G(t)$, where $G(t)$ is a turn-on function that rises from 0 to 1 as one approaches the steady state, with the approximation of constant ΔN_i. The total radiative population transfer from the ground state to the metastable excited state can then be estimated from equation (3.2) to be $N_2 \approx \frac{\sigma_2 \Delta N_2}{\hbar \omega_2 \Gamma_2} \int dt \, [\mathbf{E}(t)]^2 G(t)$ for a cw source (assuming the population transferred to level 3 quickly drops down to level 2 and then stays there). For a pulsed source with a finite spectral width, but a duration greater than the turn-on time (which should be a few periods), I can simplify my expression by setting $G(t) = 1$, and then transform to the frequency domain using Parseval's theorem. I then keep all frequencies close to the resonant frequency (within $\pm\Gamma_2/2$), and discard the rest, which yields:

$$N_2 \approx \frac{\sigma_2 \Delta N_2}{\hbar \omega_2 \Gamma_2} \int_{\omega_2 - \Gamma_2/2}^{\omega_2 + \Gamma_2/2} |E(\omega)|^2 \, d\omega \equiv \frac{\sigma_2 \Delta N_2}{\hbar \omega_2 \Gamma_2} I_2, \tag{3.7}$$

where I_2 is an intensity integral whose numerical value is given later for each simulation with a pulsed source. Equation (3.7) can readily be used to calculate the field amplitudes needed to achieve a given level of population inversion in the limit that ΔN_2 is approximately constant. Now, I seek to calculate the criteria for lasing. I assume a resonant mode of a high-Q cavity with frequency ω_1 is initially excited at time 0 with a small amplitude. The associated polarization field is expected to have the form $P_1 = P_0 e^{-i\omega_1 t} e^{\alpha t}$, where α is a growth rate that is assumed to be small relative to the frequency ω. Then I can substitute into equation (3.1) to find that, to the lowest order in α, $2\alpha + \Gamma_e = (\sigma_1/\omega_1) \left| \Delta N_1(0) E / P_1 \right|$, where the $\Delta N_1(0)$ is the initial population inversion, and $\Gamma_e = \Gamma_1 + 2\tau_{21}^{-1}$ is the total loss rate for a pulsed excitation, while $\Delta N_1(0) \rightarrow \Delta N_1$ and $\Gamma_e = \Gamma_1$ for a continuous wave pulse. In order to achieve exponential growth of the mode, it must then be the case that

$(\sigma_1/\omega_1)\,|\Delta N_1(0)E/P_1| > \Gamma_e$. If the system reaches the regime where the electric field is driven by the polarization field, i.e., $E = -4\pi P_1$, then I obtain the condition for sustainable growth, $|\Delta N_1(0)| > \omega_1\Gamma_e/4\pi\sigma_1$.

3.3 Simulations

3.3.1 Two-level atomic system

The first simulation checks the agreement of the code with an analytical model for the upper level occupation. It can be shown that for a two-level atomic system stimulated by an external plane wave cw source with a finite rate of non-radiative decay, the steady-state upper level occupation N_2 should behave as:

$$N_2 = \frac{1}{2}\left[\frac{1}{1+\left(\frac{\hbar\omega\Gamma}{\tau\sigma}\right)\frac{1}{|E|^2}}\right], \tag{3.8}$$

where $|E|$ is the amplitude of the external plane wave cw source, ω is the frequency of the source and the atomic resonance, Γ is the width of the atomic resonance, τ is the rate of non-radiative decay, and σ is the coupling strength.

A series of simulations are then performed in which a slab of the two-level atomic material is subjected to a cw source of frequency $\omega = 0.25(2\pi c/a)$ (where a is the period of a photonic crystal), and allowed to equilibrate. This is done for two cases: an atomic slab surrounded by vacuum, and an atomic slab enclosed in a Fabry-Perot cavity with 3 quarter-wave thick layers of polystyrene ($n = 1.6$) and indium phosphide ($n = 2.97$). The cavity is designed to exhibit a resonance at the cw source frequency. The steady state upper occupation number is then measured for a series of different values of the incident field amplitude. As can be seen in Fig. 3-2, the simulation nicely reproduces the analytical prediction for both cases. There are two regimes for both curves in this figure. For low field amplitudes ($|E| \ll \sqrt{\hbar\omega\Gamma/(\tau\sigma)}$), the occupation grows quadratically with field amplitude (i.e., $N_2 \approx (\tau\sigma/(2\hbar\omega\Gamma))\,|E|^2$), which corresponds to the physical picture that the atoms absorb a fixed fraction of the incident light, as would be seen in a non-atomic material with a constant conductivity. On the other hand, for large field amplitudes ($|E| \gg \sqrt{\hbar\omega\Gamma/(\tau\sigma)}$), the occupation saturates to the maximum value of one-half (corresponding to equal occupations of the upper and lower levels). In this simulation, I choose $\hbar\omega\Gamma/\tau\sigma = 0.8$ and find that the curve of Fig. 3-2 precisely follows the analytical prediction of equation (3.8). The saturation occurs significantly earlier for the Fabry-Perot cavity because of the substantial resonant enhancement of electric field magnitudes, which also enhances polarization field magnitudes and the energy transfer rate. This phenomenon can also be viewed as an effective increase in the coupling strength of the polarization to the external field. For this calculation, a cavity with $Q = 38$ shows an effective coupling enhancement factor of 24. Higher quality factors should lead to even greater enhancements of the effective coupling.

3.3.2 Four-level atomic system

In this section, I consider a series of simulations in which a slab of four-level atomic material surrounded by vacuum is subjected to a cw source and allowed to equilibrate. The intensity of the cw source is varied, and then the power absorbed at the cw source frequency ω_2 is measured and compared to the power emitted at the target emission frequency ω_1. For the absorption frequency, I use $\omega_2 = 0.4(2\pi c/a)$, $\sigma_2 = 0.001(2\pi c/a)^2$, and $\Gamma_2 = 0.01(2\pi c/a)$; for the emission frequency, I use $\omega_1 = 0.2(2\pi c/a)$, $\sigma_1 = 0.02(2\pi c/a)^2$, and $\Gamma_1 = 0.001$. For the decay parameters, I use $\tau_{32} = 2.5(a/c)$, $\tau_{21} = 62.5(a/c)$, and $\tau_{10} = 2.5(a/c)$. The results for power emitted versus power absorbed are plotted in Fig. 3-3. According to section 3.2, I expect the threshold to be crossed when $|\Delta N_1| > (\omega_1\Gamma_1/\sigma_1)\,|P_1/E| \approx 0.0132/4\pi$, since $|P_1/E| = 1.32/4\pi$ in my calculation. For the first point above threshold, where $P_{in} = 0.00304$ and $P_{out} = 0.000149$, $\Delta N_1 = 0.0157/4\pi$, which is just above the critical value required for lasing. This demonstrates that lasing can occur in this system, and that I am able to accurately predict the onset of lasing behavior. However, I am obliged to include the caveat that in a cavity, the rate of spontaneous emission will be modified in a way that is not included in the framework of my calculations.

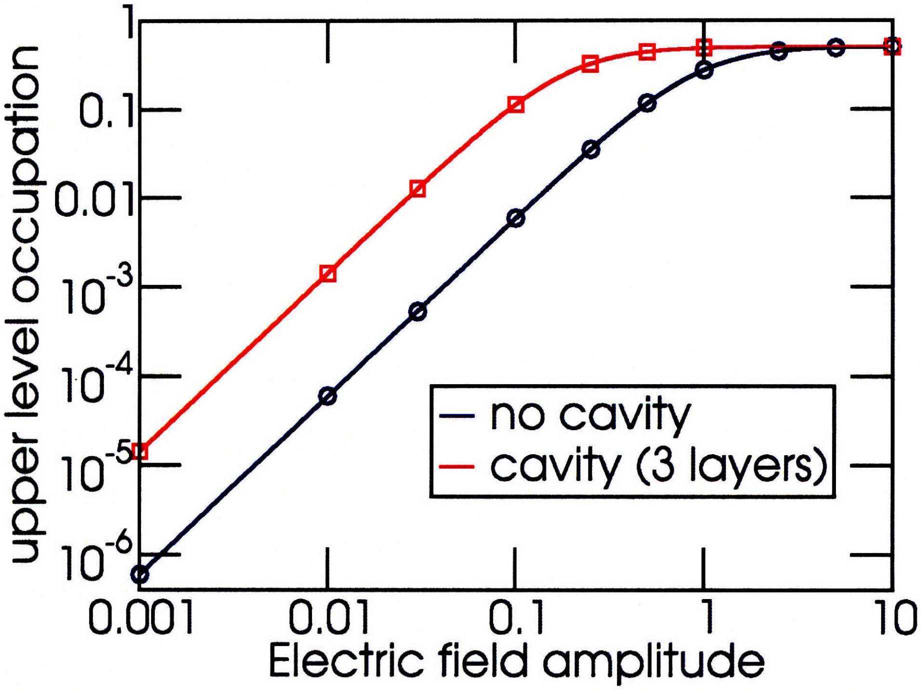

Figure 3-2: Fractional occupation of the upper level of a two-level atomic system as a function of field amplitude, with and without a cavity. The symbols are simulation data, and the smooth curve represents a fit to equation (3.8). Two regimes are seen: at low field amplitudes, occupation goes up linearly with field intensity, and at high field amplitudes, occupation saturates at one-half. Saturation occurs more quickly with a cavity due to the enhancement of stimulated emission.

Therefore, while I observe that lasing occurs in the rest of the systems in the numerical part of this chapter for sufficient power levels, I note that the threshold could be slightly higher than I calculate with this calculational scheme (but still substantially lower than in vacuum). In any case, despite this limitation, I am confident that lasing should still occur for sufficient power, and therefore the results in the subsequent sections should be considered essentially valid. Also, note that the efficiency η associated with these processes will be given by the ratio of actual P_{out} to the theoretical limit $(\omega_1/\omega_2)P_{in}$, and will approach unity for values well above threshold.

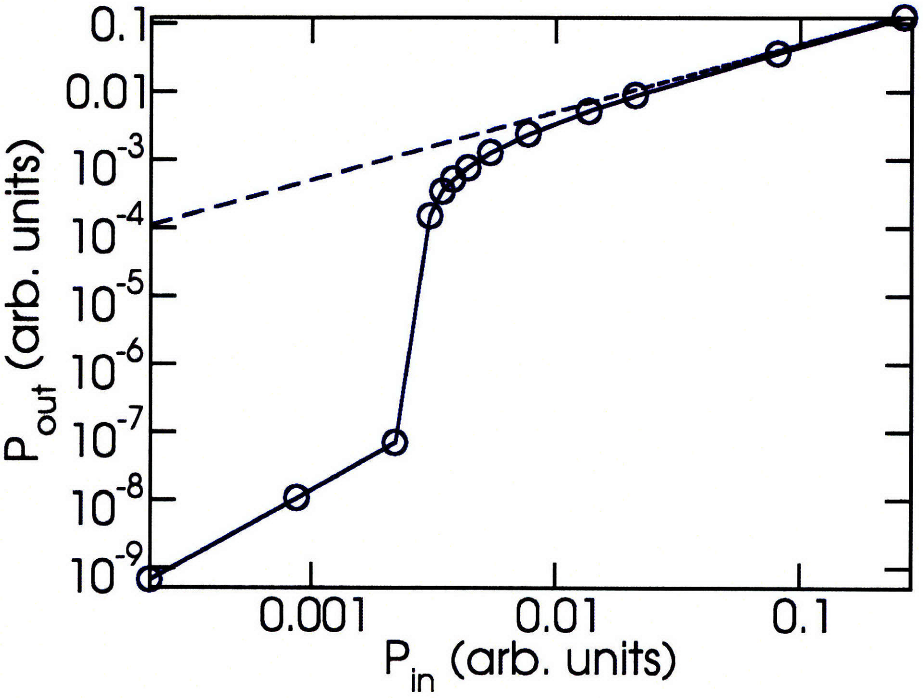

Figure 3-3: Graph of power emitted at $\omega = \omega_1$ vs. power absorbed at $\omega = \omega_2$ (both measures of power are in the same units). The dotted line corresponds to the maximum conversion efficiency for the values of ω_i used in this calculation. Notice a sharp rise in emission around $P_{in} \approx 0.003$, which corresponds to the lasing threshold for this system.

3.3.3 Four-level atomic system in a Fabry-Perot cavity

Having verified that the code behaves properly, now consider a slightly more complex 1D system, as illustrated in Figs. 3-4 and 3-5. It consists of a Fabry-Perot etalon, made of four and a half bilayers of the high contrast dielectric materials tellurium ($n = 4.8$) and polystyrene ($n = 1.6$), enclosing a cavity of length $2.5a$ containing four-level atomic material described by equations (3.2)-(3.5). A Gaussian plane-wave source with central frequency $\omega = 0.4(2\pi c/a)$ is used to optically pump atoms contained inside the defect cavity that absorb at the same frequency $\omega = 0.4(2\pi c/a)$, with width $\Gamma = 0.001(2\pi c/a)$, and re-emit at the resonant frequency $\omega = 0.2(2\pi c/a)$, with width $\Gamma = 0.001(2\pi c/a)$. This traps light, thus encouraging stimulated emission.

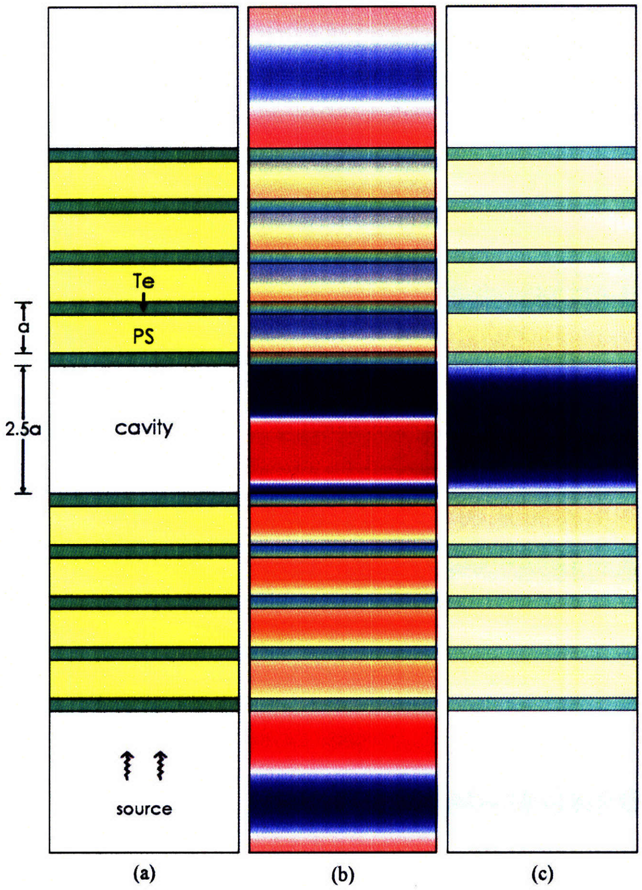

Figure 3-4: Conversion of light from the optical pumping frequency ($\omega = 0.4(2\pi c/a)$) to the stimulated emission frequency ($\omega = 0.2(2\pi c/a)$) in a Fabry-Perot cavity, illustrated in (a). The pump pulse is shown in (b) and the stimulated emission is shown in (c). Green represents high dielectric tellurium, yellow representing lower dielectric polystyrene; blue and red signify positive and negative electric fields, respectively.

Also, the parameter values $\sigma_2 = 0.0008$ and $I_2 = 2.77$ (at the edge of the material near the source) lead to a population transfer of about 69%; furthermore, $\sigma_1 = 0.001$, which is large enough to create sustainable radiative transfer, and τ_{21} is set to an extremely large time, which makes non-radiative decay negligible ($\Gamma_e = \Gamma_1$) and leads to an extremely high conversion efficiency $\eta = 0.9986$. Evidence for this process is given by Fig. 3-5, which shows intensity as a function of position and frequency. The upper band, centered around $\omega = 0.4(2\pi c/a)$, corresponds to the optical pump frequency, which clearly is transmitted through the dielectric structure with relatively low reflection. The lower band, centered around $\omega = 0.2(2\pi c/a)$, which only exists in the middle of the active cavity, represents the electronic coupling to the fundamental mode of the cavity. In the absence of this electronic coupling, no such band occurs, as shown on the right-hand side of Fig. 3-5. In general, multimode lasing could occur in an active material, but all of the calculations in this chapter are designed to have non-degenerate resonant modes with a mode spacing significantly greater than the width of the population-inverted atomic transition. The field patterns associated with optical pumping and stimulated emission are shown in Fig. 3-4.

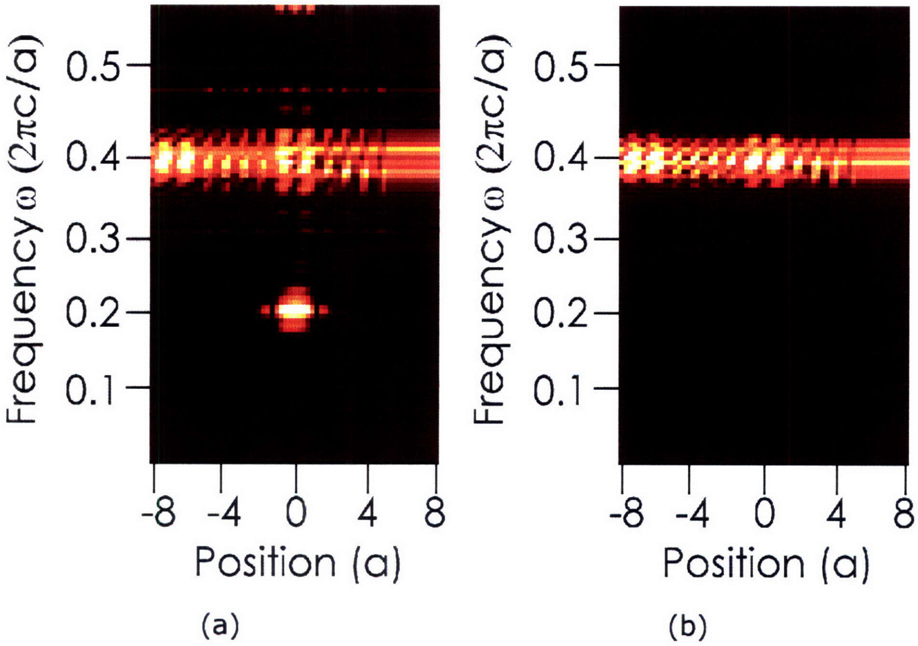

Figure 3-5: Visualization of $E(x, \omega)$ in 1D Fabry-Perot cavities (a) with active material and (b) without active material. The low-frequency band in (a) demonstrates that active materials can induce frequency conversion.

3.3.4 Dielectric rods in a 2D lattice

The next simulation is of a 2D system, a square lattice of dielectric rods possessing a line of defect rods. The parameters used were based on those of Ref. [1], with $\epsilon = 8.9$ and $r = 0.2a$ for the normal rods, and $\epsilon = 17.1$ and $r = 0.25a$ for the defect rods. The purely dielectric system, illustrated in Fig. 3-6, was tested, and was shown to yield a transmission peak about a frequency of $\omega = 0.346(2\pi c/a)$, as shown in Fig. 3-7. Introduction of active material in the dielectric rods having an

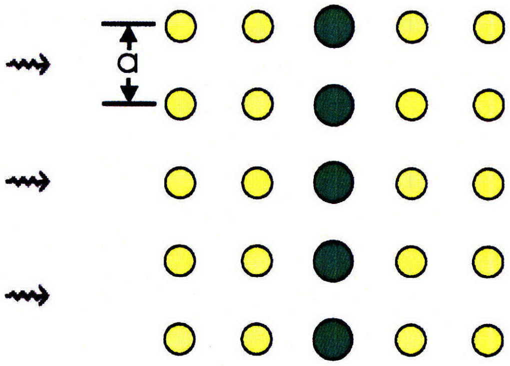

Figure 3-6: Square lattice of dielectric columns, with $r = 0.2a$ and $\epsilon = 8.9$. A row of defect columns in the middle have an $r = 0.25a$, $\epsilon = 17.1$.

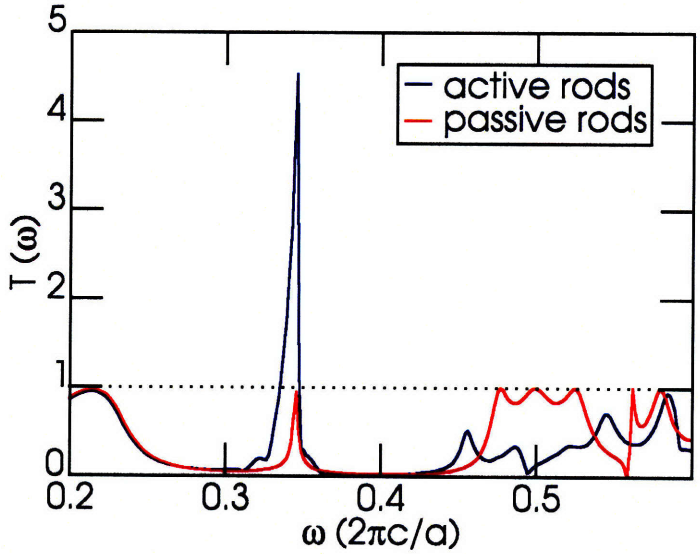

Figure 3-7: Transmission for active and passive versions of the geometry shown in Fig. 3-6. Notice the sharp enhancement of the defect mode peak in the gap to above 100%, the signature of a gain medium.

absorption frequency $\omega = 0.5(2\pi c/a)$ and width $\Gamma = 0.01(2\pi c/a)$, along with an emission frequency $\omega = 0.346(2\pi c/a)$ and width $\Gamma = 0.0006(2\pi c/a)$, changed the transmission spectrum as one would expect – the frequencies around $\omega = 0.5(2\pi c/a)$ being depleted and the frequencies around the defect mode at $\omega = 0.346(2\pi c/a)$ being strongly enhanced. In fact, the transmission percentage for the defect mode goes above 100%, the signature of a gain medium. The comparison between the two

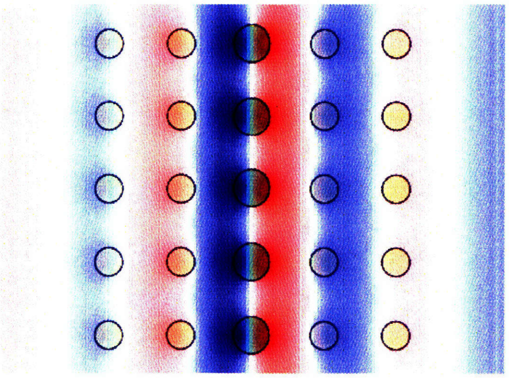

Figure 3-8: Snapshot of the "π-like" defect mode centered about $\omega = 0.346(2\pi c/a)$.

cases is shown in Fig. 3-7. The parameter values $\sigma_2 = 0.2$ and $I_2 = 0.01979$ (on the right edge of the central defect rod) lead to a population transfer of about 40%; also, $\sigma_1 = 0.2$, which is large enough to create sustainable radiative transfer, and τ_{21} is set to an extremely large time, which makes non-radiative decay negligible ($\Gamma_e = \Gamma_1$). As a result, the efficiency of the conversion is given by $\eta = 0.986$ for the parameter values used. An illustration of the defect mode is given in Fig. 3-8. The main defect mode, centered about $\omega = 0.346(2\pi c/a)$, evidently has one nodal line, said to be "π-like" [1]. Interestingly enough, one might expect this mode to couple poorly to the atoms on the defect rods due to the nodal plane, but a substantial transmission enhancement of over 300% is observed.

3.3.5 Cylindrical photonic crystal in 3D

The third simulation is of a cylindrical photonic crystal, a multilayer dielectric structure that is rolled into a cylinder, with a cross-section such as the one in Fig. 3-9. In this chapter, an external plane-wave source on the left side of the structure is used to excite an atomic material inside the otherwise hollow core. The targeted mode is the so-called TM_{01} mode, which has a non-zero E_z and H_ϕ. Further properties of the modes of cylindrical photonic crystals are discussed in Ref. [19].

Another direct illustration of optically pumped lasing is shown in Figs. 3-10 and 3-11. Here, a cylindrical photonic crystal with two bilayers of tellurium and polystyrene

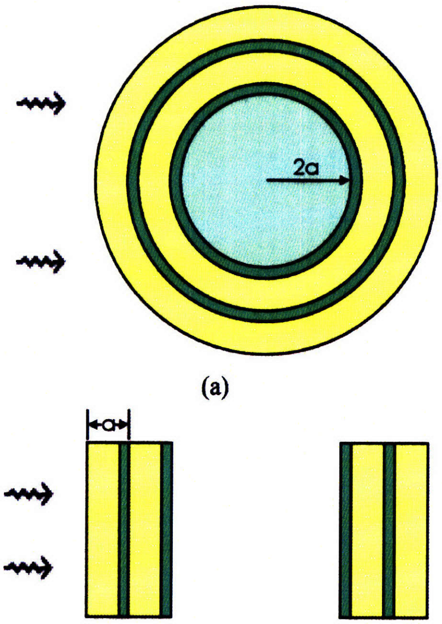

(a)

(b)

Figure 3-9: Two slices of a cylindrical photonic crystal, a multilayer dielectric structure with continuous symmetry along z. Here, a core of radius $2a$ is surrounded by two bilayers of dielectric, with $\epsilon_{\text{low}} = 2.56$ and $\epsilon_{\text{high}} = 23.04$. Subfigure (a) depicts a cross-section perpendicular to the z-axis, and subfigure (b) shows a cross-section through the center of the core along the z-axis.

and an inner radius $r_i = 2a$ is pumped with a broad Gaussian source centered around $\omega = 0.4(2\pi c/a)$. The short cylinder of active material in the center absorbs the incoming radiation with $\omega = 0.4(2\pi c/a)$ and $\Gamma = 0.002(2\pi c/a)$), then re-emits near the predicted TM_{01} cutoff frequency $\omega = 0.1914(2\pi c/a)$ (for $r_i = 2a$), with width $\Gamma = 0.0004(2\pi c/a)$.

That this conversion takes place can be checked visually: it is evident from the before and after snapshots in Fig. 3-11 that the wavenumber decreases substantially in the horizontal direction. Combining that observation with the rest of the information about this mode implies that the latter snapshot corresponds to a much lower frequency mode.

This expectation can also be checked numerically. In Fig. 3-12, transmission through the photonic crystal is shown for two cases: one with active material and one without. Clearly an enormous enhancement of the transmission, orders of magnitude above 100%, occurs with the introduction of the active material. This can only be due to optical pumping. A smaller but still noticeable drop in the transmission of some of the energy near $\omega = 0.4(2\pi c/a)$ lends support to this conclusion. The peak in transmission occurs at $\omega = 0.188(2\pi c/a)$, fairly close to the expected peak frequency $\omega = 0.1914(2\pi c/a)$. The shift in the resonant frequency in the presence of the active material can be attributed to the so-called pulling effect. The real part of the gain polarization corresponds to a small shift in the dielectric constant, which in turn shifts the resonance. The strength of the pulling effect is thus proportional to the coefficient converting electric field into polarization, which is on the order of $\xi = \sigma_i/(\omega_i \Gamma_i)$. The reason that the pulling effect was not observed previously is that $\xi = 5$ in the 1D case, and $\xi = 964$ in the 2D case, in both cases giving rise to shifts which fall below the frequency spacing. However, $\xi = 6531$ in this 3D calculation, giving rise to a substantially larger shift which in turn gives rise to fairly off-resonance coupling, broadening the emission substantially beyond the natural width, and lowering the efficiency. The parameter values $\sigma_2 = 0.05$ and $I_2 = 0.0117$ (on the right side of the inner cavity, $r = 1.25a$) lead to a population transfer of about 36%; also, $\sigma_1 = 0.5$, which is large enough to create sustainable radiative transfer, and τ_{21} is set to an extremely large time, which makes non-radiative decay negligible ($\Gamma_e = \Gamma_1$). In the end, the efficiency of this conversion process is $\eta = 0.828$. Tuning the emission frequencies to the shifted values and adjusting the widths accordingly would allow the efficiency to approach the theoretical maximum. Furthermore, note that the shift in the effective index of the core material may alter the Fabry-Perot resonances and thus shift the position of the transmission peaks observed in Fig. 3-12. However, it is also possible that numerical errors that occur during the propagation of the fields by the atomic code may have given rise to some of the differences between the active and passive core transmission spectra, especially away from the resonant frequencies of $\omega_1 = 0.1914(2\pi c/a)$ and $\omega_2 = 0.4(2\pi c/a)$. This points to the possibility that a prediction-correction approach to the field propagation, as discussed, e.g., in Refs. [62, 74], may be warranted for regimes of stronger polarizabilities ξ.

Finally, consider the case of a small cluster of atoms placed at the exact center of

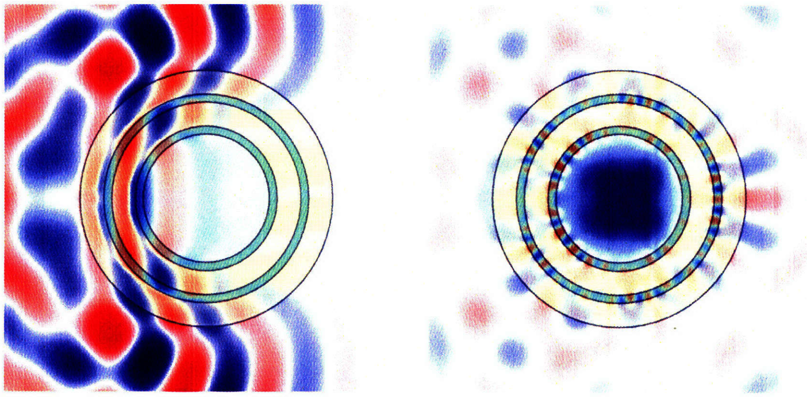

Figure 3-10: Conversion of light at an optical pump frequency into a stimulated emission frequency via the TM_{01} resonant mode of a cylindrical photonic crystal with 2 bilayers, viewed perpendicular to the z-axis. The incoming wave in (a) has $\omega \approx 0.4(2\pi c/a)$, and the outgoing wave in (b) has $\omega \approx 0.19(2\pi c/a)$.

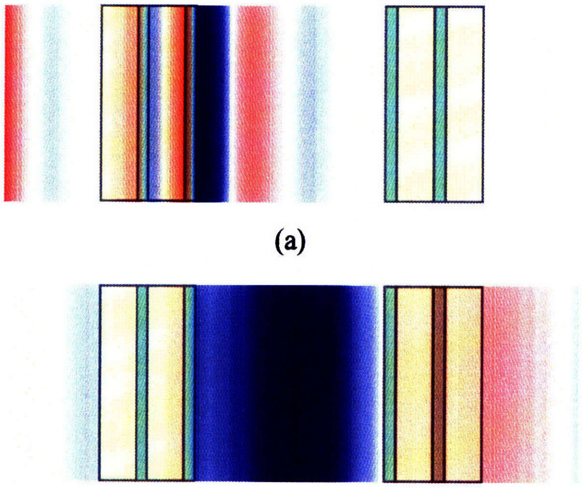

Figure 3-11: Conversion of light at an optical pump frequency into a stimulated emission frequency, as in Fig. 3-10, but in a cross-section through the center of the core along the z-axis.

the cylindrical photonic crystal. The cluster radius is taken to be much smaller than an optical wavelength so the atomic system can be modeled as a single point in space on the scale of the simulation. This system is studied by comparing the calculation for an empty cylindrical core to one which has an atomic cluster inside. In this calculation, the excitation frequency is $\omega = 0.2857(2\pi c/a)$, with width $\Gamma = 0.01(2\pi c/a)$; the

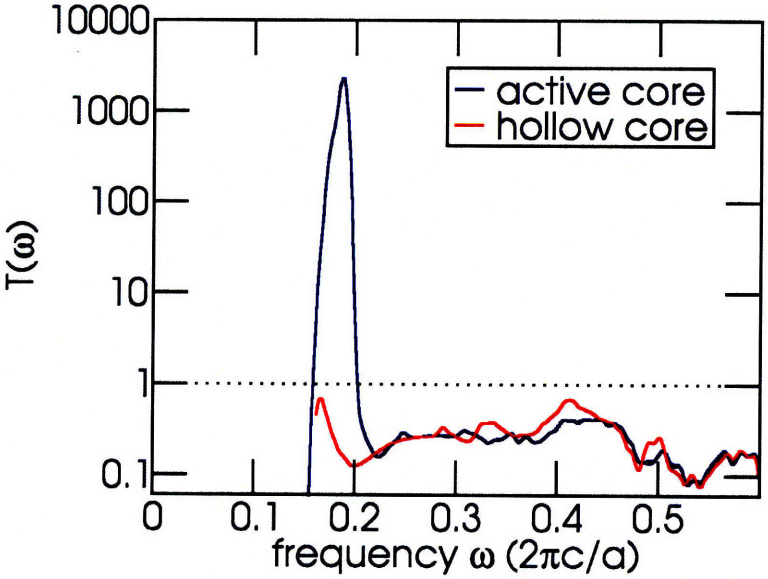

Figure 3-12: Transmission for a cylindrical photonic crystal structure with and without active material at the core. Notice the slight decrease in transmission at $\omega \approx 0.4(2\pi c/a)$ and the sharp increase in transmission about $\omega \approx 0.186(2\pi c/a)$ for the active material.

emission frequency is $\omega = 0.1939(2\pi c/a)$, with width $\Gamma = 0.0002(2\pi c/a)$. The cluster is optically pumped by an extremely broad Gaussian source with central frequency $\omega = 0.264(2\pi c/a)$. This arrangement allows for depopulation of the ground state of the central cluster followed by emission into a TM_{01} mode of non-negligible magnitude. The differential field profile after excitation followed by stimulated emission is shown in Fig. 3-13. As expected, the TM_{01} mode is the one observed. The conversion efficiency of this process was found to be extremely high ($\eta > 0.999$). This suggests that the scheme for biological sensing proposed in chapter 2 would be capable of detecting a tiny cluster of atoms. If one were to move it away from the center, coupling to the same mode would still be expected (except at the nodes). The final amplitude of the fluorescent mode for atomic clusters on or off center should be the same in the absence of other processes besides stimulated emission (neglecting modal decay). However, the threshold may be increased due to the decrease in the local density of states (which goes as the zeroth order Bessel function squared for this problem).

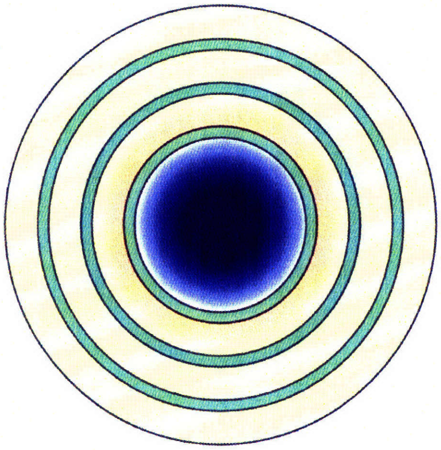

Figure 3-13: Snapshot of the TM_{01} mode which is excited by a small cluster of atoms at the center of the cylindrical photonic crystal.

3.4 Conclusion

An extension to the well-established FDTD method for simulating Maxwell's equations in macroscopic dielectric media has been developed to include active materials modeled by four-level atoms. The code was verified to display the saturation and threshold effects expected for atomic materials, in agreement with analytical results. This method is used to simulate optically pumped lasers in one, two and three dimensions, as well as the biological sensor design proposed in chapter 2 . It is found that the key criteria for efficient conversion of energy are the delivery of the right amount of field energy to create a population inversion of order unity, as predicted by equation (3.7), and the presence of a small amount of energy at the resonant emission frequency, along with a low enough loss rate Γ_e and a high enough coupling σ_1, such that the induced population inversion $|\Delta N_1(0)| > \omega_1 \Gamma_e / 4\pi\sigma_1$. One additional measure that can increase the efficiency is concentrating atomic emitters in the regions of the defect that should have the highest field intensity in the defect mode. Simulations of the cylindrical photonic crystal system support this assertion, which is why the radius of the active material was set to be only $1.4a$ in a cylindrical photonic crystal with $r_i = 2a$, and is also the reason why the active material is chosen to only fill the middle half of the cavity in a 1D Fabry-Perot etalon defect cavity of size $2.5a$. Finally, careful choice of coupling strengths and linewidths is critical for efficient conversion; any real world system would have very fixed values of these parameters which could put an important limitation on conversion efficiency. These simulations should facilitate the design of ultra-low threshold lasers and single fluorescent molecule detectors. Future work should incorporate changes in the rate of spontaneous emission associated with presence of a cavity and allow for accurate calculation of the lasing threshold.

Chapter 4

Improving solar cell efficiencies with photonic crystals

4.1 Introduction

One of the foremost challenges in designing silicon photovoltaic cells is devising an efficient light-trapping scheme. Crystalline silicon (c-Si) and nanocrystalline silicon (nc-Si) have an indirect bandgap, which gives rise to weak absorption of light in the near infrared (near-IR), with an absorption length that increases from over 10 μm for λ =800 nm to over 1 mm for λ =1108 nm [75]. However, that range of wavelengths contains 36.2% of solar photons with energies above the bandgap of c-Si [76]. Thus, a c-Si solar cell with a plain wafer geometry substantially less than 1 mm thick (e.g., 100 μm) will fail to absorb a significant number of photons that could otherwise be used to generate power in the cell. At the same time, the expense of c-Si for a 300 μm-thick wafer with a correspondingly long diffusion length drives up costs and limits potential supply significantly. As a result, efficient light trapping schemes that can achieve high levels of absorption for thin films of silicon are needed. In this chapter, two distinctive approaches to light-trapping are discussed: geometrical and wave optics. The wave optics approach can be implemented using either gratings or photonic crystals.

The vast majority of light-trapping schemes used in solar cells today are based

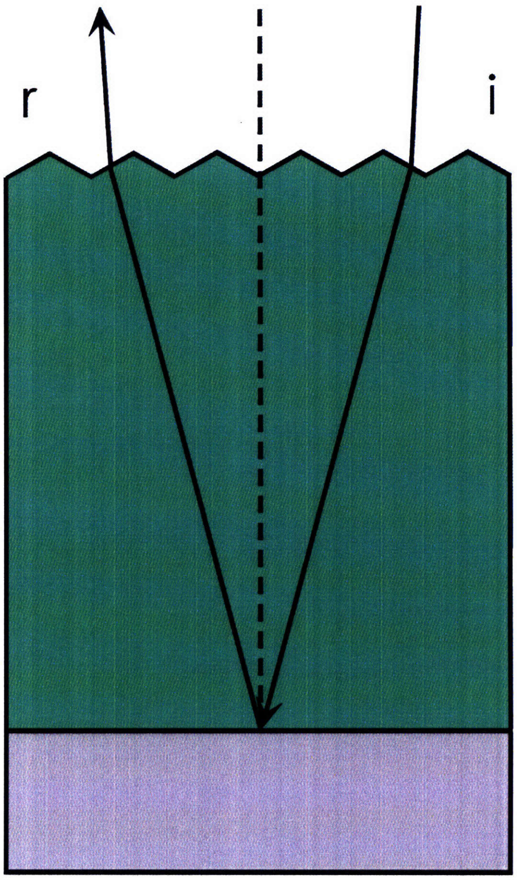

Figure 4-1: Illustration of conventional solar cell light trapping. Note that the front-surface texturing increases the effective path length via refraction into an oblique angle.

on geometrical optics. This approach, illustrated in Fig. 4-1, consists of two key elements. The first element of the design is a metallic back reflector, which ensures that incoming light takes two passes through the cell. In the second element of the design, front-surface texturing is used to further increase the average path length of the light, through refraction into oblique angles. In the ideal case, texturing of this type will yield a Lambertian surface, which randomly scatters light into a uniform distribution of forward angles. Combining perfect random scattering with a lossless reflector in the back theoretically enhances the effective path length by a factor of $4n^2$, corresponding to a value of about 50 for c-Si, and 30 for TiO_2 [77]. If one patterns the front surface of c-Si with an inverted pyramid structure, for example by etching (100)-oriented c-Si wafers with KOH to form (111)-oriented pyramids, normally incident light will now be refracted into large angles inside the c-Si. For the best type of random distribution of pyramids, the predicted performance comes close to the ideal Lambertian scattering case [78]. However, no actual scattering surface is perfectly Lambertian in nature – the extent to which it replicates the ideal is typically called the "Lambertian fraction" Λ, and is typically 55% or less [79]. Furthermore, it has been found that the fill factor (a measure of efficiency) is generally decreased by surface texturing [80, 81]. In one case, the fill factor falls from 75% to 70%, for a relative drop of 6.7% [81]: this can potentially erase most of the gains associated with improved light trapping.

The light-trapping approach illustrated in this chapter uses wave optics, which has been shown to be capable, in principle, of outperforming all geometrical optics approaches for a certain range of wavelengths [82, 83]. This is because, in contrast to geometric optics approaches (such as the ones discussed above) that treat all wavelengths of light equally, wave optics approaches can be targeted to enhance absorption only in the range where it can be most beneficial. To date, there has been some work considering wave optics approaches to light-trapping. Some groups have used gratings to enhance the effective path length via diffraction [84, 85, 86, 87, 88, 89, 90]. However, approaches using metal gratings, while increasing absorption, have not been shown to increase power generation efficiency [87]. On the other hand, dielectric gratings have shown promising results in the direction of efficiency improvements [89, 90]. In order to move further away from usage of metal back-reflectors, some recent work has combined a distributed Bragg reflector (DBR) with a grating [91, 92].

In this chapter, three approaches to light trapping based on full-wave optics are examined: metallic gratings, dielectric gratings, and photonic crystals. Photonic crystals are the ideal choice because they offer complete control over the propagation of light. One of the key concepts associated with a photonic crystal is the so-called photonic band gap, a range of wavelengths which are reflected for any incident angle and polarization. Closely associated with the photonic band gap is the phenomenon of slow light. One can understand both phenomena by the following: in a periodic medium, waves must oscillate in a specific form, dictated by Bloch's theorem. When the energy of the medium oscillates with the same period as the lattice, the waves can concentrate their energy in the low-energy region or in the high-energy region, which gives rise to two different energies for the same spatial period. The energies in between those two limits form the bandgap, a range of energies that cannot propagate in the bulk. As a result, photons with the forbidden energies that enter the photonic material are reflected. The reason why slow light also occurs in these systems is that the photonic bandgap induces an anti-crossing that flattens the photonic bands, giving rise to slow group velocities.

There are three ways in which photonic crystals can improve light-trapping efficiency. First, they can be designed to reflect a range of wavelengths with arbitrarily low losses for all incident angles and polarizations [1]. Second, they can be designed to diffract incoming beams into highly oblique angles. This diffraction takes advantage of the increased density of states associated with a high-index medium. With the proper choice of periodicity, this effect can be targeted to the key near-IR region of the solar spectrum. Third, the photon density of states inside the photonic crystal can be selectively enhanced in order to improve absorption efficiency [82]. These modes can be coupled to from outside the photonic crystal via superprism-type effects [93]. All of these effects can be thought of as increasing the effective path length of photons in the near-IR, which increases the dwell time and increases the probability of absorption. Note that these approaches are especially advantageous for thin cells 40 μm or less in thickness, which are not amendable to coarse texturing approaches that introduce features 5-10 μm in depth. The features discussed in this chapter can work for even very thin cells of only a few microns. Thin cells offer the advantage of lower materials usage as well as lower bulk recombination losses and potentially higher open-circuit voltages [94].

4.2 Numerical methods

The light-trapping properties of the structures discussed in this chapter were studied using a transfer matrix method known as the S-matrix method [95]. The structure is broken up into slices with uniform symmetry in the z-direction, boundary conditions are imposed at one end, and fields are propagated throughout the structure. Light trapping is calculated by modeling the c-Si regions with a complex dielectric constant that depends on wavelength, as in Ref. [75]. The c-Si region is treated as if it were only intrinsic, i.e., the doping of the $p-$ and $n-$doped regions can be considered to have a negligible impact on the optical properties of the device. Aside from that issue, in principle, this calculation of the optical properties is exact apart from discretization errors, which can be reduced systematically by increasing the resolution of the structure. Verification was performed for several simulations using the finite-difference time domain method [47] with perfectly-matched boundary layers [96]. In general, the results were in good agreement, but the FDTD method was much slower for the same resolution, so it was not used for most calculations.

In order to calculate power generation efficiency from this model, it is assumed that each absorbed photon with energy greater than the bandgap energy generates an electron-hole pair, and both carriers reach the electrical contacts. This corresponds to the statement that the diffusion length L_D is much greater than the distance traveled by each carrier (i.e., $L_D \gg d$). Power generation efficiency is given by $\eta = J\left[V(\max)\right]V(\max)/P_{inc} = (J_{sc}V_{oc}/P_{inc}) \times FF$, where P_{inc} is the solar irradiance, $V(\max)$ and $J\left[V(\max)\right]$ are the voltage and current density at the maximum power point, respectively, the product of which equals the open-circuit voltage V_{oc} times the short-circuit current density J_{sc} times the fill factor FF. Following Refs. [97, 98], the above quantities can be calculated as follows: first, the current density J as a function of the voltage V is given by the sum of the photon-induced current minus the intrinsic current generated by radiative recombination, i.e.

$$J(V) = \int_0^\infty d\lambda \left[\frac{e\lambda}{hc}\frac{dI}{d\lambda}A(\lambda)\right] - \frac{e(n^2+1)E_g^2 kT}{4\pi^2\hbar^3c^2} \exp\left(\frac{eV-E_g}{kT}\right), \tag{4.1}$$

where $\frac{dI}{d\lambda}$ represents the light intensity experienced by the solar cell per unit wavelength (given by the ASTM AM1.5 solar spectrum [76]), $A(\lambda)$ is the absorption calculated above, E_g is the bandgap energy, kT is the thermal energy at the operating temperature T, n is the average refractive index of the semiconductor, and the

$n^2 + 1$ prefactor is derived by assuming an absorbing semiconductor substrate (as in Ref. [98]). Next, the open circuit voltage is calculated by setting $J = 0$. Finally, the fill factor is found by setting the derivative $d(JV)/dV = 0$ and solving for $V(\max)$ and $J\left[V(\max)\right]$.

In order to understand the basic properties of the photonic crystal lattices used in this chapter, the eigenmodes of Maxwell's equations with periodic boundary conditions, also known as a photonic bandstructure, were computed by preconditioned conjugate-gradient minimization of the block Rayleigh quotient in a planewave basis, using a freely available software package [99].

4.3 Results and discussion

4.3.1 Metallic designs

Consider the performance of several metal-based c-Si solar cells which all have a thickness $d = 2\,\mu\text{m}$, with light incident normally from above the cell, and electric field polarization in the plane. The first solar cell design consists of an anti-reflection coating made of silicon nitride ($n \approx 1.91$) on top of a slab of c-Si (placed on top of a c-Si substrate). Its power generation efficiency η is calculated to be 9.07%. The second design, shown in Fig. 4-2(a), uses an anti-reflection coating plus a perfect metallic reflector to force light to pass twice through the material. The spectrally reflected mode is denoted by r. This design leads to a greatly improved efficiency of 13.77%. The third design, shown in Fig. 4-2(b), uses a perfect metallic reflector with a grating optimized for light trapping. Spectrally reflected modes are denoted by r_0, while diffracted modes are denoted by r_1, r_2, etc.

In order to understand how to optimize a grating, it is necessary to consider its underlying physics. The absorption spectrum for generic 1D and 2D gratings are depicted in Fig. 4-3, and compared to the spectrum for the systems relying on simple spectral reflection. One can construct a simple analytical model to explain the diffractive light-trapping mechanism. If a bulk region of thickness d is considered,

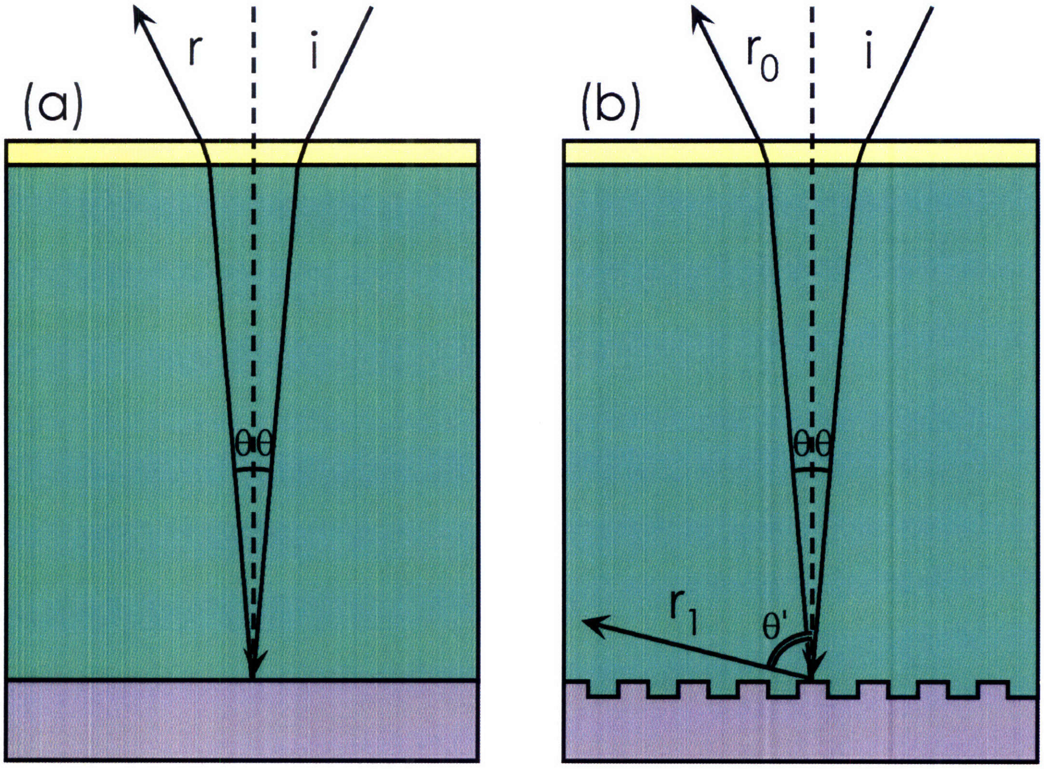

Figure 4-2: Illustration of two metallic solar cell designs: (a) a simple design with a perfect metal backing, which displays only spectral reflection; (b) a metal with a periodic grating on the back. Crystalline silicon is in green, metal in grey, and air is transparent.

then all resonances should pick up a round-trip phase change which is a multiple of 2π, which yields the condition $k_{\perp} = \pi m/d$, where m is an integer, and the frequency of the diffracted mode is given by $\omega = (c/n)[G^2 + (\pi m/d)^2]^{1/2}$. If the only source of loss is the material, then the quality factor is given by $Q = n/2k$. Near the diffraction limit, this model predicts that the mode spacing is given by $\delta\omega_{m+1} = c\pi^2(2m+1)/(2nGd^2)$. This corresponds to a linear increase with the mode number, which means that peaks will have increasingly large spacing. This in turn implies that the most benefit from diffraction will occur right near the diffraction limit. Comparison between this simple analytical model for the mode spacings and quality factors with the results in Fig. 4-3 shows excellent agreement. Note that one could alternatively have used a second order diffraction grating instead, as in Ref. [88]. However, it was found that the performance of the second order gratings is similar to first order gratings for the periods examined in this chapter.

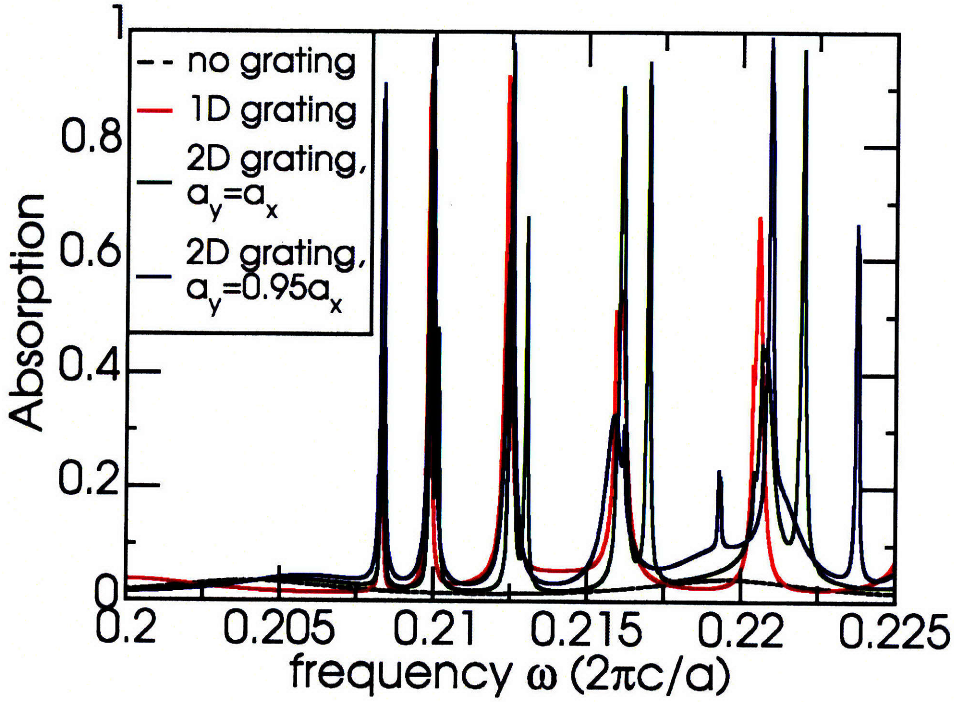

Figure 4-3: Absorption versus frequency of a 2 μm-thick layer of c-Si, with several different metal reflectors on bottom: one which is planar, one with 1D etching, and two with 2D "checkerboard" etching patterns and slightly different ratios of the x- and y-periods. All gratings have a square etch with a fill factor of one-half in each direction.

In grating optimization, the first parameter that must be determined is the period of the grating p. Following previous work (e.g., Refs. [85, 86, 87]), it is chosen so that first order diffraction will occur in the near-IR. Through optimization, its value is determined to be 255 nm, which leads to diffraction of wavelengths of 920 nm and below in c-Si. In either case, the exact optimal periodicity will depend slightly on the thickness of the active region, and will be shifted to longer wavelengths for thicker cells (since they will already be absorbing shorter wavelengths well). Furthermore, there are a variety of other parameters to be considered, such as profile shape, incident angle and polarization, profile, duty cycle, and etch depth [100]. The rectangular (square-wave) profile is chosen because it is a simple structure that has been shown to perform better than a symmetric triangular pattern [89]. The etching profile is

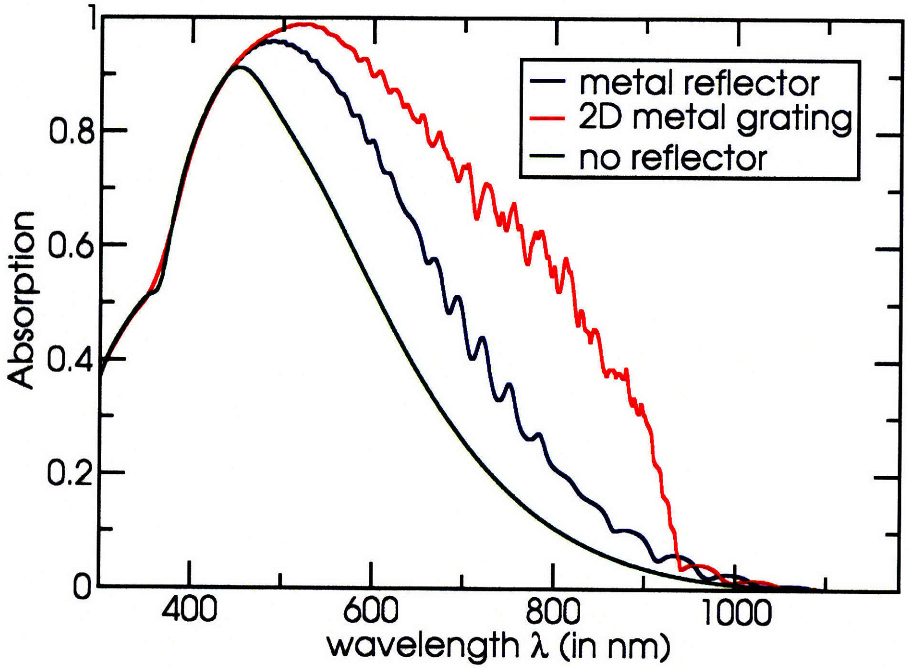

Figure 4-4: Absorption vs. wavelength for three 2 μm-thick Si cell designs: no back reflector, perfect metal back reflector, and perfect metal grating with 2D periodicity.

chosen to be a symmetric square wave, for simplicity. The duty cycle f, i.e., the fraction of dielectric that is raised over each period, is chosen to be exactly one-half for the reason that the largest Fourier components (responsible for coupling to diffraction) will occur at that value. Finally, in choosing the etch depth, one has to consider at least two interference effects: one is between light bouncing off the top of the etch pattern versus the bottom of the etch pattern, which gives rise to a phase difference of $\delta\phi = 2k_{\text{hi}}t$, and one between light passing through the top of the etch pattern and light passing through the bottom of the etch pattern, which gives rise to a phase difference of $\delta\phi = 2(k_{\text{hi}} - k_{\text{lo}})t$; these lead to two different predictions for the etch depth. It is found that the best etch depth is 67 nm. In the ideal case of no absorption from reflection or surface plasmons, the following remarkable results are obtained: for a 1D periodic grating, the efficiency is found to be 17.86%; for a 2D periodic "checkerboard" grating (where the periods are equal in each direction), the efficiency is given by 18.69% (efficiency are quoted to four significant figures for comparison purposes). The corresponding absorption spectra are shown in Fig. 4-4. However, it is well-known that there are two sources of loss in a real metallic grating – first, the natural absorption of the metal upon reflection, as well as surface plasmons. These losses are too great to allow increased power generation efficiency in an actual device. That consideration has driven recent interest in all-dielectric structures.

4.3.2 Dielectric designs

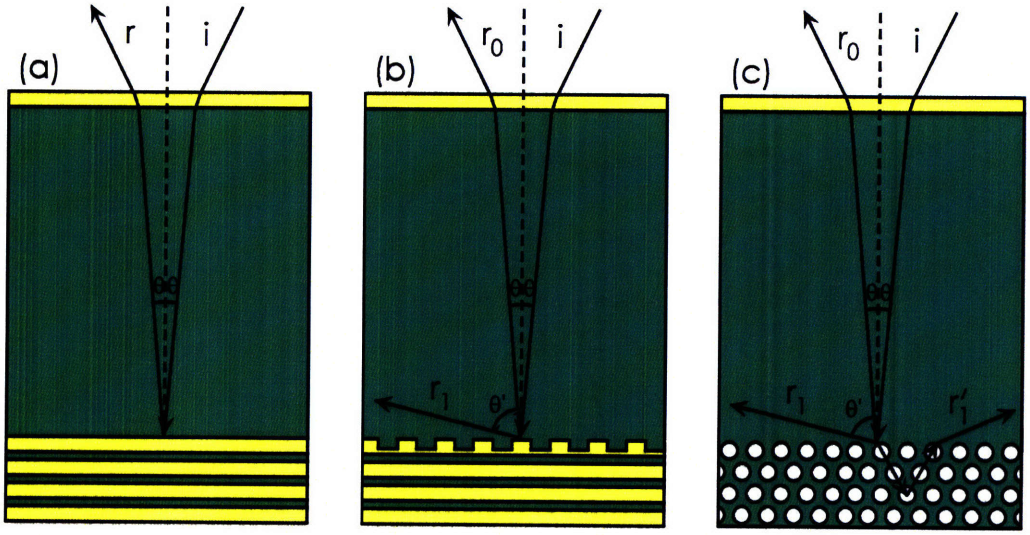

Figure 4-5: Illustration of three solar cell designs: (a) a simple design with a distributed Bragg reflector (DBR), which displays only spectral reflection; (b) a DBR plus a periodically etched grating, displaying spectral reflection and diffraction; and (c) a photonic crystal consisting of a triangular lattice of air holes, displaying simultaneous reflection and diffraction from the photonic crystal layer. The crystalline silicon is in green, and the low dielectric is in yellow; the air is transparent.

DBR-based designs

Now consider the performance of three dielectric-based solar cell structures made of 2 μm of c-Si. The first design, shown in Fig. 4-5(a), consists of an anti-reflection coating on top and a distributed Bragg reflector (DBR) in the bottom. In creating a DBR design that reflects strongly in the near-IR, the materials are chosen to be c-Si ($n \approx 3.5$) and SiO_2 ($n = 1.5$) because they represent a low cost and readily available method of making an omnidirectional reflector [101]. Given the target wavelength range and materials, a period $a = 150$ nm is chosen. Using 10 bilayers of c-Si and SiO_2 yields high reflectivity (over 99%) over most of the critical wavelengths that are difficult to absorb in silicon. The overall efficiency is found to be 12.44%, which compares reasonably well to the perfect metal reflector efficiency of 13.77%, and may be larger in practice due to the much greater losses of a realistic metallic reflector.

The second dielectric design, shown in Fig. 4-5(b), based on the one studied in Refs. [91, 92] consists of an anti-reflection coating, a DBR on the bottom, and a periodic grating in the back of the top low-index SiO_2 layer of the DBR. It should be noted that the introduction of the grating into the omnidirectional reflector can, in principle, cause coupling into propagating modes in the reflector, thus eliminating perfect omnidirectional reflectivity.

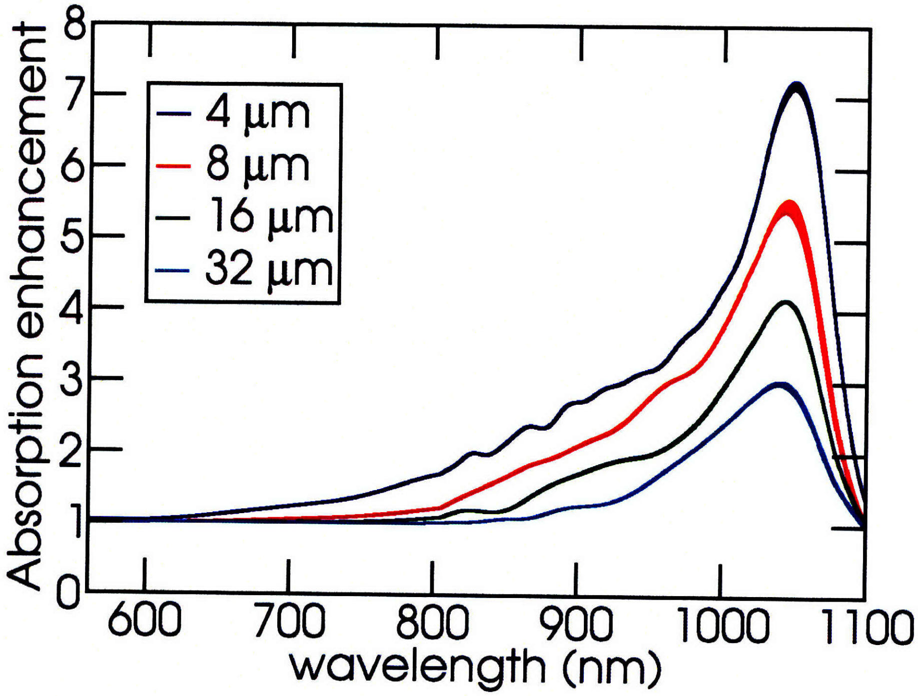

Figure 4-6: Illustration of the average enhancement created by a 1D grating with period $1.375a$ and etch depth $0.46a$, for c-Si wafers with thicknesses ranging from 4 μm up to 32 μm.

The results for c-Si wafers with thicknesses varying from 4 μm to 32 μm, and

# bilayers	efficiency η (%)
1	12.48
2	14.60
3	15.25
4	15.41
5	15.45
6	15.46
7	15.47
8	15.47

Table 4.1: Efficiency of the solar cell design in Fig. 4-5(b) (with a 1D periodic etch) as a function of the number of DBR bilayers.

backed with a DBR etched with a 1D grating with period $1.375a$ and etch depth $0.46a$ are shown in Fig. 4-6 (after smoothing over individual closely-spaced peaks as depicted in Fig. 4-3). In analyzing these results, it is observed that the overall absorption goes up with thickness, as expected, due to the greater number of modes supported by the bulk semiconductor region. However, the relative enhancement of light trapping is greater for thinner films, because they have lower baseline absorption. For a 4 μm-thick c-Si region, the greatest absorption enhancement of about a factor of 7 occurs over the wavelength range 1040 to 1060 nm. This result is consistent with the observation that the density of peaks is greatest near the diffraction limit, as illustrated in Fig. 4-3.

However, when I optimize the parameters for a 2 μm-thick sample of c-Si, I find that the parameters are similar to what was seen before for a metallic structure of equal thickness, specifically, a DBR period $a = 160$ nm, an etching period of 255 nm, and etch depth of 60 nm. The efficiency as a function of the number of bilayers is given in table 4.1.

Photonic crystal-based designs

The third design, illustrated in Fig. 4-5(c), consists of an anti-reflection coating in the front, and a photonic crystal in the back, made of a four-layer-deep 2D triangular lattice of air holes, with an air-hole radius of $r = 0.375a$. Aside from the diffracted modes, which are labeled in the same fashion as those in the grating, additional modes which penetrate into the photonic crystal before reflection or loss out the backside are denoted along the path r'_1. Thus, this design effectively has more silicon that can be used for absorption (since it is not surrounded by an insulator). On an experimental note, electron-hole recombination could be prevented through oxidation of the air-silicon interfaces, which would create a thin layer of silica for passivation. It would also be possible to use hydrogen gas for passivation, or to fill the holes entirely with a passivating material.

In order to understand the general properties of photonic crystal lattices placed in solar cells, I shall first consider the properties of a simple square lattice of air holes: first, calculating the bandstructure, then calculating the detailed absorption spectrum. The bandstructure of the TE modes of the photonic crystal used in this problem is shown in Fig. 4-7. Around $\omega = 0.225$, a flat band is observed, which implies slow light propagation and enhanced absorption.

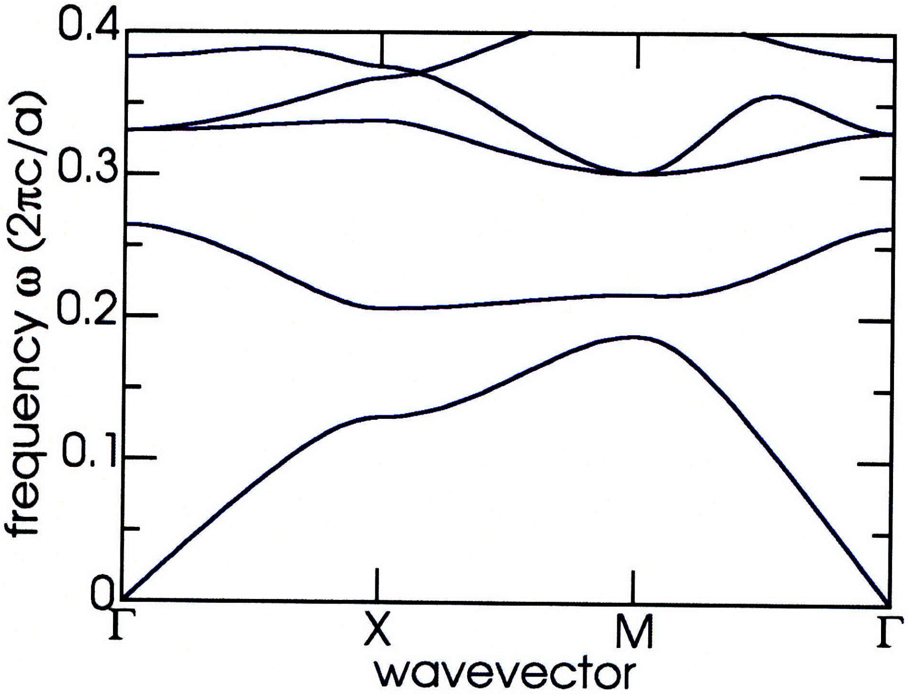

Figure 4-7: Bandstructure for tranverse electric (TE) modes in a photonic crystal consisting of an infinite 2D square lattice of air holes in c-Si with period 1.375a and radius $r = 0.55a$.

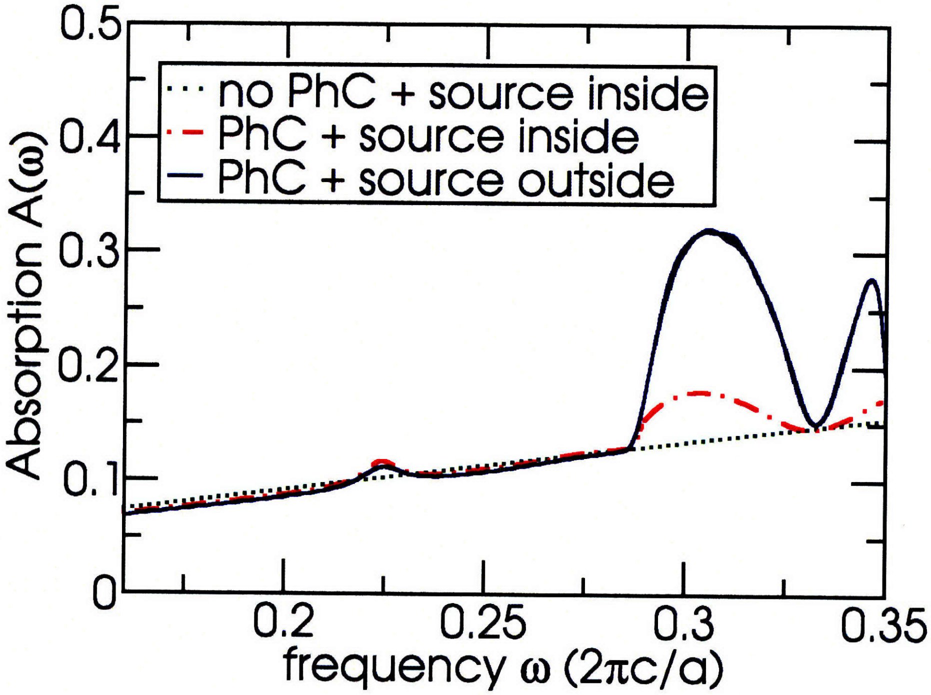

Figure 4-8: Absorption versus frequency at normal incidence for a photonic crystal consisting of 3 layers of a 2D lattice of air holes with $r = 0.55a$ and period $1.375a$.

An absorption spectrum is calculated for three geometries: a source inside the c-Si with no photonic crystal, a source inside the c-Si with a photonic crystal consisting of a 2D lattice of air holes, and a source outside the c-Si with the same photonic crystal. Fig. 4-8 is for normal incidence, and Fig. 4-9 is for TE modes at oblique incidence. Note that a large enhancement is observed at the diffraction limit $\omega = 0.288(2\pi c/a)$, as would be expected for the results obtained with the grating geometry. Furthermore, some narrow peaks in the absorption are observed, which correspond to resonant photonic crystal modes (superprism-type effects) – for example, at normal incidence, one peak is observed around $\omega = 0.225(2\pi c/a)$ in Fig. 4-8, as predicted by the bandstructure in Fig. 4-7. More peaks are observed at oblique incidence around $\omega = 0.18(2\pi c/a)$, $0.245(2\pi c/a)$, and $0.255(2\pi c/a)$ in Fig. 4-9, which correspond to frequencies at which coupling takes place to photonic crystal modes, as can be seen from Fig. 4-7. The greater number of peaks observed at oblique incidence can be explained by the fact that coupling to certain modes is forbidden in directions of high symmetry, such as normal incidence.

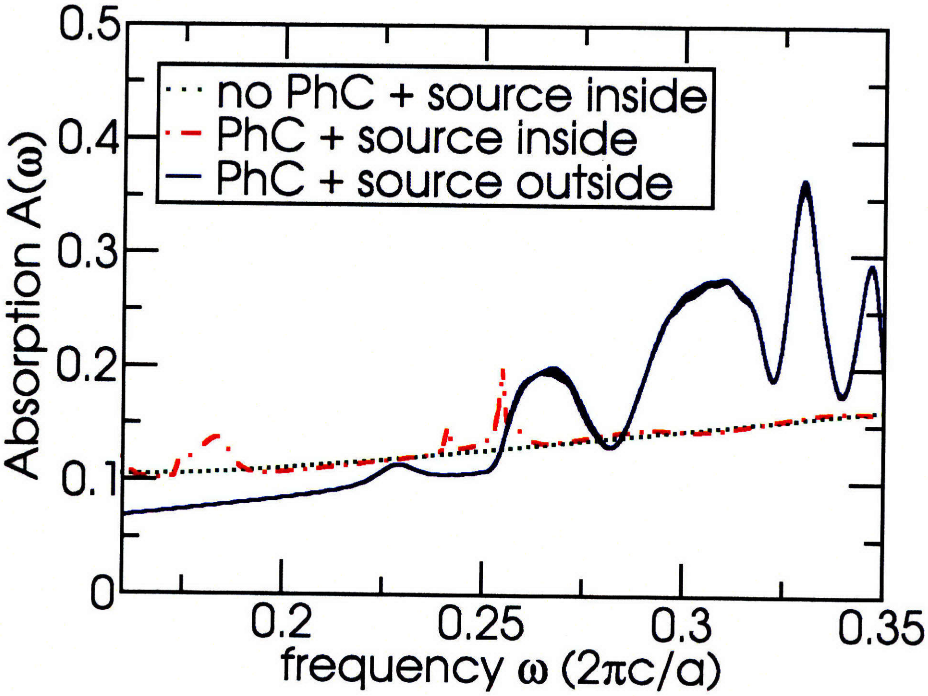

Figure 4-9: Absorption versus frequency for TE modes at oblique incidence for a photonic crystal consisting of 3 layers of a 2D lattice of air holes with $r = 0.55a$ and period $1.375a$.

However, when I optimize the parameters for a 2 μm-thick sample of c-Si, two findings are made: first, that a triangular lattice offers a performance superior to the square hole structure, and second, that the lattice parameters will be changed from those used above. The optimal lattice period a is found to be 305 nm, corresponding to a layer thickness of 264 nm. The air holes in the bulk have radius $r = 0.375a$, while the front layer has a slightly flattened, nearly rectangular structure with a fill factor of 0.5 and a thickness of 145 nm, in order to maximize diffraction events. The efficiency as a function of the number of rows for the optimized structure are given in table 4.2.

# rows	efficiency η (%)
1	14.08
2	14.90
3	15.32
4	15.50
5	15.59
6	15.70
7	15.73
8	15.74

Table 4.2: Efficiency of the solar cell design in Fig. 4-5(c) (with a 2D triangular lattice of air holes) as a function of the number of layers of air holes.

Comparison of DBR with photonic crystal based designs

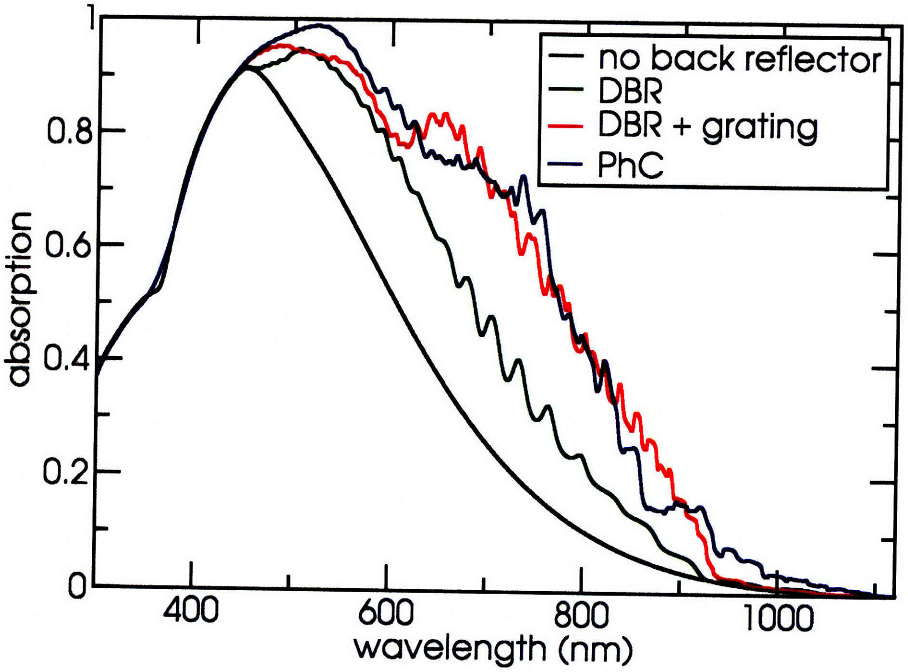

Figure 4-10: Absorption vs. wavelength at normal incidence for four 2 μm-thick Si cell designs: no back reflector, plain DBR, a DBR plus a 1D-periodic grating, and finally, a 2D photonic crystal of air holes in silicon. The last two designs consist of six complete layers. The photonic crystal-based design yields the highest efficiency.

The absorption spectra at normal incidence of four different 2 μm-thick c-Si solar cells are shown in Fig. 4-10. Note that the narrow peaks seen in Fig. 4-3 are smoothed out with a moving average that preserves the area under the curve. The designs and their overall power generation efficiencies are as follows: a simple anti-reflection coating (no back reflector), with an overall efficiency of 9.07%; an AR coating plus 10 bilayers of DBR, with an overall efficiency of 12.44%; an AR plus 6 bilayers of DBR with optimized 1D etching, with an overall efficiency of 15.46%; and finally, an AR plus 6 layers of photonic crystal air holes in a triangular lattice, with an overall efficiency of 15.59%. The photonic crystal design offers the best performance overall, due to two factors: first, the grating causes a small amount of light to be scattered into modes that are no longer reflected by the DBR, and the photonic crystal provides an extra region of silicon to absorb light – in the DBR design, the c-Si in the distributed Bragg reflector is surrounded by insulator and thus cannot contribute to current generation.

4.4 Conclusion

In conclusion, two light-trapping schemes in silicon have been studied: geometrical and wave optics. It is found that in principle, wave optics can vastly outperform geometrical optics for a certain range of wavelengths. Fortunately, only a relatively small range of wavelengths, from 600 - 900 nm, requires enhancement in thin films of c-Si. Within wave optics, it is found that photonic crystals offer the best performance because of their ability to reflect, diffract and allow partial penetration of light simultaneously within a single photonic lattice, without causing scattering losses, as in a DBR with a grating.

Chapter 5

Enhanced beam steering via photonic crystals

5.1 Introduction

Optical phased arrays, which dynamically control the phase and amplitude of light across a wavefront, are important for many applications [102, 103]. Some examples include anamorphic lensing, array generation, aberration correction, and beam steering [102, 103, 104]. Some of the latest technology uses a liquid crystal system to steer one polarization at an angle of approximately 10° [105]. As a result, achieving large angle beam steering has required multiple stages which gradually increase the angle of the light at each step [103, 105]. Furthermore, many common systems can only be modulated at rates of 1 GHz or less [102].

In this chapter, the performance of a beam steering array based on photonic crystal elements is analyzed. Such a system could steer light at any forward angle with a single stage, and be switched at high speeds. It could be made polarization insensitive [106] (as compared to the liquid crystal device) and would be a common aperture device (i.e., obey time-reversal invariance). The concept is to create a large phase contrast between elements by using photonic crystals to enhance the small index shift associated with the electro-optic effect. It is shown that if one surrounds the electro-optic material with a cavity of quality factor Q, the maximum phase sensitivity is increased by Q compared to a bare slab of material. The total phase shift associated with the presence of one resonance is π, and for m resonances, is $m\pi$. Therefore, 2 resonances are sufficient for a four-element device, which works conceptually as suggested in Fig. 5-1.

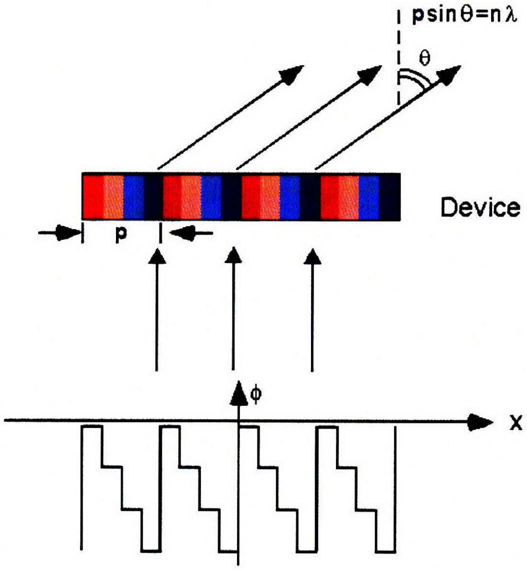

Figure 5-1: Concept for a large-angle beam steering device. The phase is modulated periodically to give rise to Bragg diffraction at certain angles.

5.2 Changing the phase of a beam of light

Consider the problem of changing the phase of a beam of light. There are several physical effects that can be used to achieve this goal. The first is changing the path length of the light through microelectromechanical (MEMS) devices. They generally switch at rates of 1 kHz or less (although some systems in the lab have approached rates of 1 MHz) [102]. Another approach to changing the phase is modulating the index of the material through which it passes. The phase change for a plane wave with frequency ω passing through a material of thickness d with index modulation Δn is $\Delta\phi = \Delta n\omega d/c$ (where c is the speed of light). This index change can be accomplished by acousto-optic devices. They can switch at speeds up to 1 GHz, but offer less index contrast (and worse performance) at higher switching rates. Electro-optic devices, based on applying a DC field to achieve a certain index change, offer the highest potential switching rate. They are generally based on either the Pockels effect (first order in field strength) and the Kerr effect (second order in field strength) [107]. There are many different electro-optic materials of each class. The best materials couple a high nonlinear index change with a low nonlinear absorption coefficient: the electro-optic figure of merit is given by the ratio of these two quantities. However, typically there is a limit to the performance of electro-optic materials for a given frequency range. Furthermore, there are limits to how much of an index change can be induced by an applied voltage before electrical breakdown occurs.

When the level of index modulation for a given device is found to be insufficient to achieve a desired phase shift directly, another approach is required for improving performance. In the structural approach, one introduces a structure that slows down light, in order to enhance the phase change that can be achieved with a given amount of nonlinear material subject to a fixed maximum voltage [108, 109]. Physically, this can be pictured as light bouncing back and forth multiple times, picking up a small phase shift on each pass. As a result of this picture, the maximum phase shift enhancement is proportional to the number of bounces, and therefore, the quality factor Q. More formally, one can write the phase ϕ associated with a collection of resonances with central frequencies ω_i and widths Γ_i as [110]:

$$\cot\phi = \sum_i \frac{2}{\Gamma_i}\left(\omega - \omega_i\right) \tag{5.1}$$

The linearity of the cotangent function near resonance yields a phase derivative $d\phi/dn|_{\omega=\omega_i} = 2/\Gamma_i = 2Q/\omega_i$, which proves the maximum enhancement is proportional to Q. Going completely across one resonance by integrating over all frequencies yields a π phase shift. Combining multiple resonances can allow for arbitrarily large phase shifts.

The simplest embodiment of this principle is a 1D photonic crystal with two resonant cavities, as shown in Fig. 5-2. This will give rise to low transmission within the bandgap except close to the two resonant frequencies. For two well-separated peaks, the adjacent peak phase difference will be given by π. One can then exploit

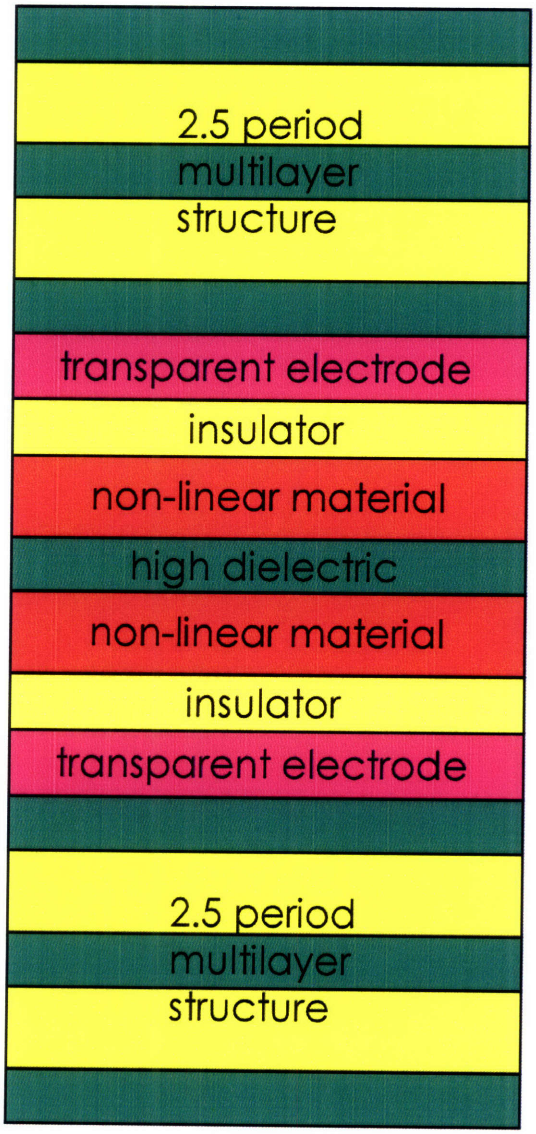

Figure 5-2: Schematic of a 1D photonic crystal, with two microcavities, 2.5 exterior bilayers and only one half interior bilayer of high dielectric. A transparent electrode, an insulator layer, and a nonlinear material layer are the 3 components of each microcavity.

this property by taking the following approach. First, choose the nonlinear material index and thickness such that the lower cavity resonant frequency coincides with the desired operating frequency. Then apply a voltage sufficient to shift the higher frequency peak down to the operating frequency. Now, the phase of the output will be π out of phase with what was observed previously. The thickness of the device proposed in Fig. 5-2 is about $8.2a$ when using high and low indices of $n_{\text{hi}} = 2.4$ and $n_{\text{low}} = 1.6$, respectively. Converting to physical distances yields device thicknesses of

12.3 cm at 5 GHz, and 1.23 m at 500 MHz. The thicknesses could be reduced by at least 32% through the use of very high index contrast materials. Furthermore, note that the fractional bandwidth of the phase shifting effect will be inversely proportional to the quality factor of the cavity. Therefore, if a bandwidth of about 3% of the central frequency is required, this could be achieved using a relatively low quality factor $Q \leq 33$.

Using a high and low dielectric of indices $n_1 = 2.4$ and $n_2 = 1.6$ and period a with 2.5 exterior bilayers and only a half interior bilayer yields two resonant peaks within the bandgap at normal incidence, centered around $\omega = 0.25(2\pi c/a)$, with a quality factor $Q \approx 40$, which corresponds to a bandwidth of approximately 2.5% of the central frequency. Choosing the microcavities to have equal thicknesses of $1.5a$ and indices of $n_c = 1.178$ and $n_c = 1.6324$ yields the result shown in Fig. 5-3: two different resonances overlapping at the same frequency. According to equation (5.1), the peaks of the two resonances should differ in phase by π. This prediction is checked in Fig. 5-4, which shows that the fields as a function of time for the two microcavity index values are very close to being π out of phase with one another.

By comparison, the phase change associated with a layer of nonlinear material with thickness $1.5a$ and equal index change is only 0.341π, about a third of the phase change seen for this device.

Note that the parameters used in this discussion are just an example, and one can use this design with any frequency where dielectric media can be treated macroscopically, ranging from radio frequencies to ultraviolet light. The most important materials choice is the non-linear material, which should be chosen to have a large figure of merit.

Furthermore, any bandwidth that's not extremely broad (i.e., less than 10% of mid-range frequency) could conceivably be used in this device with proper choice of dielectric materials. There is, however, a tradeoff between bandwidth and index contrast: the smaller the bandwidth needed, the lower the index contrast needed, and vice-versa. As a consequence, one can achieve a π phase shift for monochromatic light with an arbitrarily small index contrast given a sufficiently high quality factor

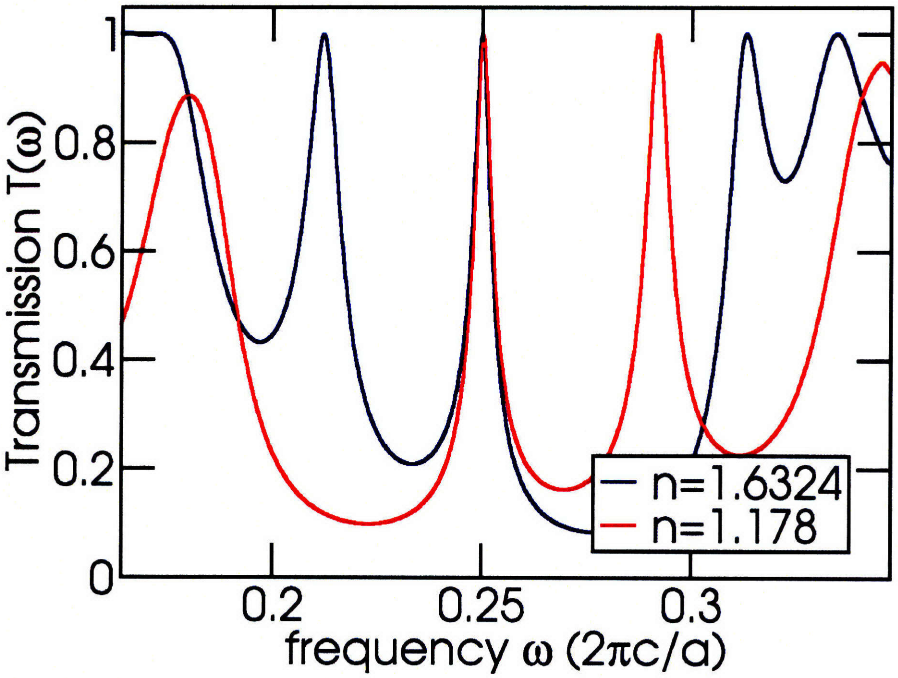

Figure 5-3: Transmission as a function of frequency for two values of the index of the microcavity, $n_c = 1.178$ and $n_c = 1.6324$, chosen to shift two different resonances to the same central frequency $\omega = 0.25(2\pi c/a)$.

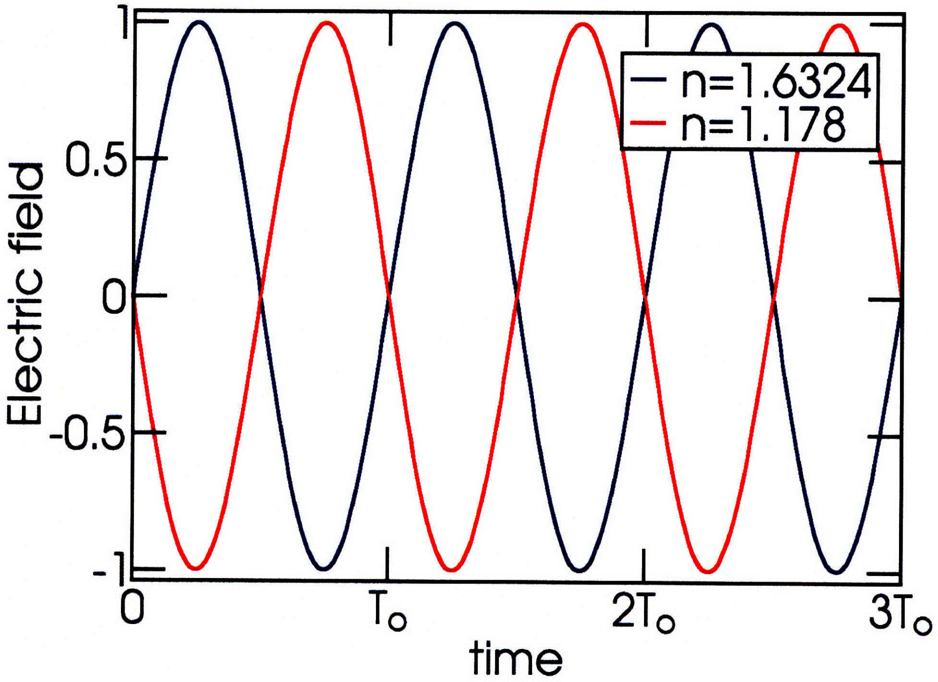

Figure 5-4: Electric fields as a function of time at a point opposite the source for two values of the index of the microcavity, $n_c = 1.178$ and $n_c = 1.6324$. The two outputs are π out of phase with respect to one another.

cavity.

5.3 Designing a beamsteering device

The introduction of a $\pi/2$ phase shift between each element, each of which has a transverse size of $p/4$, gives rise to a periodic array of periodicity p that will diffract light at an angle specified by the Bragg diffraction formula, $\sin\theta = \lambda/p$.

In Fig. 5-5, four specific index values are found that can achieve precisely the required phase shift between each element, to wit: n =2.1195, 2.1317, 2.2851, and 2.3022.

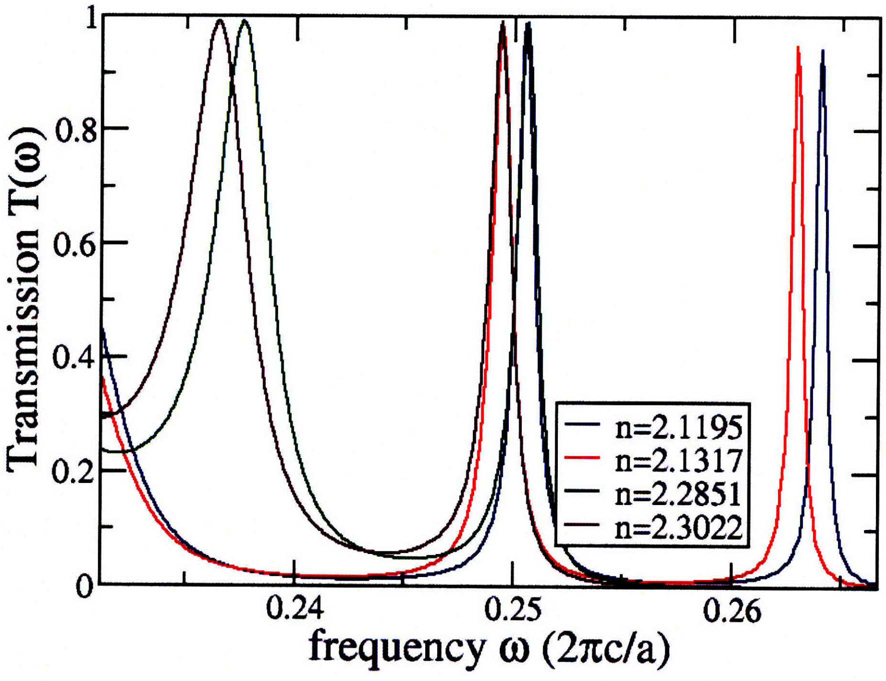

Figure 5-5: Transmission versus frequency for a single device with four different electrooptic material refractive indices. These indices (shown in the legend) are chosen such that all the half-maxima coincide, thus yielding a phase shift of $\pi/2$ between each device.

The proposed design for the four-element periodic device is shown in Fig. 5-6. The operation of this device is simulated for continuous wave operation at the wavelength

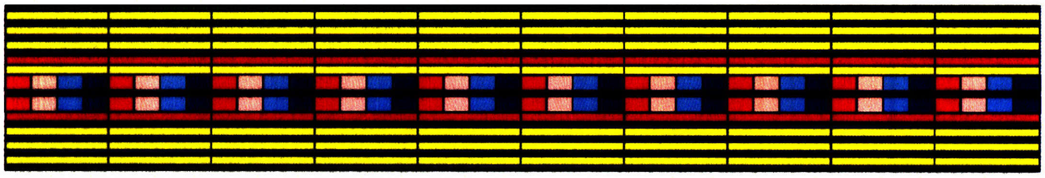

Figure 5-6: Ten periods of a photonic crystal beamsteering device employing four steps per period.

$\lambda = 4a$. The lateral periodicity p is then chosen to be $p = 4.8a$, so that steering will occur at the angle $\theta = \sin^{-1}(\lambda/p) \approx 56°$. Of course, when the device is turned off (i.e., each nonlinear element has an applied voltage of zero), no beamsteering is expected to occur. As shown in Fig. 5-7, all the light is either transmitted forward with no deflection, or reflected backwards, since the phase is the same through each device. However, when the voltages are turned on, the forward beam is seen to be steered at an angle of 52°, fairly close to the theoretical prediction of 56°, as shown in Fig. 5-8,. Most of the difference probably comes from the finite length of time over which the simulation is run, since the beam gradually shifts to the correct angle as the fields build up in the microcavities. Furthermore, note that the beam width is substantially unaffected, which is necessary for any real applications.

It should be noted that the design presented in this chapter has a couple of key drawbacks. The first is that only 50% of the incoming light is steered in the desired direction, due to the basic approach of using resonances shifted by a phase of $\pi/2$, which requires operating at half-maximum. The alternative approach of using the peaks of two resonances would not break σ_y (left-right) symmetry, and would thus result in two diffracted beams in the forward direction. Thus in practice, both approaches would only yield 50% steering of the power in a particular direction. The second drawback to this design is that contacting on small scales would be required, since each element measures exactly $p/4$ across. For operation at $\lambda = 1.55\mu\text{m}$, this would require the width of each element to be $0.3\lambda = 465$ nm.

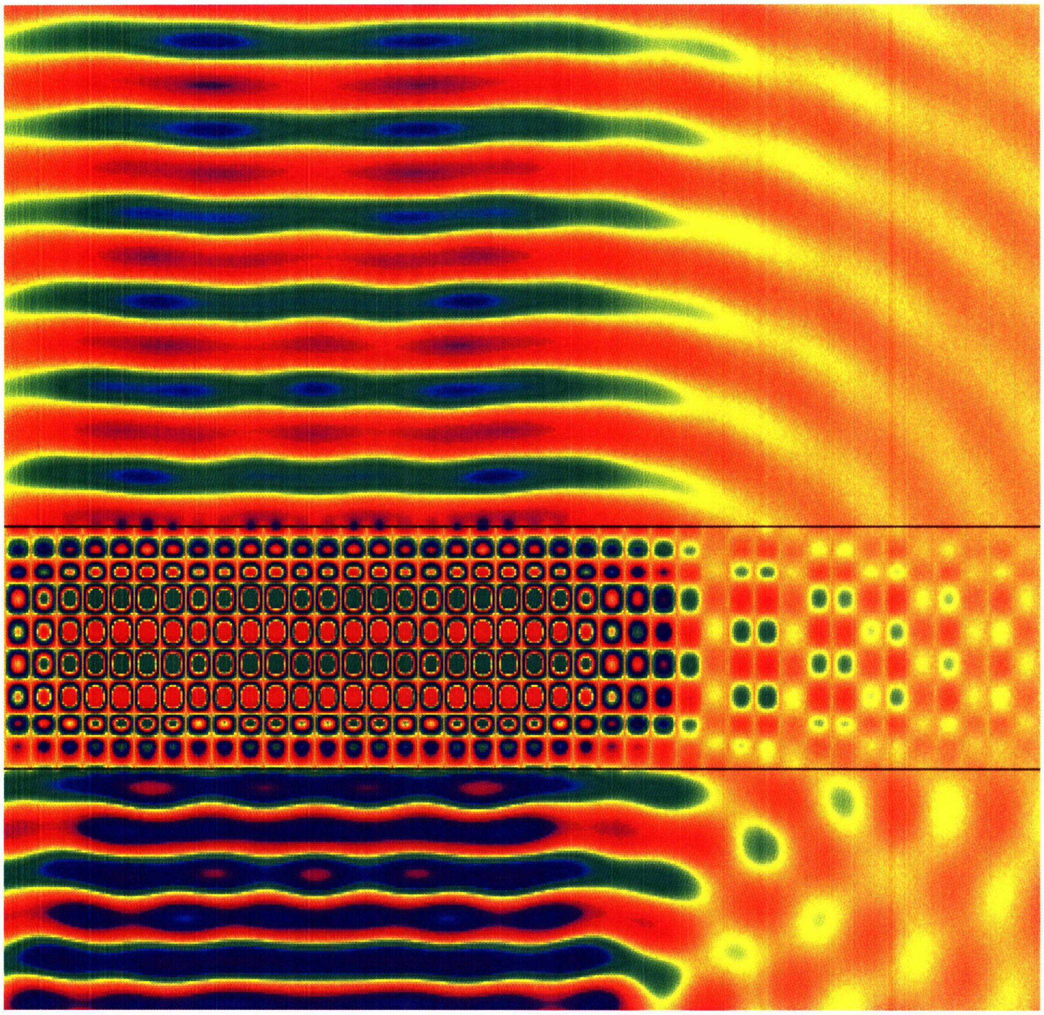

Figure 5-7: Illustration of the photonic beamsteering device with all nonlinear elements turned off: no beamsteering takes place.

5.4 Conclusion

In conclusion, I have designed a system for achieving large-angle beam steering in a single stage using electro-optic materials. This system has the advantage of being able to exploit small changes in index to steer light to any forward angle desired with the proper design. It also can operate at very high bandwidths compared to previous systems.

Some of the most interesting future work will consist in experiments: choosing materials, fabricating a structure and characterizing it in the laboratory. In conjunction with that, future theoretical work should include full 3D modeling of the experimen-

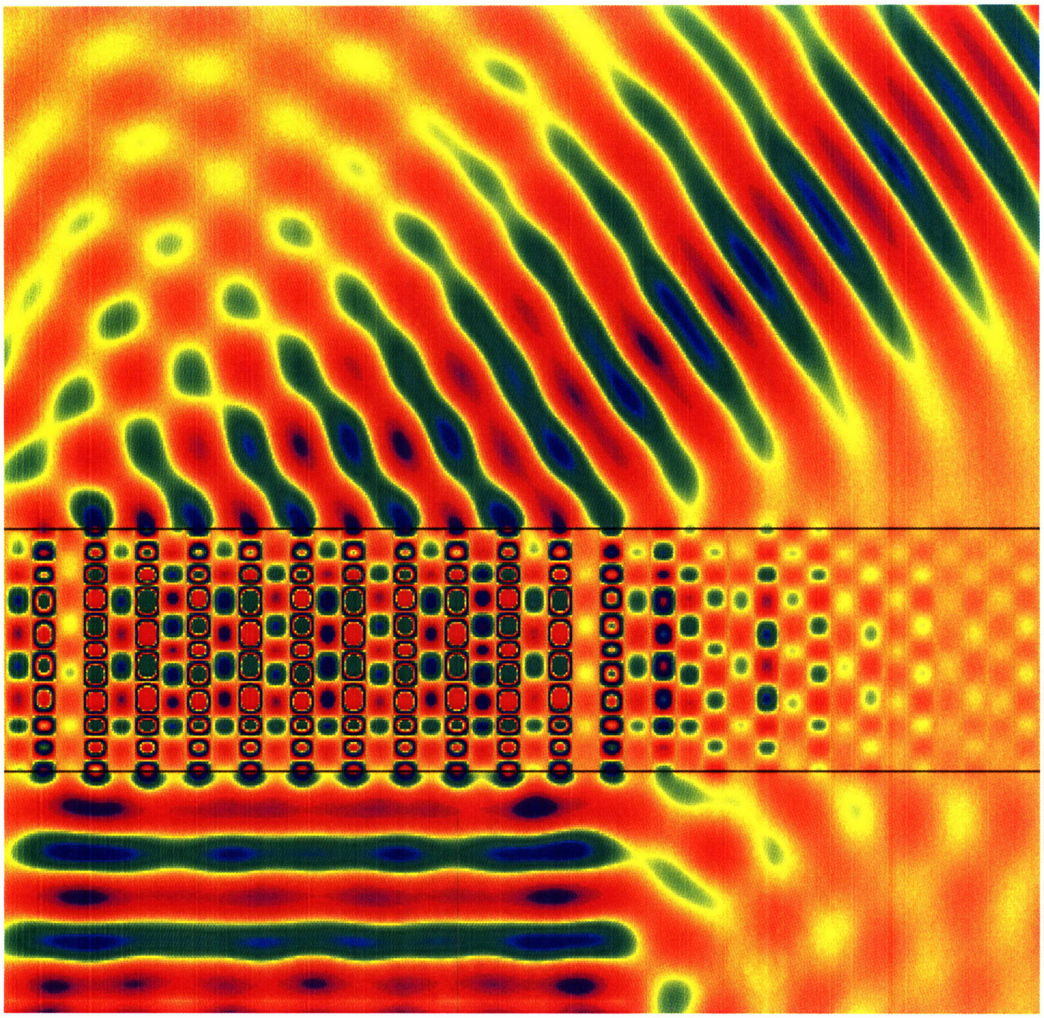

Figure 5-8: Illustration of the photonic beamsteering device with the nonlinear elements turned on: beamsteering at a well-controlled 52° angle takes place.

tal systems, and extending the work to include multiple wavelengths. Being able to bend light by a constant amount from any incident angle or polarization would also be a potential direction that could be pursued theoretically.

Chapter 6

Single-photon all-optical switching using waveguide-cavity QED

6.1 Introduction

Several emerging technologies, such as integrated all-optical signal processing and all-optical quantum information processing, require strong and rapid interactions between two distinct optical signals [111]. Achieving this goal is a fundamental challenge because it requires a unique combination of large nonlinearities and low losses. The weak nonlinearities found in conventional media mean that large powers are required for switching. However, nonlinearities up to 12 orders of magnitude larger than those observed in common materials [112] with low losses can be achieved using EIT materials [24, 112, 113]. One can then envision inducing strong interactions between two very weak signals of different frequencies by placing a 4-level EIT atom in a high-quality factor (high-Q) cavity, so that a very small signal at a specific atomic transition frequency could shift another resonant frequency of the system by a measurable amount [114]. This approach differs from several optical switching schemes for small numbers of photons that have previously been discussed in the literature. One of the pioneering papers in this area used a single three-level atom with a V-level structure in an optical cavity to induce a cross-phase modulation of 16° between two photons [115]. EIT offers even further opportunities in terms of larger nonlinearities and greater tunability, which has directed much subsequent work in this direction. EIT materials have been predicted to cause a photon blockade effect, where the state of a cavity can be switched by the self-phase modulation of a single photon [116, 117, 118] or several photons [119, 120]. This effect has recently been observed experimentally [121]. Ref. [122] predicts that ensembles of EIT atoms can be modulated to create quantum entangled states for a small number of photons. An alternative method is discussed in Ref. [123], whereby a laser beam can control the relative populations of a two-state system embedded in a PhC, which switches its transmission properties at low power levels.

Ref. [114] semi-classically demonstrates the strong interaction of very low intensity fields which can be mediated by EIT materials. This work extends that idea to the quantum regime, by writing down the waveguide-cavity QED Hamiltonian for a system consisting of one or a few 4-level EIT atoms strongly coupled to a photonic crystal (PhC) cavity mode, which in turn is coupled to a PhC waveguide, and solving it exactly. Furthermore, an approach to calculating the relevant parameters from first principles is demonstrated. It should be experimentally feasible, with EIT having already been demonstrated in a Pr doped Y_2SiO_5 crystal [124, 125]. Note that compared to EIT systems such as Na BEC's displaying narrow bandwidths (e.g., 2 MHz [112]), switching can occur over much larger bandwidths even for single photon power levels (e.g., 2 GHz, using the parameters from Ref. [126]) because the PhC cavity compensates for weaker nonlinearities, as demonstrated in this chapter. Furthermore, this approach utilizes PhC's, which offer confinement of light to high quality factor microcavities with low modal volumes, which facilitates strong coupling between light and matter. The emergence of new phenomena associated with the quantization of the probe and gate fields (e.g., Rabi-splitting) is discussed. Finally, it is shown that switching behavior can be achieved with single probe and gate photons, and the physical parameters needed to achieve such operations are calculated.

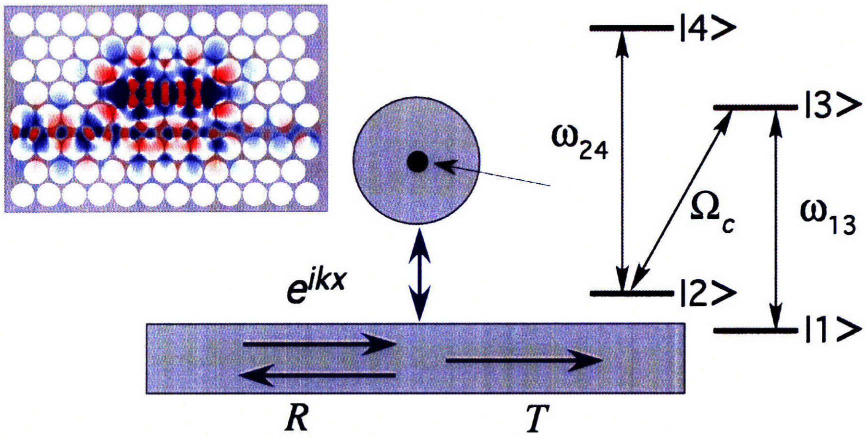

Figure 6-1: Schematic illustration of the system investigated. A waveguide is coupled to a cavity with an EIT atom at its center. In the upper left-hand corner, an FDTD simulation that can be used to calculate the model parameters is shown.

6.2 Theoretical model

Consider the following design, illustrated in Fig. 6.2. There is a cavity which supports two resonant modes, one with a resonant frequency ω_{RES} and the other with a control frequency ω_{CON}, enclosing a single four-level EIT atom with coupling strengths g_{ij} and atomic transition frequencies ω_{ij}, where i and j refer to the initial and final atomic states, respectively. The EIT dark state is created by adding a classical coupling field to the cavity with frequency ω_{23} and Rabi frequency $2\Omega_c$ – all other quantities are treated quantum mechanically. In general, any number of coupling schemes between the cavity and one or more waveguides could be utilized. However, in this chapter, the ω_{RES} cavity mode is side-coupled to an adjacent single-mode waveguide with a radiative linewidth $\Gamma_w = \omega_{\text{RES}}/2Q_w = V_w^2/v_g$, where Q_w is the quality factor of the ω_{RES} cavity mode, V_w is the coupling strength and v_g is the group velocity in the waveguide – its dispersion relation $\omega(k)$ is assumed to be approximately linear near the ω_{RES} resonance. For relatively strong cavity-waveguide couplings, radiative couplings out of the system are much smaller and may be neglected. Also, the ω_{CON} resonance is designed to have a much smaller decay rate $\Gamma_{\text{CON}} = \omega_{\text{CON}}/2Q_{\text{CON}}$. This can be achieved by starting with two dipole modes, one with an even symmetry coupled strongly to the waveguide, and one with an odd symmetry exactly decoupled from the waveguide. A slight shift in the cavity position can then create a slight coupling that nonetheless creates a substantial disparity in quality factors, i.e., $Q_{\mathrm{CON}} \gg Q_w$ (see, e.g., Refs. [1, 127]). Alternatively, one could use two cavities to create even and odd modes with substantially different quality factors [128]. In the absence of an atom, these design produces a Lorentzian lineshape for the *reflection* (because of the side-coupling), centered around ω_{RES} [129]. A photonic crystal implementation of this is shown in the upper left-hand corner of Fig. 6.2 – a triangular lattice of air holes in silicon with radius $0.48a$ that has a complete 2D photonic bandgap. A similar geometry has been used for quantum dots in photonic crystal microcavities, as in Ref. [126]. That experimental system exhibits a critical photon number $m_0 = \Gamma_3^2/2g^2 = 0.55$ and critical atom number $N_0 = 2\Gamma_w\Gamma_3/g^2 = 4.2$. Ideally both of these numbers would be less than one for quantum information processing [130]; it should be possible to achieve this goal with improvements in the quality factor Q or the modal volume V_{mode}, or by placing several atomic or quantum dot systems in the same microcavity. Note that it could also be possible to achieve similar behavior with other physical systems, such as high-finesse Fabry-Perot optical microcavities [131], or ultrahigh-Q toroidal microresonators [132].

Combining Ref. [117]'s Hamiltonian for an EIT atom in a cavity and Ref. [133]'s Hamiltonian for a waveguide interacting with a cavity yields:

$$\begin{aligned} H/\hbar = \quad & \sum_k \omega_k a_k^\dagger a_k + \omega_{\mathrm{RES}} a^\dagger a + \omega_{\mathrm{CON}} b^\dagger b + \sum_k V_w (a_k^\dagger + a_k)(a^\dagger + a) + \omega_{21}\sigma_{22} \\ & + (\omega_{13} - i\Gamma_3)\sigma_{33} + (\omega_{14} - i\Gamma_4)\sigma_{44} + \Omega_c(\sigma_{32} + \sigma_{23}) \cos(\omega_{23} t) \\ & + g_{13}(a^\dagger \sigma_{13} + a\sigma_{31}) + g_{24}\left(b^\dagger \sigma_{24} + b\sigma_{42}\right) \end{aligned} \tag{6.1}$$

where a_k are the annihilation operators for waveguide states of wavevector k and frequency ω_k, a and b are the annihilation operators for cavity photon states of frequencies ω_{RES} and ω_{CON}, respectively (which are considered in this chapter to be singly occupied), σ_{ij} are the projection operators that take the atomic state from j to i, Γ_3 is the nonradiative decay rate of the third level, Γ_4 is the nonradiative decay rate of the fourth level, $\Delta\tilde{\omega}_{13} = \omega_{13} - \omega_{\mathrm{RES}} - i\Gamma_3$ is the complex detuning of the 1→3 transition from ω_{RES}, and $\Delta\tilde{\omega}_{24} = \omega_{24} - \omega_{\text{CON}} - i\Gamma_4$ is the complex detuning of the 2→4 transition from ω_{CON}. In this chapter, the cavity resonance is designed to match the 1→3 transition, i.e., $\omega_{\text{RES}} = \omega_{13}$, so that $\Delta\tilde{\omega}_{13} = i\Gamma_3$. Also, although $\Delta\tilde{\omega}_{24}$ is predominantly real, in general there is an imaginary part corresponding to absorption losses in the fourth level. However when the detuning greatly exceeds the decay rate of the upper level, this contribution may be neglected. Losses from the second atomic level are also neglected, since typically it is a metastable state close to the first atomic level in energy. Finally, although in general the two cavity modes should have at least slightly different frequencies, ω_{CON} is set equal to ω_{RES} for simplicity.

The Hamiltonian in equation (6.1) can then be rewritten in real space and separated into a diagonal part:

$$\begin{aligned} H_o/\hbar = \quad & \omega_{\text{RES}} \int dx \left[a_R^\dagger(x) a_R(x) + a_L^\dagger(x) a_L(x)\right] \\ & + \omega_{\text{RES}} \left(a^\dagger a + b^\dagger b + \sigma_{33} + \sigma_{44}\right) + \omega_{21}(\sigma_{22} + \sigma_{44}), \end{aligned} \tag{6.2}$$

where a_L and a_R refer to left and right moving waveguide photons, respectively, as well as an interaction part:

$$\begin{aligned} H_I/\hbar = \quad & \int dx \Big[a_R^\dagger(x)(-iv_g\partial_x - \omega_{\text{RES}}) a_R(x) + a_L^\dagger(x)(iv_g\partial_x - \omega_{\text{RES}}) a_L(x) \\ & + V_w \delta(x)(a_R^\dagger(x) a + a_R(x) a^\dagger + a_L^\dagger(x) a + a_L(x) a^\dagger)\Big] + \Omega_c(\sigma_{23} + \sigma_{32}) \\ & + g_{13}(a^\dagger \sigma_{13} + a\sigma_{31}) - i\Gamma_3\sigma_{33} + \Delta\tilde{\omega}_{24}\sigma_{44} + g_{24}(b\sigma_{42} + b^\dagger \sigma_{24}) \end{aligned} \tag{6.3}$$

via the interaction picture (using the rotating-wave approximation [23]), where the total system Hamiltonian is given by $H = H_o + H_I$. The eigenstate for the system can be written as:

$$\begin{aligned} |\psi_k\rangle = \quad & \Big\{ \int dx \left[\phi_{k,R}^+(x) a_R^\dagger(x) + \phi_{k,L}^+(x) a_L^\dagger(x)\right] + e_k a^\dagger \\ & + f_k \sigma_{31} + h_k \sigma_{21} + p_k \sigma_{41} b \Big\} \, |0,0,1\rangle_{\text{phc}} \otimes |1\rangle_{\text{atom}} \end{aligned} \tag{6.4}$$

where:

$$\begin{aligned} \phi^{+}_{k,R}(x) &= e^{ikx}\left[\theta(-x) + t\theta(x)\right] \\ \phi^{+}_{k,L}(x) &= re^{-ikx}\theta(-x), \end{aligned} \tag{6.5}$$

e_k is the probability amplitude of the cavity photon at ω_{RES}, and f_k, h_k, and p_k are the occupations of the 3rd, 2nd, and 4th atomic levels, respectively. t and r are the waveguide transmission and reflection amplitudes, respectively. All of these parameters are determined when the eigenequation is solved below. $|0,0,1\rangle_{\text{phc}} \otimes |1\rangle_{\text{atom}}$ is an eigenstate consisting of a direct product of a photonic state (phc) and an atomic state (atom). The photonic state consists of zero photons in the waveguide, zero photons in the cavity at ω_{RES}, and one photon in the cavity at ω_{CON}, respectively. The atomic state consists of a single atom in its ground state. Note that $|\psi_k\rangle$ is written in terms of an annihilation operator b in order to simplify the notation, which would otherwise require $b^{\dagger}$ operators in all but one term.

Applying the Hamiltonian, equation (6.3), to the time-independent eigenvalue equation $H_I|\psi_k\rangle = \hbar\epsilon_k|\psi_k\rangle$, where $\epsilon_k = \omega - \omega_{\text{RES}}$, and solving for the reflection coefficient yields $|r(\epsilon_k)|^2 = |\Gamma_w/(\xi - i\Gamma_w)|^2$,where:

$$\xi = \epsilon_k - \frac{g_{13}^2}{\epsilon_k + i\Gamma_3 - \frac{\Omega_c^2}{\epsilon_k - g_{24}^2/(\epsilon_k - \Delta\tilde{\omega}_{24})}} \tag{6.6}$$

6.3 Results and discussion

The parameters g_{13}, V_w (or Γ_w), v_g, and Ω_c of equation (6.3) can be determined from a numerical solution to Maxwell's equations (e.g., via [134]) as follows. First, the cavity mode is excited by a source, and the modal volume of the cavity is found from the field patterns by $V_{\text{mode}} = \left(\int_{\text{mode}} d^3x\epsilon\,|\mathbf{E}|^2\right)/\epsilon\,|\mathbf{E}_{max}|^2$. One can then apply the formula $g_{13} = \sqrt{\pi e^2 f_{13}/m\epsilon V_{\text{mode}}}$ [20], where e is the elementary electric charge, ϵ is the dielectric constant of the medium in which the atomic system is embedded, m is the free electron mass, and f_{13} is the oscillator strength for the $|1\rangle \rightarrow |3\rangle$ transition (1/2 in Na [112]). The linewidth Γ_w can be calculated by examining the decay rate of the field in the cavity mode. The waveguide group velocity is given by $v_g = \frac{d\omega(k)}{dk}\Big|_{\omega=\omega_{\mathrm{RES}}}$. Finally, the Rabi frequency Ω_c can be estimated from quantum mechanics by first determining the vacuum Rabi splitting for the 2→3 atomic transition g_{23}, and then multiplying by $\sqrt{n}$, where n is the number of ω_{23} photons.

First, consider the case of a 2-level atomic system (i.e., $\Omega_c = 0$, $g_{24} = 0$), with a waveguide coupling Γ_w and a non-radiative decay rate Γ_3. For a fixed atom-photon coupling g_{13} and zero non-radiative absorption, the single resonant mode at $\epsilon_k = 0$ experiences a Rabi splitting into two orthogonal linear superpositions of the cavity and atom modes at $\epsilon_k = \pm g_{13}$. As long as one remains in the strong coupling regime $g_{13} > \Gamma_3/2$, the absorption for all frequencies increases nearly linearly with Γ_3.

However, in the opposite regime of weak coupling ($g_{13} < \Gamma_3/2$), the normal modes of the system are mostly photonic (lossless) or mostly atomic (very lossy). This phenomenon eliminates the Rabi splitting and gives rise to a reflection nearly indistinguishable from a system without an atom for sufficiently large Γ_3.

Now, consider a 3-level atomic system without losses. Compared to the 2-level system, a third mode, corresponding to the dark state of the EIT atom, will emerge at $\epsilon_k = 0$ between the previously observed Rabi-split peaks. The dark eigenstate is given by $|\psi\rangle_{\mathrm{dark}} = \left[a^\dagger - (g_{13}/\Omega_c)\sigma_{21}\right] |0,0,0\rangle_{\mathrm{phc}} \otimes |1\rangle_{\mathrm{atom}}$. The width of the central peak is expected to scale as $(\Omega_c/g_{13})^2$ for small Ω_c/g_{13} [122]. If one substitutes the expression given in Ref. [20] for g_{13}, one obtains the classical results found in Refs. [112, 114]. Meanwhile, the width of the side peaks is set by Γ_w and remains roughly constant as one tunes the parameters of the system.

In Fig. 6.3, $g_{13}/\Omega_c = 2$ while g_{13} is varied. It is shown that as g_{13} is decreased, the central resonance width stays constant, while the distance between the central and Rabi-split peaks becomes smaller. For use in applications, it therefore seems optimal to have a large Rabi splitting, corresponding to the very strong coupling limit, which can also be viewed as corresponding to critical photon and atom numbers much less than one. The experimental values for a system with a single quantum dot emitting a single photon observed in Ref. [126] correspond to a regime where

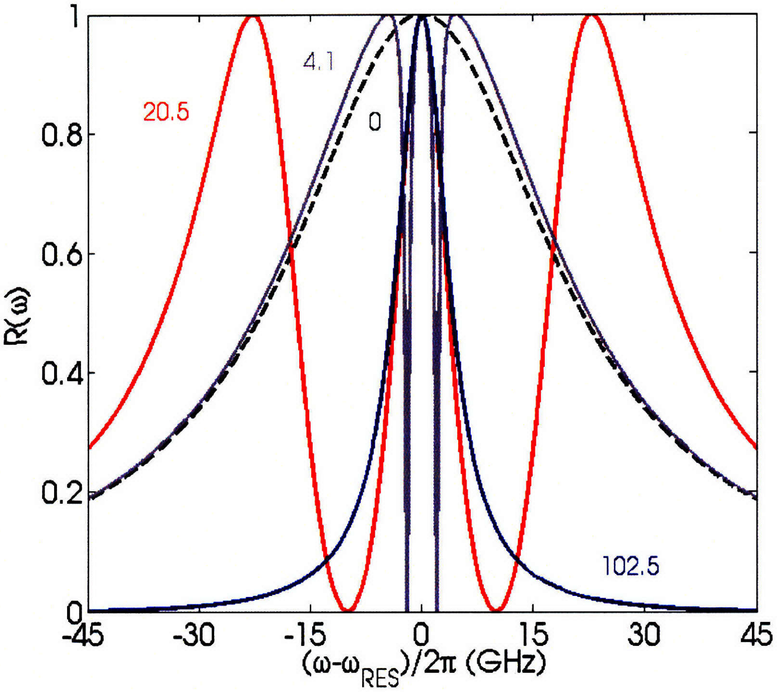

Figure 6-2: Waveguide reflection for a lossless 3-level EIT atom for the four labelled values of the atomic coupling strength g_{13}, in GHz. The radiation rate $\Gamma_w = 21.5$ GHz and the ratio $g_{13}/\Omega_c = 2$ are fixed. Larger g_{13} produces larger peak separations (the blue curve shows Rabi peaks outside of the plot), favorable for switching.

$g_{13} \approx \Gamma_w$ – specifically, they find that for operation at $\lambda = 1.182$ μm, $g_{13} = 20.5$ GHz and $\Gamma_w = 21.5$ GHz; note that PhC microcavities are optimal for simultaneously decreasing Γ_w and increasing g_{13}.

Now, consider a 4-level system with a control photon present. Two possible effects can be induced by the control photon. When the control frequency ω_{CON} is close to the electronic transition frequency ω_{24}, an Autler-Townes doublet is observed; upon detuning, an AC-Stark shift will be induced in this system instead [114, 117]. The latter effect has been suggested as a switching mechanism in Refs. [114, 135, 136]. This can be shown by using equation (6.6) to calculate the poles of the EIT term in the reflection, i.e., set $\epsilon_k - g_{24}^2/(\epsilon_k - \Delta\tilde{\omega}_{24}) = 0$, which yields $\epsilon_k = \pm g_{24}$ for no detuning, and $\epsilon_k \approx -g_{24}^2/\Delta\tilde{\omega}_{24}$ for a large detuning, matching the semi-classical result found in Ref. [114].

Single-photon switching is obtained when the reflection peak is shifted by an

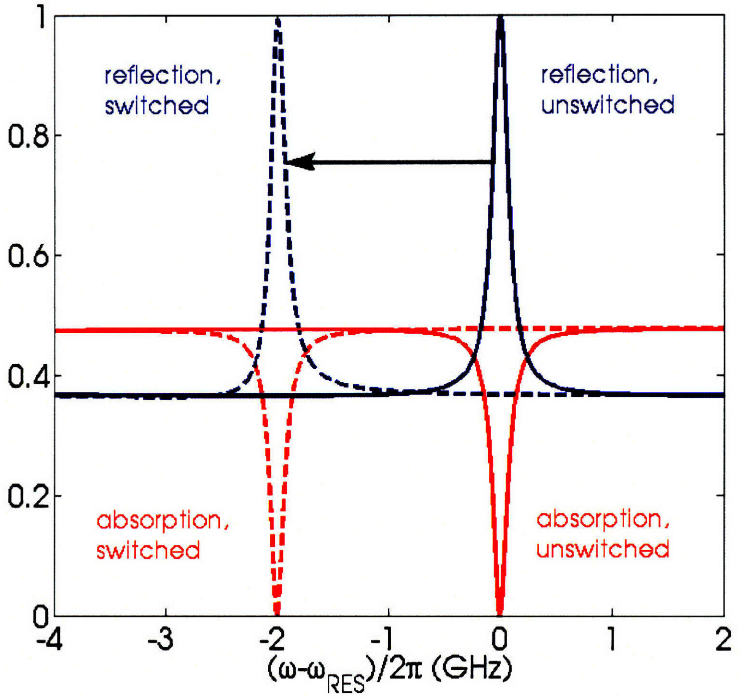

Figure 6-3: Waveguide reflection (blue) and absorption (red) in the absence (solid) and presence (dashed) of an control photon, demonstrating nonlinear single-photon switching ($\Gamma_w = 21.5$ GHz, $g_{13} = 20.5$ GHz, $\Omega_c = 2$ GHz, $\Gamma_3 = 30$ GHz, $g_{24} = 8$ GHz, and $\Delta\tilde{\omega}_{24} = 30$ GHz).

amount greater than its width, via the presence or absence of one control photon. In order to achieve this goal, one can take two different approaches. First, in the regime where $g_{13} \approx \Gamma_w$, as in Ref. [126], one can introduce an absorption via $\Gamma_3 \neq 0$, and thus absorb the majority of light not coupled to the dark state. In Fig. 6.3, the reflection and absorption are plotted for an optimized value of $\Gamma_3 = 30$ GHz, both before and after switching. As shown, reflections at the Rabi-split frequencies are decreased substantially (to about 40%), while full reflection is still observed at the central, EIT-narrowed peak. Furthermore, in the presence of a single detuned control photon, it is possible to switch the peak reflection frequency by an amount greater than the EIT-narrowed central peak width. A second, lossless approach, appropriate if producing a large nonradiative decay Γ_3 or small Ω_c is difficult in a single-atom device, is to enhance the ratio g_{13}/Γ_w. This goal can be achieved by either decreasing Γ_w or V_{mode}, or by increasing the number of atoms from one to N. The first example of switching by

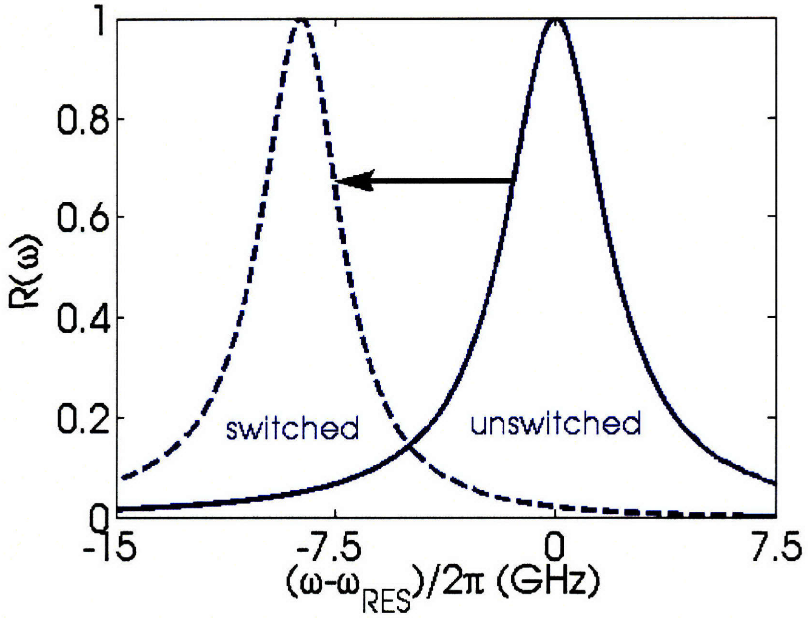

Figure 6-4: Waveguide reflection with (dashed) and without (solid) a control photon, demonstrating lossless switching, where a higher quality factor has made the resonant peaks narrow enough to be shifted by more than their full width at half maximum by a single photon ($\Gamma_w = 3$ GHz, $g_{13} = 20.5$ GHz, $\Omega_c = 30$ GHz, $\Gamma_3 = 0$, $g_{24} = 30$ GHz and $\Delta\tilde{\omega}_{24} = 20$ GHz).

decreasing the waveguide coupling is shown in Fig. 6-4, where the waveguide coupling width Γ_w is decreased by about a factor of 7 to $\Gamma_w = 3$ GHz. Now the peaks are narrow enough that a single photon of frequency ω_{CON} can shift the peak by more than the full width at half-maximum. The second example of switching, by increasing the number of atoms is illustrated in Fig. 6-5. In general, it is clear that increasing the number of atoms collectively oscillating will improve the coupling strength; in the special case where each atom has equal coupling to the field, the N-atom treatment in Ref. [137] shows that the coupling constant $g_{13} \to g'_{13} = g_{13}\sqrt{N}$. Furthermore, one can generalize the arguments of Ref. [137] to a four-level system of N atoms to show that the other coupling constants g_{24} and Ω_c will scale in an identical fashion (i.e., $g_{24} \to g'_{24} = g_{24}\sqrt{N}$, $\Omega_c \to \Omega'_c = \Omega_c\sqrt{N}$). This collective Rabi oscillation separates the Rabi-split peaks much further from the central peak. Fig. 6-5 shows switching exploiting this phenomenon based on parameters from Ref. [126] and using $N = 49$. The advantage of this lossless switching scheme is that one obtains a substantially

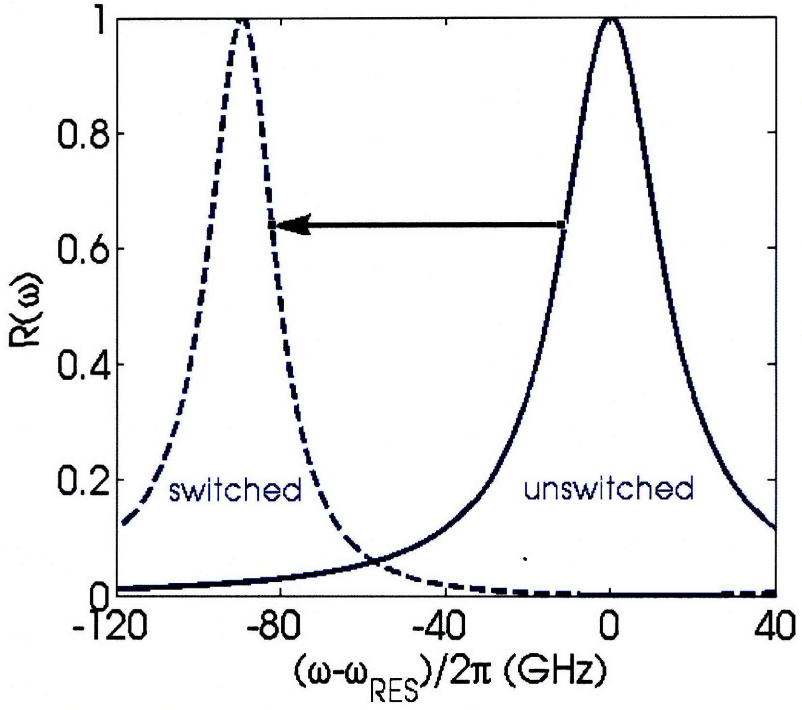

Figure 6-5: Waveguide reflection with (dashed) and without (solid) a control photon, demonstrating lossless switching, where multiple (49) EIT atoms have been used to push the Rabi-split peaks farther away in the presence of negligible loss ($\Gamma_w = 21.5$ GHz, $g_{13} = 143.5$ GHz, $\Omega_c = 210$ GHz, $\Gamma_3 = 0$, $g_{24} = 210$ GHz and $\Delta\tilde{\omega}_{24} = 20$ GHz).

greater tuning range and contrast (the difference between the peaks and the troughs) than with the lossy ($\Gamma_3 \neq 0$) scheme.

In conclusion, the reflection peak of a waveguide-cavity system can be switched in and out of resonance by a single gating photon, assuming realistic experimental parameters. Thus, one photon can be used to gate another photon of a different frequency, via a Kerr cross-phase modulation. This approach is distinct from the photon blockade system where self-phase modulation is responsible for the switching behavior. Under proper circumstances, this can give rise to two-photon entangled states. The integration of microcavities and waveguides in the same photonic crystal means that the entanglement could be preserved, in principle, throughout the system, which could be of use for quantum information processing [130].

Chapter 7

Tailoring optical nonlinearities via the Purcell effect

7.1 Introduction

Optical nonlinearities have fascinated physicists for many decades because of the variety of intriguing phenomena that they display, such as frequency mixing, supercontinuum generation, and optical solitons [107, 138]. Moreover, they enable numerous important applications such as higher-harmonic generation and optical signal processing [51, 107, 139]. On a different note, the Purcell effect has given rise to an entire field based on studying how complex dielectric environments can strongly enhance or suppress spontaneous emission from a dipole source [21, 22, 42, 140, 141]. In this chapter, I demonstrate that the Purcell effect can also be used to tailor the effective nonlinear optical susceptibility. While this is a general physical principle that applies to a wide variety of nonlinearities, I specifically investigate the Kerr nonlinearity, which is present in most materials, modeled here as resulting from the presence of two-level systems. I show theoretically that using the Purcell effect for frequencies close to an atomic resonance can substantially influence the resultant Kerr nonlinearity for light of all (even highly detuned) frequencies. For example, in realistic physical systems, enhancement of the Kerr coefficient by one to two orders of magnitude could be achieved.

In hindsight, the modification of nonlinearities through the Purcell effect could be expected intuitively: optical nonlinearities are caused by atomic resonances, so varying their strengths should influence the strengths of nonlinearities as well. Nevertheless, to the best of my knowledge, this interesting phenomenon has not thus far been described in the literature. Moreover, it displays some unexpected properties. For example, while increasing spontaneous emission strengthens the resonance by enhancing the interaction with the optical field, it actually makes the optical nonlinearity weaker. Furthermore, phase damping (e.g., through elastic scattering of phonons), which is detrimental to most optical processes, plays an essential role in this scheme, because in its absence, these effects disappear.

7.2 Theoretical model

A simple, generic model displaying Kerr nonlinearity is a two-level system. Its susceptibility has been calculated to all orders in both perturbative and steady state limits [107]. However, this derivation is based on a phenomenological model of decay observed in a homogeneous medium, and does not necessarily apply to systems in which the density of states is strongly modified, such as a cavity or a photonic crystal bandgap. Following an approach similar to Ref. [142], the validity of this expression can be established from a more fundamental point of view. Start by considering a collection of N two-level systems per unit volume in a photonic crystal cavity, whose levels are labeled a and b. The corresponding Hamiltonian is given by the sum of the self-energy and interaction terms (H_0 and $V(t)$, respectively). Using the electric dipole approximation, one obtains:

$$H = H_0 + V(t) = \hbar \left[\omega_a \sigma_{aa} + \omega_b \sigma_{bb} + \Omega(t)\sigma_{ab} + \Omega^*(t)\sigma_{ba} \right], \tag{7.1}$$

where $\sigma_{ij} = c_i^\dagger c_j$ is the operator that transforms the fermionic state j to the fermionic state i, $\Omega(t) = -\vec{\mu} \cdot \vec{E}(t)/\hbar$ is the Rabi amplitude of the applied field as a function of time, and the scalar dipole moment μ is defined in terms of its projection along the applied field $\vec{E}(t)$. In general, if this system is weakly coupled to the environmental degrees of freedom, then the timescale for the observable dynamics of the system is less than the timescale of the "memory" of the environment. In this case, information sent into the environment is irretrievably lost – this is known as the Markovian approximation [143]. The dynamics of this system can then be modeled by the Lindbladian $\mathcal{L}$, which is a superoperator defined by $\dot{\rho} \equiv \mathcal{L}[\rho]$. In general, one obtains the following master equation from the Lindbladian:

$$\dot{\rho} = -(i/\hbar)[H,\rho] + \sum_{\mu}\left[L_\mu \rho L_\mu^\dagger - \frac{1}{2}L_\mu^\dagger L_\mu \rho - \frac{1}{2}\rho L_\mu^\dagger L_\mu\right] \tag{7.2}$$

Using the only two quantum jump operators that are allowed in this system on physical grounds – $L_1 \equiv \sigma_{ab}/\sqrt{T_1}$ and $L_2 \equiv \sigma_{bb}\sqrt{\gamma_{\text{phase}}}$ [143] – one can obtain the following dynamical equations:

$$\frac{d\rho_{ba}}{dt} = -(i\omega_{ba} + T_2^{-1})\rho_{ba} + i\Omega(t)(\rho_{bb} - \rho_{aa}) \tag{7.3}$$

$$\frac{d(\rho_{bb} - \rho_{aa})}{dt} = -\frac{(\rho_{bb} - \rho_{aa}) + 1}{T_1} - 2i\left[\Omega(t)\rho_{ab} - \Omega^*(t)\rho_{ba}\right], \tag{7.4}$$

where $\omega_{ba} \equiv \omega_b - \omega_a$, T_1 is the rate of population loss of the upper level, and $T_2 = (1/2)T_1^{-1} + \gamma_{\text{phase}}$ is the rate of polarization loss for the off-diagonal matrix elements. The prediction of exponential decay via spontaneous emission is known as the Wigner-Weisskopf approximation [144]. Although it has been shown that the atomic population can display unusual oscillatory behavior in the immediate vicinity of the photonic band edge [145, 146], theoretical [142] and experimental considerations [147, 148] show that this approximation is fine for resonant frequencies well inside the photonic bandgap. In the rest of this chapter, this is assumed to be the case. Next, one can make the rotating wave approximation for Eqs. (7.3) and (7.4), and then solve for the steady state. If the polarization is defined by $P = N\mu(\rho_{ba} + \rho_{ab}) = \chi E$, where χ is the total susceptibility to all orders, one obtains the following well-known expression for the susceptibility [107, 142]:

$$\chi = -\frac{N\mu^2(\omega - \omega_{ba} - i/T_2)T_2^2/\hbar}{1 + (\omega - \omega_{ba})^2 T_2^2 + (4/\hbar^2)\mu^2|E|^2 T_1 T_2}. \tag{7.5}$$

In general, equation (7.5) may be expanded in powers of the electric field squared. Of particular interest is the Kerr susceptibility, also in Ref. [107]:

$$\chi^{(3)} = \frac{4}{3} N\mu^4 \frac{T_1 T_2^2(\Delta T_2 - i)}{\hbar^3(1 + \Delta^2 T_2^2)^2}, \tag{7.6}$$

where $\Delta \equiv \omega - \omega_{ba}$ is the detuning of the incoming wave from the electronic resonance frequency. For large detunings $\Delta T_2 \gg 1$, one obtains the approximation that:

$$\operatorname{Re}\chi^{(3)} \approx \frac{4}{3} N\mu^4 \left(\frac{1}{\hbar\Delta}\right)^3 \frac{T_1}{T_2}. \tag{7.7}$$

Of course, there are many types of materials to which a simple model of noninteracting two-level systems does not apply. However, it has been shown that some semiconductors such as InSb (a III-V direct bandgap material) can be treated as a collection of independent two-level systems with energies given by the conduction and valence bands, and yield reasonable agreement with experiment [149]. If the parameter Δ is defined in terms of the bandgap energy such that $\Delta \equiv \omega_G - \omega$, then one can look at the regime $\Delta T_2 \gg 1$ studied above, and obtain the following equation:

$$\operatorname{Re}\chi^{(3)} \approx -\frac{1}{30\pi\hbar^3}\left(\frac{eP}{\hbar\omega}\right)^4 \left(\frac{2m_r}{\hbar\Delta}\right)^{3/2} \frac{T_1}{T_2}, \tag{7.8}$$

where P is a matrix element discussed in Ref. [149], ω_G is the direct bandgap energy of the system, and m_r is the reduced effective mass of the exciton. This equation displays the same scaling with lifetimes as Eq. (7.7), so the considerations that follow should also apply for such semiconductors.

Now, consider the effects of changing the spontaneous emission properties for systems modeled by Eqs. (7.7) or (7.8). When spontaneous emission is suppressed, as in the photonic bandgap of a photonic crystal, T_1 will become large while T_2 remains finite, thus enhancing $\chi^{(3)}$ by up to one or more orders of magnitude (for materials with the correct properties). For large detunings (where $\Delta T_{2,\text{vac}} \gg 1$), I expect that $\chi^{(3)}$ will scale as T_1/T_2. The enhancement of the real part of $\chi^{(3)}$ is defined to be $\eta \equiv \operatorname{Re}\chi^{(3)}_{\text{purcell}} / \operatorname{Re}\chi^{(3)}_{\text{hom}}$, where $\chi^{(3)}_{\text{purcell}}$ is the nonlinear susceptibility in the presence of the Purcell effect, while $\chi^{(3)}_{\text{hom}}$ is the nonlinear susceptibility in a homogeneous medium. Since $T_1^{-1} = \Gamma_{\text{rad}} + \Gamma_{\text{nr}}$, the maximum enhancement is predicted to be roughly:

$$\eta \approx \frac{T_{1,\text{purcell}}T_{2,\text{vac}}}{T_{1,\text{hom}}T_{2,\text{purcell}}} = \frac{\frac{1}{2}\Gamma_{\text{nr}} + \gamma_{\text{phase}}}{\frac{1}{2}(\Gamma_{\text{nr}} + \Gamma_{\text{rad}}) + \gamma_{\text{phase}}} \frac{\Gamma_{\text{rad}} + \Gamma_{\text{nr}}}{\Gamma_{\text{nr}}} \tag{7.9}$$

where Γ_{rad} is the radiative decay rate in vacuum. Since the Purcell effect increases the amplitude of $\chi^{(1)}$, one might also expect it to increase the amplitude of $\chi^{(3)}$; however, according to Eq. (7.9), the opposite is true. This can be understood by noting that Purcell enhancement decreases the allowed virtual lifetime, and thus, the likelihood of nonlinear processes to occur [110]. Moreover, since the Purcell factor [22] is calculated by only considering the photon modes [21], one would not necessarily expect phase damping effects to play a role, in marked contrast with Eq. (7.9). This result comes about because $\chi^{(3)}$ comes directly from the polarization of the medium, which exhibits a significant T_2 dependence. Thus, the absence of phase damping effects causes any enhancement effects to disappear. On the other hand, the presence of large phase damping effects makes T_2 effectively constant, which means that suppression of spontaneous emission (caused by the absence of photonic states at appropriate energies [42]) can enhance Kerr nonlinearities by one or more orders of magnitude, while enhancement of spontaneous emission via the Purcell effect [21, 141] can suppress these nonlinearities. For the case where Purcell enhancement takes place, T_1 decreases while T_2 may not change as rapidly, due to the constant contribution of phase damping effects. This applies in the regime where $T_1 \gg \gamma_{\text{phase}}^{-1}$. Otherwise, if T_1 is sufficiently small, then T_2 will scale in the same way, and $\chi^{(3)}$ will remain approximately constant for large detunings, where $\Delta T_2 \gg 1$. This opens up the possibility of suppressing nonlinearities in photonic crystals (to a certain degree). For processes such as four-wave mixing or cross phase modulation, $\chi^{(3)}$ will generally involve a detuning term and will differ from Eq. (7.6). It is also interesting to note that this enhancement scheme will generally not increase non-linear losses, which are a very important consideration in all-optical signal processing. If the nonlinear switching figure of merit ξ is defined by $\xi = \mathrm{Re}\,\chi^{(3)}/(\lambda\,\mathrm{Im}\,\chi^{(3)})$ [150], then $\xi_{\mathrm{purcell}}/\xi_{\mathrm{vacuum}} = T_{2,\mathrm{purcell}}/T_{2,\mathrm{vacuum}} \geq 1$, for all cases of suppressed spontaneous emission.

7.3 2D photonic crystal example

The general principal described thus far should apply for any medium where the local density of states is substantially modified. In what follows, I show how this effect would manifest itself in one such exemplary system: a photonic crystal. This example serves as an illustration as to how strong nonlinearity suppression / enhancement effects could be achieved in realistic physical systems. It consists of a 2D triangular lattice of air holes in a high-dielectric medium ($\epsilon = 13$), with a two-level system placed in the middle, as in Fig. 7-1.

Note that the vast majority of photonic crystal literature is generally focused on modification of dispersion relations at the frequency of the light that is sent in as a probe. By contrast, in the current work, it is only essential to modify the dispersion relation for the frequencies close to the atomic resonances; the dispersion at the frequency of the light sent in as a probe can remain quite ordinary.

First, consider the magnitude of the enhancement or suppression of spontaneous emission in this system. Clearly, since there are several periods of high contrast dielectric, two effects are to be expected. First, there will be a substantial but incomplete suppression of emission inside the bandgap. Second, there will be an enhancement of spontaneous emission outside the bandgap (since the density of states is shifted to the frequencies surrounding the bandgap). For an atom polarized in the direction out of the 2D plane, only the TM polarization need be considered. The results are plotted in Fig. 7-2.

A GaAs-AlGaAs single quantum well can lie in the interesting regime discussed above, where the radiative loss rate Γ_{rad} dominates the non-radiative loss rate Γ_{nr}

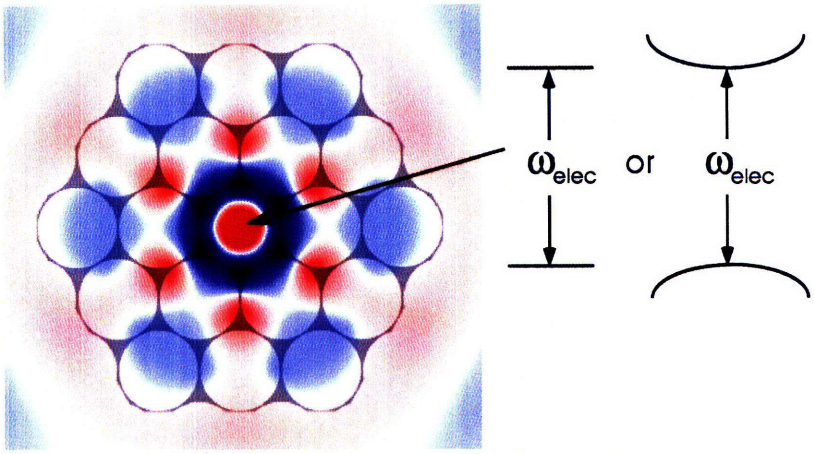

Figure 7-1: A 2D triangular lattice of air holes in dielectric, ($\epsilon = 13$). On top of the dielectric structure in grey, the E_z field is plotted, with positive values in red, and negative values in blue. A small region of nonlinear material is placed exactly in the center of the structure. This material may be, for example, either two-level atoms, quantum wells, or some semiconductors such as InSb.

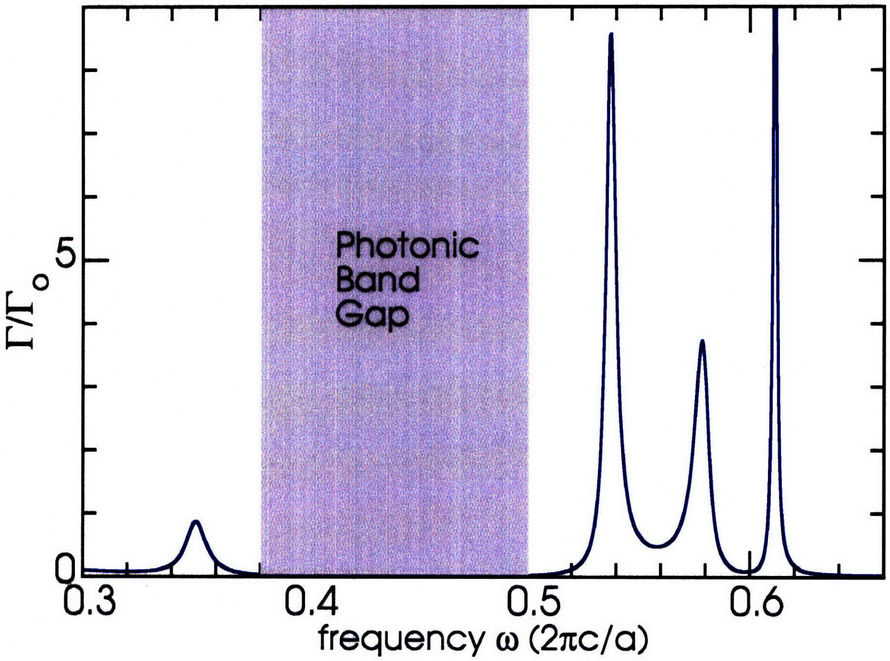

Figure 7-2: Relative enhancement of the TM local density of states for Fig. 7-1, as measured in the time-domain simulation rate of emission, Γ, normalized by the emission rate in vacuum, Γ_o

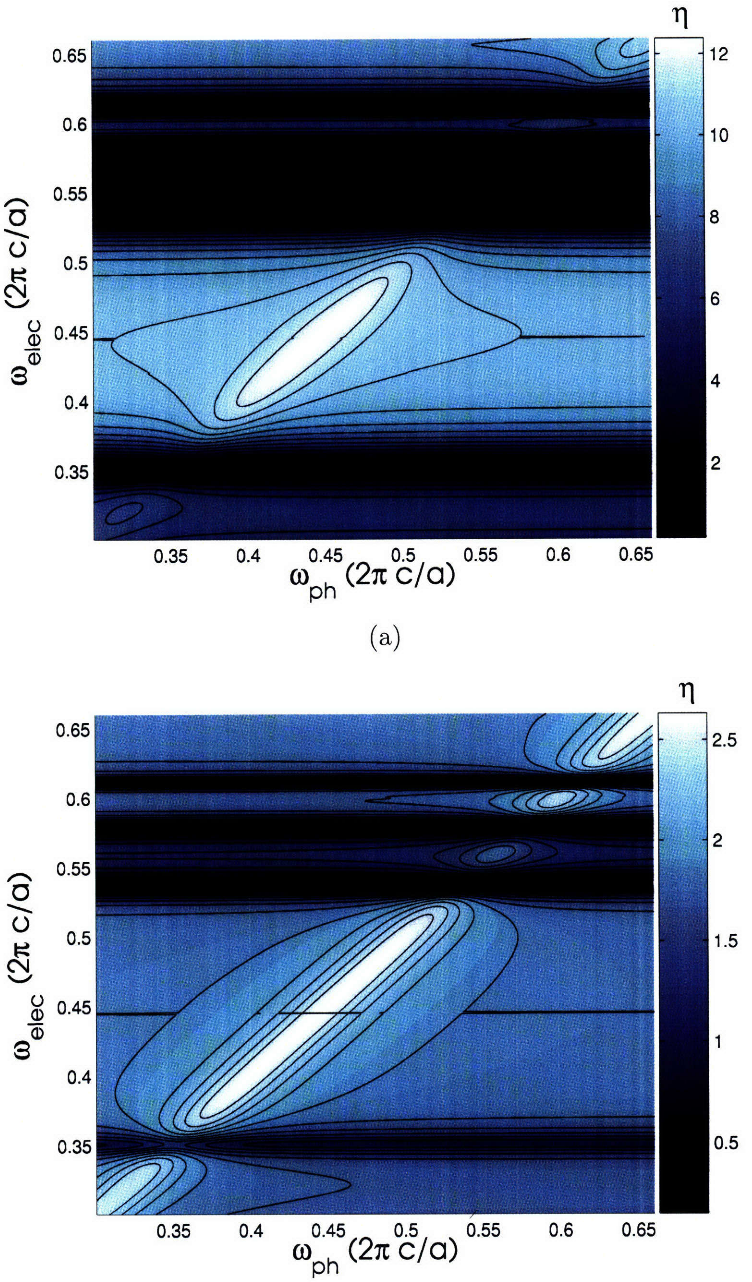

(a)

(b)

Figure 7-3: Contour plot of Kerr enhancement $\eta \equiv \mathrm{Re}\,\chi^{(3)}_{\text{purcell}} / \,\mathrm{Re}\,\chi^{(3)}_{\text{hom}}$ as a function of probe (ω_{ph}) and electronic transition (ω_{elec}) frequencies, for a single quantum well of GaAs-AlGaAs, (a) at $T = 200$ K, with $0.1\gamma_{\text{phase}} = 10\Gamma_{\text{nr}} = \Gamma_{\text{rad}}$, and (b) at $T = 225$ K, with $0.1\gamma_{\text{phase}} = \Gamma_{\text{nr}} = \Gamma_{\text{rad}}$.

as well as the overall loss rate of the quantum well, for certain temperatures [151]. Equation (7.8) implies that one can see substantial enhancement of the Kerr coefficient in that regime.

At a temperature of about 200 K, $\Gamma_{\text{nr}} \approx 0.1\Gamma_{\text{rad}}$ [151]. Although experimental measurements for γ_{phase} are unavailable to the present author, the presence of a substantial phonon bath at that temperature leads one to expect a fairly large value, which may be conservatively estimated by $10\Gamma_{\text{rad}}$. These results are displayed in Fig. 7-3(a). Note that enhancement is primarily observed inside the photonic bandgap (cf. Fig. 7-2). I observe an enhancement in the real part of the Kerr coefficient up to a factor of 12, close to the predicted maximum enhancement factor of 10.48 in the regime of large detunings ($\Delta T_2 \gg 1$).

Also, at a temperature of about 225 K, $\Gamma_{\text{nr}} \approx \Gamma_{\text{rad}}$ [151], and again I take $\gamma_{\text{phase}} = 10\Gamma_{\text{rad}}$. These results are displayed in Fig. 7-3(b). In this case, I observe an enhancement up to a factor of 2.5, close to the predicted maximum enhancement factor of 1.91 in the regime of large detunings ($\Delta T_2 \gg 1$).

Finally, note that close to room temperature (285 K), the system in Ref. [151] displays $\Gamma_{\text{nr}} \approx 10\Gamma_{\text{rad}}$, which is predicted to yield a maximum enhancement factor of 1.06. Since this number is fairly negligible, it illustrates that this approach has little impact when non-radiative losses dominate the decay of the electronic system.

In conclusion, I have shown that the Purcell effect can be used to tailor optical nonlinearities. This principle manifests itself in an exemplary two-level system embedded in a photonic crystal; for realistic physical parameters, enhancement of Kerr nonlinearities by more than an order of magnitude is predicted. The described phenomena is caused by modifications of the local density of states near the resonant frequency. Thus, this treatment can easily be applied to analyze the Kerr nonlinearities of two-level systems in almost any geometrical structure in which the Purcell effect is substantial (e.g., photonic crystal fibers [152], optical cavities). It also presents a reliable model for a variety of materials, such as quantum dots, atoms, and certain semiconductors. Future investigations will involve extending the formalism in this chapter to other material systems.

7.4 Numerical methods

I obtain the enhancement of spontaneous emission by performing two time-domain simulations in Meep [153], a finite difference time-domain code which solves Maxwell's equations exactly with no approximations, apart from discretization (which can be systematically reduced) [134]. First, I calculate the spontaneous emission of a dipole placed in the middle of the photonic crystal structure illustrated in Fig. 7-1, then divide by the spontaneous emission rate observed in vacuum. The resulting values of T_1 and T_2 are calculated numerically, and used as inputs in the calculation of the enhancement factor η of Eq. (7.9), plotted in Fig. 7-3.

Chapter 8

Conclusion

Although the behaviors of materials such as linear dielectrics, dispersive materials, and metals placed in photonic crystals have been studied in great depth, the study of active materials in photonic crystals is just beginning to emerge. It has been shown here that there are a wide variety of phenomena enabled by the introduction of photonic crystals into active material systems. This comes about through strong modification of the photonic local density of states (LDOS). For example, an increase in the LDOS that leads to enhancement of spontaneous emission is referred to as the Purcell effect. The LDOS is influenced by both the photonic bandstructure and field profiles. In the presence of defect structures, the field profiles for modes with frequencies inside the photonic bandgap are strongly localized inside the defect region, leading to huge increases in the local density of states. This can lead to substantial enhancement of the following effects: spontaneous emission (chapter 2), stimulated emission, which lowers lasing thresholds (chapter 3), photovoltaic electron-hole generation (chapter 4), and phase sensitivity (chapter 5). These effects are not confined to the semi-classical regimes, either; in the quantum regime, single-photon switching can be enabled through the enhancement of the LDOS (chapter 6). Physically, the enhancement of the LDOS makes the system strongly coupled, which creates the possibility of intriguing quantum effects such as entanglement. Finally, an interesting result from chapter 7 is that suppression of the LDOS can actually enhance certain quantities, such as the coefficient of Kerr nonlinearity. Clearly, the effect of embedding these active materials in photonic structures is far from trivial, and has created a rich new area for exploration which lies at the intersection of traditional photonic crystal literature with literature on the Purcell effect. Photonic crystals' unique ability to tailor the LDOS has been shown to lead to many exciting new phenomena and applications.

Furthermore, there are still a number of materials as well as systems that are open for investigation. Many of these materials and systems could be studied using tools that have recently been developed (possibly with slight modifications). So it looks like the future for active materials in photonic structures is bright. Here, I list a couple of areas that may be of near-term interest for further investigation:

Combining multiple light-trapping approaches

As illustrated in chapters 2 and 4, photonic crystals have the potential to enhance light-trapping effects by manipulating the photon density of states. An open question is whether these effects can be combined with existing or future light trapping approaches. Two ideas readily present themselves. First one can improve on antireflection coatings by considering that reflection on the front *and* back surfaces is required to create a destructive interference that couples the most light into the cell. Furthermore, this effect must be sustained over a very wide bandwidth (corresponding to $\delta\omega/\omega_{\text{mid}} \approx 0.5$). In principle, this optimization should be compatible with the waveguiding effect being induced by the photonic crystals on the backside, but this must be tested; the necessary tools have already been developed. Second, one would like to combine the photonic-crystal light-trapping approach with geometrical optics-based approaches in order to achieve even higher efficiencies. Insofar as a real textured surface fails to scatter light, photonic crystals should be able to fill in the gaps for light trapping.

Enhanced light trapping in novel systems

The light trapping effects discussed in this thesis may also apply to any number of detection systems that possess an optical components. This is *particularly* true when the optical radiation one wants to detect is emitted in a random direction, because optical fibers are poorly suited for omnidirectional light guidance. However, this can be true to a certain extent any time that the quantum efficiency is below 100%. Some important detection systems not treated in this thesis are neutron and gamma-ray detection systems (which typically rely on scintillating materials that emit at optical wavelengths), and high quantum efficiency single photon detectors (for use in deep-space astronomy, quantum computing, and other high-fidelity applications).

Novel optical switching approaches

There are a wealth of optical switching schemes in the literature, which fundamentally come from atomic and molecular physics that create certain energy level structures. In discussions of cavity QED, it was shown that cavities in general, and particularly photonic crystal microcavities and other structures, can strongly affect optical transitions of these systems. This lets one imagine taking any number of optical switching schemes, and improving them. One that comes to mind is the J-aggregate, which offers a uniquely high optical density of states due to a combination of a quasi-1D electronic bandstructures, small dipole size, and short-range coherence (which makes several dipoles act as one). They offer the possibility of creating cheap, low-power optical switches.

Bibliography

[1] J. Joannopoulos, R. Meade, and J. Winn, *Photonic Crystals: Molding the Flow of Light* (Princeton, Princeton, NJ, 1995).

[2] J. D. Joannopoulos, P. R. Villeneuve, and S. Fan, Nature **386**, 143 (1997).

[3] J. D. Joannopoulos, S. G. Johnson, J. N. Winn, and R. D. Meade, *Photonic Crystals: Molding the Flow of Light*, 2nd ed. (Princeton, Princeton, NJ, 2007).

[4] Z. Dutton, *Ultra-slow, stopped, and compressed light in Bose-Einstein condensates*, PhD thesis, Harvard University, 2002.

[5] O. Shapira, F. Sorin, and Y. Fink, Fiber amplification by side excitation, 2007.

[6] E. Yablonovitch, Phys. Rev. Lett. **58**, 2059 (1987).

[7] S. John, Phys. Rev. Lett. **58**, 2486 (1987).

[8] E. Yablonovitch and T. J. Gmitter, Phys. Rev. Lett. **63** (1989).

[9] K. M. Ho, C. T. Chan, and C. M. Soukoulis, Phys. Rev. Lett. **65**, 3152.

[10] R. D. Meade, A. M. Rappe, K. D. Brommer, J. D. Joannopoulos, and O. L. Alerhand, Phys. Rev. B **48**, 8434 (1993).

[11] R. D. Meade, K. D. Brommer, A. M. Rappe, and J. D. Joannopoulos, Phys. Rev. B **44**, 13772 (1991).

[12] A. Mekis, J. Chen, I. Kurland, S. Fan, P. Villeneuve, and J. Joannopoulos, Phys. Rev. Lett. **77**, 3787 (1996).

[13] S. Fan, P. R. Villeneuve, J. D. Joannopoulos, and E. F. Schubert, Phys. Rev. Lett. **78**, 3294 (1997).

[14] S. G. Johnson, S. Fan, P. R. Villeneuve, J. D. Joannopoulos, and L. A. Kolodziejski, Phys. Rev. B **60**, 5751 (1999).

[15] Y. Xu, J. Vuckovic, R. K. Lee, O. Painter, A. Scherer, and A. Yariv, J. Opt. Soc. Am. B **16**, 465 (1999).

[16] S. Fan, P. R. Villeneuve, J. D. Joannopoulos, and H. A. Haus, Phys. Rev. Lett. **80**, 960 (1998).

[17] Y. Fink, J. N. Winn, S. Fan, C. Chen, J. Michel, J. D. Joannopoulos, and E. L. Thomas, Science **282**, 1679 (1998).

[18] M. Ibanescu, Y. Fink, S. Fan, E. L. Thomas, and J. D. Joannopoulos, Science **289**, 415 (2000).

[19] S. Johnson, M. Ibanescu, M. Skorobogatiy, O. Weisberg, T. Engeness, M. Soljacic, S. Jacobs, J. Joannopoulos, and Y. Fink, Opt. Express **9**, 748 (2001).

[20] L. C. Andreani, G. Panzarini, and J.-M. Gerard, Phys. Rev. B **60**, 13276 (1999).

[21] H. Ryu and M. Notomi, Opt. Lett. **28**, 2390 (2003).

[22] E. Purcell, Phys. Rev. **69**, 681 (1946).

[23] M. O. Scully and M. S. Zubairy, *Quantum Optics* (Cambridge University Press, Cambridge, England, 1997).

[24] K.-J. Boller, A. Imamoglu, and S. E. Harris, Phys. Rev. Lett. **66**, 2593 (1991).

[25] E. Arimondo, *Progress in Optics,*volume 34 (Elsevier Science, Amsterdam, 1996), p. 257.

[26] E. Marcatilli and R. Schmeltzer, Bell Syst. Tech. J. **43**, 1783 (1964).

[27] J. Harrington, Fiber Integr. Opt. **19**, 211 (2000).

[28] Y. Matsuura, T. Abel, and J. Harrington, Appl. Opt. **34**, 6842 (1995).

[29] M. Born, *Optik* (Springer, Berlin, 1933).

[30] W. Weinstein, J. Opt. Soc. Am. **37**, 576 (1947).

[31] F. Abeles, Ann. de Physique **5**, 596, 706 (1950).

[32] M. Born and E. Wolf, *Principles of Optics* (Pergamon Press, Bath, England, 1959).

[33] P. Yeh, A. Yariv, and E. Marom, J. Opt. Soc. Am. **68**, 1196 (1978).

[34] A. Cho, A. Yariv, and P. Yeh, Appl. Phys. Lett. **30**, 471 (1977).

[35] P. Yeh, A. Yariv, and C.-S. Hong, J. Opt. Soc. Am. **67**, 423 (1977).

[36] N. Doran and K. Blow, J. Lightwave Tech. **LT-1**, 588 (1983).

[37] M. Miyagi and S. Kawakami, J. Lightwave Tech. **2**, 116 (1984).

[38] C. de Sterke and I. Bassett, J. Appl. Phys. **76**, 680 (1994).

[39] Y. Fink, D. J. Ripin, S. Fan, C. Chen, J. D. Joannopoulos, and E. L. Thomas, J. Lightwave Technol. **17**, 2039 (1999).

[40] S. Hart, G. Maskaly, B. Temelkuran, P. Prideaux, J. Joannopoulos, and Y. Fink, Science **296**, 510 (2002).

[41] B. Temelkuran, S. Hart, G. Benoit, J. Joannopoulos, and Y. Fink, Nature **420**, 650 (2002).

[42] D. Kleppner, Phys. Rev. Lett. **47**, 233 (1981).

[43] R. Hulet, E. Hilfer, and D. Kleppner, Phys. Rev. Lett. **55**, 2137 (1985).

[44] J. Fleming, S. Lin, I. El-Kady, R. Biswas, and K. Ho, Nature **417**, 52 (2002).

[45] K. Busch and S. John, Phys. Rev. E **58**, 3896 (1998).

[46] R. Magnanini and F. Santosa, SIAM J. Appl. Math. **61**, 1237 (2000).

[47] K. S. Yee, IEEE Trans. Attennas Propag. **AP-14**, 302 (1966).

[48] Z. S. Sacks, D. M. Kingsland, R. Lee, and J.-F. Lee, IEEE Trans. Antennas Propag. **AP-43**, 1460 (1995).

[49] G. Gilat and L. Raubenheimer, Phys. Rev. **144**, 390 (1966).

[50] C. Hooijer, D. Lenstra, and A. Legendijk, Opt. Lett. **25**, 1666 (2000).

[51] G. Agrawal, *Applications of Nonlinear Fiber Optics,*Optics and Photonics (Academic Press, San Diego, CA, 2001).

[52] E. Hecht, *Optics* (Addison-Wesley, Reading, MA, 1998).

[53] N. W. Ashcroft and N. D. Mermin, *Solid State Physics* (Holt Saunders, Philadelphia, PA, 1976).

[54] G. D. Mahan, *Many-Particle Physics* (Kluwer Academic, New York, 2000).

[55] A. E. Siegman, *Lasers* (University Science Books, Sausalito, CA, 1986).

[56] C. Kittel, *Introduction to Solid State Physics* (John Wiley and Sons, New York, 1986).

[57] A. Schawlow and C. Townes, Phys. Rev. **112**, 1940 (1958).

[58] B. Toland, B. Houshmand, and T. Itoh, IEEE Microw. Guided Wave Lett. **3**, 333 (1993).

[59] H. Cao, J. Xu, D. Zhang, S.-H. Chang, S. Ho, E. Seelig, X. Liu, and R. Chang, Phys. Rev. Lett. **84**, 5584 (2000).

[60] O. Painter, R. Lee, A. Scherer, A. Yariv, J. O'Brien, P. Dapkus, and I. Kim, Science **284**, 1819 (1999).

[61] J. Vučković, O. Painter, Y. Xu, A. Yariv, and A. Scherer, IEEE J. Quantum Electron. **35**, 1168 (1999).

[62] R. Ziolkowski, J. Arnold, and D. Gogny, Phys. Rev. A **52**, 3082 (1995).

[63] A. S. Nagra and R. A. York, IEEE Trans. Antennas Propag. **46**, 334 (1998).

[64] R. W. Ziolkowski, IEEE Trans. Antennas Propag. **45**, 375 (1997).

[65] G. Slavcheva, J. Arnold, I. Wallace, and R. Ziolkowski, Phys. Rev. A **66**, 063418 (2002).

[66] S. John and G. Pang, Phys. Rev. A **54**, 3642 (1996).

[67] X. Jiang and C. Soukoulis, Phys. Rev. Lett. **85**, 70 (2000).

[68] C. Soukoulis, X. Jiang, J. Xu, and H. Cao, Phys. Rev. B **65**, 041103(R) (2002).

[69] C. Vanneste and P. Sebbah, Phys. Rev. Lett. **87**, 183903 (2001).

[70] P. Sebbah and C. Vanneste, Phys. Rev. B **66**, 144202 (2002).

[71] H. Cao, J. Phys. A **38**, 10497 (2005).

[72] T. Harayama, S. Sunada, and K. S. Ikeda, Phys. Rev. A **72**, 013803 (2005).

[73] S.-H. Chang and A. Taflove, Opt. Express **12**, 3827 (2004).

[74] F. Schlottau, M. Piket-May, and K. Wagner, Opt. Express **13**, 182 (2005).

[75] C. Herzinger, B. Johs, W. McGahan, J. Woollam, and W. Paulson, J. Appl. Phys. **83**, 3323 (1998).

[76] ASTMG173-03, *Standard Tables for Reference Solar Spectral Irradiances: Direct Normal and Hemispherical on 37 degree Tilted Surface* (ASTM International, West Conshohocken, Pennsylvania, 2005).

[77] E. Yablonovitch and G. Cody, IEEE Trans. Electron Devices **ED-29**, 300 (1982).

[78] P. Campbell and M. A. Green, J. Appl. Phys. **62**, 243 (1987).

[79] R. Brendel, M. Hirsch, R. Plieninger, and J. Werner, IEEE Trans. Electron Devices **43**, 1104 (1996).

[80] L. Feitknecht, J. Steinhauser, R. Schluchter, S. Fay, D. Domine, E. Vallat-Sauvin, F. Meillaud, C. Ballif, and A. Shah, Investigations on fill-factor drop of microcrystalline silicon p-i-n solar cells deposited onto highly surface-textured zno substrates, in *Tech. Digest PVSEC-15*, Shanghai, China, 2005.

[81] H. Bender, J. Szlufcik, H. Nussbaumer, G. Palmers, O. Evrard, J. Nijs, R. Mertens, E. Bucher, and G. Willeke, Appl. Phys. Lett. **62**, 2941 (1993).

[82] J. Gee, in *Twenty-ninth IEEE Photovolt. Spec. Conf.*, p. 150, 2002.

[83] R. Brendel, *Thin-Film Crystalline Silicon Solar Cells* (Wiley-VCH, Weinheim, Germany, 2003).

[84] P. Sheng, A. Bloch, and R. Stepleman, Appl. Phys. Lett. **43**, 579 (1983).

[85] R. H. Morf and H. Kiess, in *Proc. Ninth Internat. Conf. Photovolt. Solar Energy*, edited by W. Palz, Brussels, 1989, Commission of the European Communities.

[86] H. Kiess and R. H. Morf, Proc. SPIE **1149**, 124 (1989).

[87] M. Gale, B. Curtis, H. Kiess, and R. H. Morf, Proc. SPIE **1272**, 60 (1990).

[88] C. Heine and R. H. Morf, Appl. Opt. **34**, 2476 (1995).

[89] S. H. Zaidi, J. M. Gee, and D. S. Ruby, in *Twenty-eighth Photovolt. Spec. Conf.*, p. 395, 2000.

[90] S. H. Zaidi, R. Marquadt, B. Minhas, and J. Tringe, in *Twenty-ninth IEEE Photovolt. Spec. Conf.*, p. 1290, 2002.

[91] L. Zeng, Y. Yi, C.-Y. Hong, X. Duan, and L. C. Kimerling, New light trapping in thin film solar cells using textured photonic crystals, in *Mater. Res. Soc. Symp. Proc.*, volume 862, Boston, MA, 2005, Materials Research Society.

[92] L. Zeng, P. Bermel, Y. Yi, N. Feng, C.-Y. Hong, X. Duan, J. D. Joannopoulos, and L. C. Kimerling, Optimization of textured photonic crystal backside reflectors for silicon thin-film solar cells, in *Mater. Res. Soc. Symp. Proc.*, volume 974E, Boston, MA, 2006, Materials Research Society.

[93] H. Kosaka, T. Kawashima, A. Tomita, M. Notomi, T. Tamamura, T. Sato, and S. Kawakami, Phys. Rev. B **58**, R10096 (1998).

[94] T. Tiedje, E. Yablonovitch, G. Cody, and B. Brooks, IEEE Trans. Electron Dev. **31**, 711 (1984).

[95] D. Whittaker and I. Culshaw, Phys. Rev. B **60**, 2610 (1999).

[96] J. Berenger, J. Comp. Phys. **114**, 185 (1994).

[97] W. Shockley and H. J. Queisser, J. Appl. Phys. **32**, 510 (1961).

[98] C. Henry, J. Appl. Phys. **51**, 4494 (1980).

[99] S. G. Johnson and J. D. Joannopoulos, Opt. Express **8**, 173 (2001).

[100] S. Kemme, S. Zaidi, and J. Gee, in *Ninth Workshop on c-Si Mat. and Proc.*, Breckenridge, Colorado, 1999.

[101] J. N. Winn, Y. Fink, S. Fan, and J. D. Joannopoulos, Opt. Lett. **23**, 1573 (1998).

[102] A. Yariv, *Optical Electronics in Modern Communications*, 5th ed. (Oxford University Press, 1997).

[103] J. A. Thomas and Y. Fainman, Appl. Opt. **37**, 6196 (1999).

[104] R. A. Meyer, Appl. Opt. **11**, 613 (1972).

[105] P. F. McManamon, T. A. Dorschner, D. L. Corkum, L. J. Friedman, D. S. Hobbs, M. Holz, S. Liberman, H. Q. Nguyen, D. P. Resler, R. C. Sharp, and E. A. Watson, Proc. IEEE **84**, 268 (1996).

[106] E. Lidorikis, M. Povinelli, S. Johnson, and J. Joannopoulos, Phys. Rev. Lett. **91**, 023902 (2003).

[107] R. W. Boyd, *Nonlinear Optics* (Academic Press, San Diego, 1992).

[108] M. Soljacic, M. Ibanescu, S. G. Johnson, Y. Fink, and J. D. Joannopoulos, Phys. Rev. E **66**, 055601 (2002).

[109] M. Soljacic and J. D. Joannopoulos, Nat. Mater. **3**, 211 (2004).

[110] J. J. Sakurai, *Modern Quantum Mechanics* (Addison-Wesley, Reading, MA, 1994).

[111] H. Gibbs, *Optical Bistability: Controlling Light with Light* (Academic Press, Orlando, FL, 1985).

[112] L. V. Hau, S. E. Harris, Z. Dutton, and C. Behroozi, Nature **397**, 594 (1999).

[113] E. Arimondo, *Progress in Optics,*volume 35 (Elsevier Science, Amsterdam, 1997), p. 259.

[114] M. Soljacic, E. Lidorikis, J. D. Joannopoulos, and L. V. Hau, Appl. Phys. Lett. **86**, 171101 (2005).

[115] Q. Turchette, C. Hood, W. Lange, H. Mabuchi, and H. Kimble, Phys. Rev. Lett. **75**, 4710 (1995).

[116] A. Imamoglu, H. Schmidt, G. Woods, and M. Deutsch, Phys. Rev. Lett. **79**, 1467 (1997).

[117] M. Werner and A. Imamoglu, Phys. Rev. A **61**, 011801(R) (1999).

[118] S. Rebic, S. Tan, A. Parkins, and D. Walls, J. Opt. B: Quantum Semiclass. Opt. **1**, 490 (1999).

[119] K. M. Gheri, W. Alge, and P. Grangier, Phys. Rev. A **60**, R2673 (1999).

[120] A. D. Greentree, J. A. Vaccaro, S. R. de Echaniz, A. V. Durrant, and J. P. Marangos, J. Opt. B: Quantum Semiclass. Opt. **2**, 252 (2000).

[121] K. Birnbaum, A. Boca, R. Miller, A. Boozer, T. Northup, and H. Kimble, Nature **436**, 87 (2005).

[122] R. Beausoleil, W. Munro, and T. Spiller, ArXiV:quant-ph , 0302109 v3 (2005).

[123] S. John, J. Opt. A **3**, S103 (2001).

[124] B. Ham, P. Hemmer, and M. Shahriar, Opt. Commun. **144**, 227 (1997).

[125] A. Turukhin, V. Sudarshanam, M. Shahriar, J. Musser, B. Ham, and P. Hemmer, Phys. Rev. Lett. **88**, 023602 (2002).

[126] T. Yoshie, A. Scherer, J. Hendrickson, G. Khitrova, H. Gibbs, G. Rupper, C. Ell, O. Shchekin, and D. Deppe, Nature **432**, 200 (2004).

[127] S. G. Johnson and J. D. Joannopoulos, *Photonic Crystals: The Road from Theory to Practice* (Kluwer Academic, Boston, 2002).

[128] W. Suh, Z. Wang, and S. Fan, IEEE J. Quantum Electron. **40**, 1511 (2004).

[129] H. Haus and Y. Lai, J. Lightwave Tech. **9**, 754 (1991).

[130] H. Mabuchi, M. Armen, B. Lev, M. Loncar, J. Vuckovic, H. Kimble, J. Preskill, M. Roukes, and A. Scherer, Quantum Information and Computation **1**, 7 (2001).

[131] C. Hood, T. Lynn, A. Doherty, A. Parkins, and H. Kimble, Science **287**, 1447 (2000).

[132] S. Spillane, T. Kippenberg, K. Vahala, K. Goh, E. Wilcut, and H. Kimble, Phys. Rev. A **71**, 013817 (2005).

[133] J.-T. Shen and S. Fan, Phys. Rev. Lett. **95**, 213001 (2005).

[134] A. Taflove and S. C. Hagness, *Computational Electrodynamics*, 2nd ed. (Artech House, Norwood, MA, 2000).

[135] H. Schmidt and A. Imamoglu, Opt. Lett. **21**, 1936 (1996).

[136] S. E. Harris and L. Hau, Phys. Rev. Lett. **82**, 4611 (1999).

[137] Y. Yamamoto and A. Imamoglu, *Mesoscopic Quantum Optics* (John Wiley and Sons, Inc., New York, 1999).

[138] P. Drazin and R. Johnson, *Solitons: an Introduction* (Cambridge University Press, Cambridge, England, 1989).

[139] M. Nielsen and I. Chuang, *Quantum Computation and Quantum Information* (Cambridge University Press, Cambridge, England, 2000).

[140] P. Bermel, J. Joannopoulos, Y. Fink, P. Lane, and C. Tapalian, Phys. Rev. B **69**, 035316 (2004).

[141] D. Englund, D. Fattal, E. Waks, G. Solomon, B. Zhang, T. Nakaoka, Y. Arakawa, Y. Yamamoto, and J. Vuckovic, Phys. Rev. Lett. **95**, 013904 (2005).

[142] S. John and T. Quang, Phys. Rev. Lett. **76**, 2484 (1996).

[143] J. Preskill, Quantum computation lecture notes, http://www.theory.caltech.edu/people/preskill/ph229/, 2004.

[144] C. Cohen-Tannoudji, B. Diu, and F. Laloë, *Quantum Mechanics* (John Wiley and Sons, New York, 1977).

[145] S. John and T. Quang, Phys. Rev. A **50**, 1764 (1994).

[146] P. Lambropoulos, G. M. Nikolopoulos, T. R. Nielsen, and S. Bay, Rep. Prog. Phys. **63**, 455 (2000).

[147] M. Bayer, T. Reinecke, F. Weidner, A. Larionov, A. McDonald, and A. Forchel, Phys. Rev. Lett. **86**, 3168 (2001).

[148] P. Lodahl, A. F. van Driel, I. S. Nikolaev, A. Irman, K. Overgaag, D. Vanmaekelbergh, and W. L. Vos, Nature **430**, 654 (2004).

[149] D. Miller, S. Smith, and B. Wherrett, Opt. Comm. **35**, 221 (1980).

[150] G. Lenz, J. Zimmermann, T. Katsufuji, M. E. Lines, H. Y. Hwang, S. Splter, R. E. Slusher, S.-W. Cheong, J. S. Sanghera, and I. D. Aggarwal, Opt. Lett. **25**, 254 (2000).

[151] S. Kraiem, F. Hassen, H. Maaref, X. Marie, and E. Vaneelle, Opt. Mat. **17**, 305 (2001).

[152] N. M. Litchinitser, A. Abeeluck, C. Headley, and B. Eggleton, Opt. Lett. **27**, 1592 (2002).

[153] A. Farjadpour, D. Roundy, A. Rodriguez, M. Ibanescu, P. Bermel, J. D. Joannopoulos, S. G. Johnson, and G. Burr, Opt. Lett. **31**, 2972 (2006).